UCLouvain

École polytechnique de Louvain

Analysis of the saturated absorption of the HD molecule in an optical cavity

Author: **Victor Bomans**
Supervisors: **Matthieu Génévriez, Clément Lauzin**
Readers: **Xavier Gonze, Xavier Urbain**
Academic year 2024–2025
Master [120] in Physical Engineering

Contents

Chapter 1

Introduction

1.1 The motivation behind the study of HD saturated spectroscopy

1.1.1 Discrepency between QED and experiment

The HD molecule is an isotopolog of H_2 which is one of the simplest molecules. This relative simplicity makes it possible to proceed with theoretical tools in the determination of the rovibrational energy levels of such molecules with great precision [1]. The theoretical framework used in such calculations is a quantum field theory: quantum electrodynamics (QED).

Quantum field theory is the most successful theory describing nature up to now. Quantum electrodynamics is "the most stringently tested - and the most dramatically successful - of all physical theories" according to one of the most known textbook on the topic [2]. The numerous tests on QED include measurement of the anomalous magnetic moment of the electron and the muon, the Lamb shift, hydrogen hyperfine splitting, quantum Hall effect, AC Josephson effect, ... All these experiments allow the evaluation of the fine structure constant α. The value of the fine structure constant α is of upmost importance in QED because it is the one parameter that determines the strength of the electrodynamics interaction and is thus at the core of any theoretical prediction. All the precision experiments mentioned agree to great precision with the value of the fine structure constant α and these values can also be found in [2]. This is one of the greatest success of quantum electrodynamic.

Hence the discrepancy between any QED theoretical prediction and experimental results should be of great concern. Such a deviation from theoretical prediction is observed for several rovibrationnal transition of the $(2-0)$ band of the hydrogen deuteride (HD) [3] as shown on fig. 1.1.

This discrepancy between theory and experiment might lead to new physics. Indeed the precision reached in recent experiment on hydrogen system allows to test quantum electrodynamic with high precision [7] but also to search for a fifth force [8] or even extra dimensions [9].

Although the error bars do not overlap, one must be cautious before claiming the non validity of QED in this case. On the one hand, QED prediction implies several approximations in order to calculate the energy level structure in the HD molecule because one can not calulate it directly from exact QED as will be briefly explained in the next paragraph. On the other hand, the experimental line profile of the HD (2-0) rovibrationnal transitions present an unexpected asymmetric shape whose physical explanation is still unknown. Thus the reason for

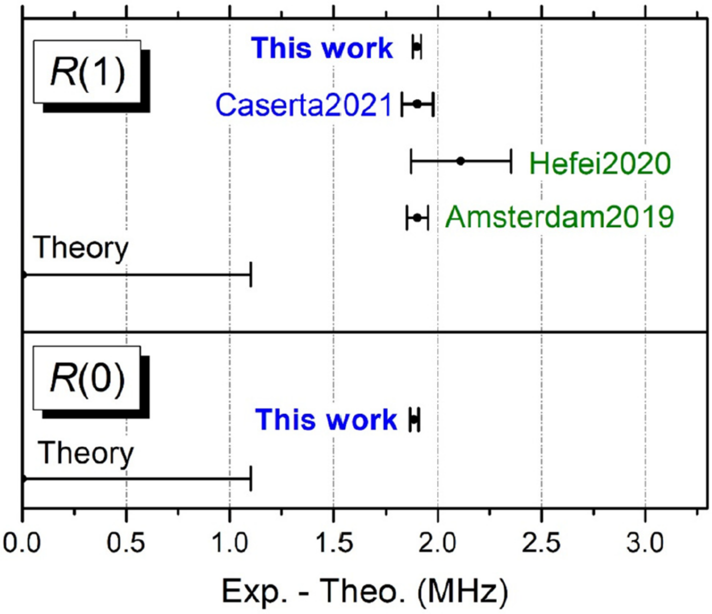

Figure 1.1: Discrepancy between QED prediction and experimental results. This graph was taken from [3] and **This work** thus refers to [3]. On this graph is represented both the QED prediction and the experimental results for the rovibrational transition (2-0) R(0) and R(1) for HD with their rescpective error bars. Amsterdam2019 refers to [4], Hefei2020 refers to [5] and Caserta2021 refers to [6] . The QED prediction comes from [1].

this discrepancy is still unlcear currently.

The theoretical predictions from QED come from a theoretical method called non relativistic quantum electrodynamics (NRQED) which mainly consists in assuming that the total energy of the system can be expanded in power of the fine-structure constant α [1]:

$$E(\alpha) = \alpha^2 mE^{(2)} + \alpha^{(4)} m \left(E^{(4)} + E^{(4)}_{FS} \right) + \alpha^{(5)} mE^{(5)} + \alpha^{(6)} mE^{(6)} + ...$$

where $E^{(2)}$ is the non relativistic energy of the system, $E^{(4)}$ is the relativistic correction, $E^{(5)}$ is the leading QED correction, $E^{(i)}$ $i > 5$ are higher order corrections terms from QED. These contributions to the total energy are expectation values of operators given by the NRQED theory. Due to this approach, the Schrödinger equation and a non relativistic wavefunction can be used. With this approach the rovibrational energy levels of the HD molecule were calculated by Komasa and Puchalski [1] up to the $\alpha^7 m$ term reaching an accuracy on the order 10^{-3} to 10^{-7}cm^{-1}. In comparison, recent experiments in spectroscopy allowed to reach a relative precision of 10^{-10} for the measurement of the HD R(1) (2-0) rovibrational transition frequency [10] [11].

1.1.2 The asymmetric profile of the HD molecule

The theoretical aspects regarding QED calculations will not be further detailled because it is not the topic of this master thesis. This work focuses instead on the experimental part of the problem. More precisely the determination of a possible explanation of the asymmetric profile observed in the experiments. Indeed the ability to extract the transition frequency from the experimental measures rely strongly on the theoretical model used to fit the data point. Hence a model for the asymmetric profile is required but still currently missing.

The asymmetry of the absorption profile has been noticed since 2018 by a research group at Hefei [11] (see fig. 1.3) and another at Amsterdam [12] (see fig. 1.2). Both group since then are looking for an explanation of this asymmetric lineshape. In order to reach a high precision in their experiment the group of Hefei uses what is called cavity ringdown spectroscopy (CRDS) whereas the group of Amsterdam uses noise-immune cavity-enhanced optical heterodyne molecular spectroscopy (NICE-OHMS). As mentioned in a note added to the paper of Hefei [11] and the one of Amsterdam [12] the two groups have both analysed the absorption spectrum of C_2H_2 in order to check if the different experimental setup would be the cause of the discrepancy in their evaluation of the HD transition frequency at that time. They found the same result for C_2H_2 and so they have ruled out this hypothesis. We will come back in more details on the lastest research of these two groups on this asymmetric lineshape.

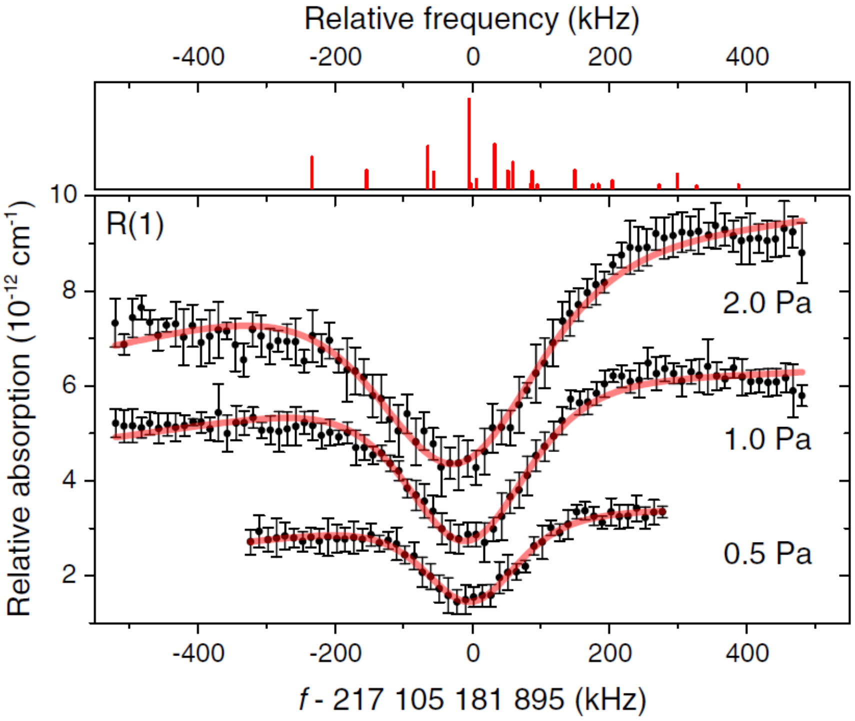

Figure 1.2: Asymmetric lineshape of the saturated absorption spectrum of the rovibrational R(1) (2-0) transition of HD (Lamb-dip), Amsterdam research group 2018 [12]. The absorption lines are shifted vertically for clarity. We observe that the lineshape becomes more and more asymmetric as the pressure increases. Image from [12].

In conclusion the asymmetry in the saturated absorption curve of the HD molecule has no explanation yet. This master thesis constitutes a preliminary step in the direction although no physical mechanism for the asymmetry will be inverstigated. The reason is that before searching for an explanation of the asymmetry, one must be able to model the expected symmetric absorption curve of the corresponding transitions. In this master thesis we will thus develop a numerical model to generate the expected saturated absorption curve of a gas of particles placed in an optical cavity.

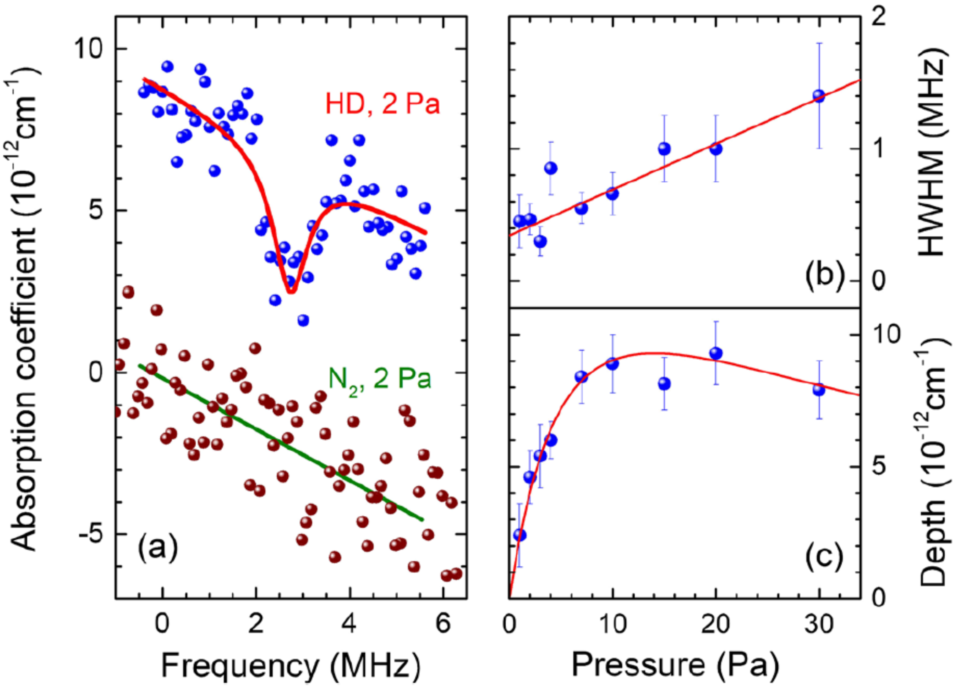

Figure 1.3: Asymmetric lineshape of the saturated absorption spectrum of the rovibrational R(1) (2-0) transition of HD (Lamb-dip), Hefei research group 2018 [11]. The absorption profile is shown for 2 Pa which corresponds to the same pressure as the most asymmetric profile on the graph of the research group from Amsterdam. Here again we can see that the lineshape is not symmetric around de Lamb-dip. Image from [11].

Chapter 2

State of the art

2.1 The usual theoretical framework for quantum optics

In this section we will briefly state the link between QED theory and the usual theoretical framework in spectrocopy because our initial concern is the discrepancy between QED and some spectroscopy experiments.

2.1.1 Equation for an isolated quantum system

The Lagrangian of quantum electrodynamics is the following

$$\mathcal{L}_{\mathrm{QED}} = \bar{\psi}\left(i\gamma^{\mu}\partial_{\mu} - m\right)\psi - \frac{1}{4}F^{\mu\nu}F_{\mu\nu} - e\bar{\psi}\gamma^{\mu}\psi A_{\mu} \tag{2.1}$$

The first term is the Dirac Lagrangian, the second is the electromagnetic Lagrangian and the last one is the interaction between the two. Relativistic treatement is not necessary for light atoms such as hydrogen. As we will focus on an hydrogen molecule ultimately we can replace the dynamics of the fermionic field and its coupling to the electromagnetic field (first term and last term of the Lagrangian) by the Pauli equation. Moreover the number of photon in a laser beam is high such that the quantum fluctuation with respect to the total intensity of light is very small and the classical description can be used [13]. However this approach neglects interactions between the atom (or molecule) and the vacuum state of the quantum electromagnetic field. In other words spontaneous emission of a photon is not described by the Pauli equation and must be added at some point. The non relativistic quantum description of a particle interacting with a classical electromagnetic field, called semiclassical approach, is describe by the Pauli equation:

$$i\hbar\frac{\partial\psi}{\partial t} = \left(\frac{1}{2m}\left(\hat{\vec{P}} - q\vec{A}\right)^2 + qU - \frac{q\hbar}{2m}\vec{\sigma}\cdot\vec{B}\right)\psi \tag{2.2}$$

If we can neglect the spin interaction then we find Schödinger equation with coupling to the electromagnetic field:

$$i\hbar\frac{\partial\psi}{\partial t} = \left(\frac{1}{2m}\left(\hat{\vec{P}} - q\vec{A}\right)^2 + qU\right)\psi \tag{2.3}$$

From there we can use the gauge degree of freedom of the electromagnetic field. Indeed, there is no unique choice of $\vec{A}$ and U that describes the same electromagnetic field. We can use these degrees of freedom to adapt the mathematical formulation of the equation to our problem. We follow what is done in [14], so we do not repeat all the mathematical details here. We impose the Coulomb gauge:

$$\nabla \cdot \vec{A} = 0 \tag{2.4}$$

and we obtain $\hat{H} = \hat{H}_0 + \hat{H}_{int}$, with

$$\hat{H}_0 = \frac{\hat{\vec{P}}}{2m} + qU \tag{2.5}$$

$$\hat{H}_{int} = -\frac{q}{m}\hat{\vec{P}} \cdot \vec{A} + \frac{q^2\vec{A}^2}{2m} \tag{2.6}$$

where $\hat{H}_0$ is the atomic or molecular Hamiltonian and $\hat{H}_{int}$ is the interaction between the electromagnetic field and the atom or molecule.

We now use the long wavelength approximation. This consists in neglecting the variation of the electromagnetic field over the volume of space occupied by the atom or the molecule because the wavelength of the light used in spectroscopy experiments is usually much larger than the atomic or molecular dimensions. Thus the electromagnetic field can be considered constant across the volume of space occupied by the atom or the molecule. The field $\vec{A}$ is thus evaluated at the location of the atom in the field. Let's call this location $\vec{r}_0$.

Eventually we impose a second gauge condition known as the *Göppert-Mayer* gauge:

$$\vec{A}'(\vec{r},t) = \vec{A}_\perp(\vec{r},t) - \vec{A}_\perp(\vec{r}_0,t) \tag{2.7}$$

$$U'(\vec{r},t) = U(\vec{r}) + (\vec{r} - \vec{r}_0) \cdot \frac{\partial}{\partial t}\vec{A}_\perp(\vec{r}_0,t) \tag{2.8}$$

The Hamiltonian becomes

$$\hat{H} = \frac{1}{2m}\left(\hat{\vec{P}} - q\vec{A}'(\hat{\vec{r}},t)\right)^2 + U(\vec{r}) + q(\hat{\vec{r}} - \vec{r}_0)\frac{\partial}{\partial t}\hat{\vec{A}}_\perp(\vec{r},t) \tag{2.9}$$

$$= \frac{1}{2m}\left(\hat{\vec{P}} - q\vec{A}'(\hat{\vec{r}},t)\right)^2 + U(\vec{r}) - q(\hat{\vec{r}} - \vec{r}_0)\vec{E}(\vec{r},t) \tag{2.10}$$

and we can rename $q(\hat{\vec{r}} - \vec{r}_0)$ as $\hat{\vec{D}}$ the electric dipole moment operator.

Due to the long wavelength approximation $\vec{A}'(\vec{r},t) = \vec{A}'(\vec{r}_0,t) = 0$. This results in the following form for the Hamiltonian:

$$\hat{H}_0 = \frac{\hat{\vec{P}}}{2m} + qU \tag{2.11}$$

$$\hat{H}_{int} = -\hat{\vec{D}} \cdot \vec{E}(\vec{r}_0,t) \tag{2.12}$$

The interaction Hamiltonian thus reduces to a coupling to the electromagnetic field through the electric instantaneous dipole moment of the atom or molecule. If the long wavelength approximation is not valid, one can use another gauge transformation to obtain an equation with higher order moments of the polar decomposition appearing in it [14].

2.1.2 Equation for a quantum system interacting with the environment

The equation discussed so far is only valid for isolated quantum system. Usually a quantum system such as in a spectroscopy laboratory interact with its environment. These interactions are, for example, spontaneous emission (interaction of the quantum system with the vacuum state of the quantum electromagnetic field), collisions with other atoms or the walls of the containers. These interactions break the unitary evolution described by the equation obtained above. One says that the coherent evolution is broken as the interaction with the environment causes a collapse of the wave function of the quantum system under study. These processes are thus called incoherent processes and they lead to quantum decoherence in the system under scrutiny.

A mathematical framework that includes the incoherent processes is the Lindblad equation or master equation. We will not dive into the details of this framework and only state the main ideas. More details can be found in [15]. In this framework, one reformulates the quantum system in the formalism of the density operator. This formalism works as follow.

For a quantum system described by a state vector $|\psi\rangle$, the density matrix operator is defined as

$$\hat{\rho} = |\psi\rangle\langle\psi| \tag{2.13}$$

Now let's consider a two level quatum system with a basis $\{|\psi_1\rangle, |\psi_2\rangle\}$. An arbitrary pure state of the system is then written as

$$|\psi\rangle = c_1|\psi_1\rangle + c_2|\psi_2\rangle \tag{2.14}$$

The density operator associated with this state is

$$\begin{aligned} |\psi\rangle\langle\psi| &= (c_1|\psi_1\rangle + c_2|\psi_2\rangle)\left(c_1^*\langle\psi_1| + c_2^*\langle\psi_2|\right) \\ &= |c_1|^2|\psi_1\rangle\langle\psi_1| + c_1c_2^*|\psi_1\rangle\langle\psi_2| + c_1^*c_2|\psi_2\rangle\langle\psi_1| + |c_2|^2|\psi_2\rangle\langle\psi_2| \end{aligned} \tag{2.15}$$

This density operator can be represented by a matrix

$$\hat{\rho} = \begin{pmatrix} |c_1|^2 & c_1c_2^* \\ c_1^*c_2 & |c_2|^2 \end{pmatrix} \tag{2.16}$$

The diagonal terms $|c_1|^2$ and $|c_2|^2$ give the probability of the system to be in state $|\psi_1\rangle$ and state $|\psi_2\rangle$ respectively. For a system with a large number of particles, the probability to be in one particular state becomes the number of particles in that specific state, i.e. how this specific state is populated. Thus the diagonal terms are called populations. The off-diagonal terms are called coherence and contains information about the phase of the quantum state.

The time evolution of the density operator can be obtain from Schrödinger equation, one gets the Liouville-von-Neumann equation:

$$\begin{aligned} \dot{\hat{\rho}} &= |\dot{\psi}\rangle\langle\psi| + |\psi\rangle\langle\dot{\psi}| \\ &= \frac{1}{i\hbar}\hat{H}|\psi\rangle\langle\psi| + \frac{1}{(-i\hbar)}|\psi\rangle\langle\psi|\hat{H} \\ &= \frac{1}{i\hbar}\left[\hat{H}, \hat{\rho}\right] \\ &= -\frac{i}{\hbar}\left[\hat{H}, \hat{\rho}\right] \end{aligned} \tag{2.17}$$

This formalism is equivalent to the Schrödinger equation formalism and does not yet include incoherent processes. However it is well suited to do so because it describes the evolution of the quantum system through its density matrix which allows to easily implement decoherence as the coherences appear explicitely in the density matrix.

The Lindblad equation is obtained from the Liouville-von-Neumann equation by adding additional terms to add incoherent processes. It is written as follow:

$$\dot{\hat{\rho}} = -\frac{i}{\hbar}\left[\hat{H}(t), \hat{\rho}(t)\right] + \sum_n \frac{1}{2}\left[2\hat{C}_n\hat{\rho}(t)\hat{C}_n^\dagger - \hat{\rho}(t)\hat{C}_n\hat{C}_n^\dagger - \hat{C}_n^\dagger\hat{C}_n\hat{\rho}(t)\right] \tag{2.18}$$

where the $\hat{C}_n$ are the collapse operators associated to the n incoherent processes taking place. These operators have the following form $\hat{C}_n = \gamma_n \hat{A}_n$ where γ_n is the "rate" of collapse and $\hat{A}_n$ is the coupling operators between different states of the system. One example of incoherent process which will be used in this master thesis is the spontaneous emission process. We negletected spontaneous emission by not using a quantum description of the electromagnetic field and the Lindblad formalism allows us to put it back in the form of a collapse operator. In the case of spontaneous emission we have $\gamma_{spont} = \sqrt{\Gamma_{spont}}$ where Γ_{spont} is the rate of photon emission.

2.1.3 Diatomic molecules as quantum systems

We aim at explaining the absorption lineshape of a simple quantum system: the HD molecule. More precisely HD is a diatomic molecule. Consequently here is presented the basics of spectroscopy of such molecules.

The motion of a molecule can be decomposed, like any other physical object that is not "pointlike", into a translation, a rotation around the center of mass and a deformation relative to the center of mass. In spectroscopy the modification of the translation part of the motion is due to the gain or loss of momentum when absorbing or emitting a photon. The exchange of momentum with light is used to trap atoms for example. The rest of the motion, i.e. the rotation and the deformation, can also be modified by the absorption or emission of photons. For a diatomic molecule the deformation reduces to a vibration of the length of the unique chemical bond in the molecule. One then talks about rotational and rovibrational transitions. The mathematical development presented here follows the one done in the textbook [16].

Rotational spectroscopy of diatomic molecules

First we consider the pure rotational transitions. The HD molecule can thus be represented by a rigid rotor model, known as the "dumbbell model" shown in fig. 2.1. In quantum mechanics we are interested in the energy level of the system. From classical mechanics we can write the energy of rotation of such a system as:

$$E_{rot} = \frac{1}{2}I\omega \tag{2.19}$$

where I is the moment of inertia and ω the angular velocity of the system around the center of mass. The moment of inertia is given by

$$I = m_H R_H^2 + m_D R_D^2 \tag{2.20}$$

and the two radius R_H and R_D are equal to

$$R_H = \frac{m_D}{m_H + m_D}R \tag{2.21}$$

$$R_D = \frac{m_H}{m_H + m_D}R \tag{2.22}$$

with $R = R_H + R_D$. These last two equations can be used in the formula of the moment of inertia and one finds

$$I = \frac{m_H m_D}{m_H + m_D} R^2 = \mu R^2 \tag{2.23}$$

This result shows that the problem is mathematically equivalent to a unique mass μ rotating at a distance R from the center of mass of the system.

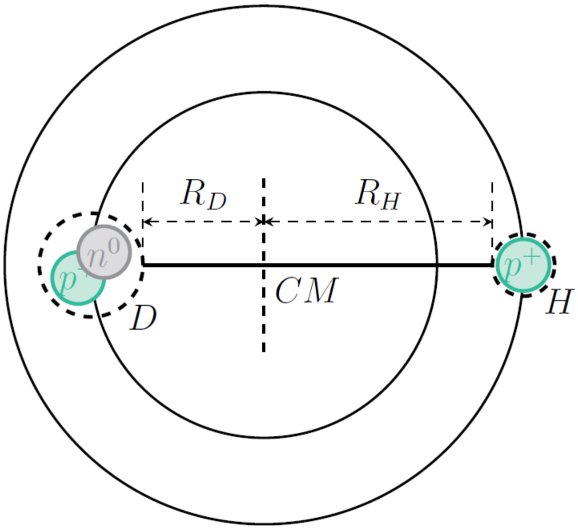

Figure 2.1: Dumbbell model of the HD diatomic molecule. CM is the center of mass. R_D and R_H are the radii of the circular trajectory, of D and H respectivelly, around the center of mass.

The quantum mechanical treatment of a single mass μ is given by the following Schrödinger equation:

$$E\psi = -\frac{\hbar^2}{2\mu} \nabla^2 \psi \tag{2.24}$$

We now use spherical coordinates because of the symmetry of the problem. Moreover as we consider a rigid rotor model the derivative with respect to the radial coordinate must vanish. One thus obtain:

$$E\psi\left(\theta, \phi\right) = -\frac{\hbar^2}{2\mu R^2} \left[\frac{1}{\sin\theta} \frac{\partial}{\partial\theta} \left(\sin\theta \frac{\partial}{\partial\theta} + \frac{1}{\sin^2\theta} \frac{\partial^2}{\partial\phi^2} \right) \right] \psi\left(\theta, \phi\right) \tag{2.25}$$

which can be rewritten using the rotational angular momentum operator $\hat{\vec{J}}$

$$E\psi\left(\theta, \phi\right) = \frac{\hbar^2}{2\mu R^2} \hat{\vec{J}}^2 \psi\left(\theta, \phi\right) \tag{2.26}$$

The solution of this Schrodinger equation are the spherical harmonic Y_{JM} and using the eigenvalue of the operator $\hat{\vec{J}}$ we find

$$\frac{\hbar^2 \hat{\vec{J}}}{2I} Y_{JM} = \frac{\hbar^2}{2I} J(J+1) Y_{JM} \tag{2.27}$$

We now define the rotational constant B as follow:

$$B = \frac{1}{h} \frac{\hbar^2}{2I} \tag{2.28}$$

The rotational quantum number J takes values $J = 0, 1, 2, ...$, and so the rotational energy $F(J) = BJ(1 + J)$ takes value $0, 2B, 6B, ...$ Also, as stated in [16]: "for a diatomic molecule possessing a permanent electric dipole moment, transitions between the rotational levels obey the simple selection rule $\Delta J = \pm 1$".

Harmonic and anharmonic vibrations of diatomic molecules

The mathematical treatment of the harmonic vibration of a diatomic molecule is to first order equivalent to the quantum harmonic oscillators. We will thus only recall one of the main result which is the value associated to the different energy levels:

$$E_v = \left(v + \frac{1}{2}\right) \hbar\nu \tag{2.29}$$

where v is the vibrational quantum number and ν is given by

$$\nu = \frac{1}{2\pi} \left(\frac{k}{\mu}\right)^{\frac{1}{2}} \tag{2.30}$$

where k is the stiffness constant of the restoring force associated to the harmonic potential.

The issue with the harmonic potential is that it fails to take into account that when the nuclei are getting away from each other the restoring force diminishes at some point and goes to zero at infinity. To improve this behavior one must consider an anharmonic potential. A particularly important one according to [16] is the *Morse* potential:

$$V(R) = D_e \left(1 - \frac{1}{e^{\beta(R-R_e)}}\right)^2 \tag{2.31}$$

where β is a constant and D_e is the dissociation energy of the molecule. The shape of this potential is shown on figure 2.2. This potential gives the following energy with a quadratic correction term:

$$G(v) = \lambda_e \left(v + \frac{1}{2}\right) - \lambda_e x_e \left(v + \frac{1}{2}\right)^2 \tag{2.32}$$

where λ_e is the wavenumber of the zero-point energy $\frac{1}{2}hc\lambda_e$ and x_e a constant related to the parameters of the *Morse* potential D_e and β. A more general treatment gives higher order correction terms

$$G(v) = \lambda_e \left(v + \frac{1}{2}\right) - \lambda_e x_e \left(v + \frac{1}{2}\right)^2 + \lambda_e y_e \left(v + \frac{1}{2}\right)^3 + ... \tag{2.33}$$

The quadratic and higher order terms lead to a decrease of the spacing of the vibrational energy levels. Again y_e is a constant related to the parameters of the potential considered.

Rovibrational spectroscopy of diatomic molecules

So far we considered the rotation of the molecule and its vibration to be independant. However, the vibrational motion is coupled to the rotational motion. Indeed, as the diatomic molecule vibrates, its moment of inertia changes due to the change in length of the chemical bound. This change in the moment of inertia could not be taken into account in the rigid rotor model. This coupling between the two motions can be included to obtain a better model than what

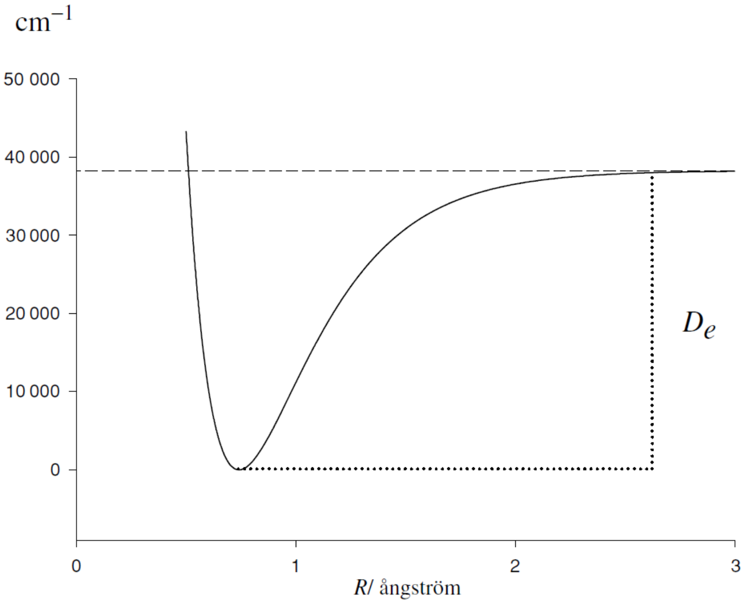

Figure 2.2: Anharmonic potential of a diatomic molecule. The potential tends to an asymptotic value when the two nuclei are far away. The difference between the potential far away and the minimum is the potential energy of the chemical bound and is linked to the dissociation energy. Image from [16].

was presented before. This is done in [16] and we will, once again, follow the mathematical development of this textbook.

Now we consider a non-rigid model of the diatomic molecule. The angular momentum of the diatomic molecule is

$$L = I\omega^2 = \mu R_c^2 \omega^2 \tag{2.34}$$

wiht R_c the radius of the rotation elongated by the centrifugal force F_c and thus differs from the one at equilibrium R_e. This centrifugal force is given by

$$F_c = \mu\omega^2 R_c = \frac{L^2}{\mu R_c} = k(R_c - R_e) \tag{2.35}$$

where k is the stiffness of the equivalent restoring force associated to the harmonic potential approximation of the chemical bond potential. From there we obtain

$$R_c - R_e = \frac{L^2}{\mu R_c^3 k} \tag{2.36}$$

Compared to the rigid model there is now a potential energy component in the total energy of the system. The total energy is equal to

$$E = \frac{L^2}{2I_c} + \frac{1}{2}k\left(R_c - R_e\right)^2 = \frac{L^2}{2\mu R_c} + \frac{1}{2}k\left(R_c - R_e\right)^2 \tag{2.37}$$

We can now substitute $R_c - R_e$ with eq (2.36) and find

$$E = \frac{L^2}{2\mu R_c^2} - \frac{L^4}{2\mu^2 R_c^6 k} \simeq \frac{L^2}{2\mu R_e^2} - \frac{L^4}{2\mu^2 R_e^6 k} + ... \tag{2.38}$$

The approximation comes from a Taylor expansion of the denominator in $(R_c - R_e)$. Neglecting all higher order terms than the zero order term is equivalent to setting $R_c = R_e$.

Now we switch to quantum mechanics. The operator $\hat{\vec{J}}^2$ has the eigenvalue $J(J+1)$ and thus $L^2 = \hbar J(J+1)$. Hence the total energy becomes

$$E = \frac{\hbar^2}{2\mu R_e^2} J(J+1) - \frac{\hbar^4}{2\mu^2 R_e^6 k} J^2(J+1)^2 \tag{2.39}$$

and if we consider higher order terms in the Taylor expansion 2.38 the rotational terms can be generally written as

$$F(J) = BJ(J+1) - DJ^2(J+1)^2 + HJ^3(J+1)^3 + ... \tag{2.40}$$

The new parameters D, H, ... compared to the rigid-rotor model are called centrifugal distortion corrections.

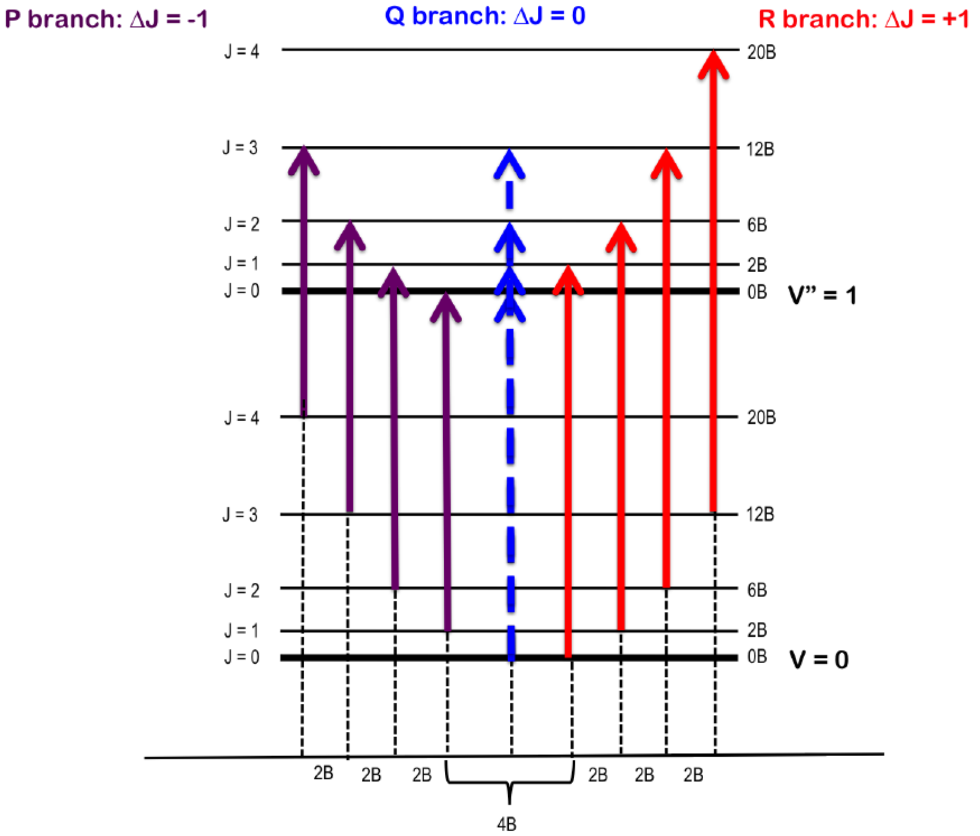

Figure 2.3: Rovibrational energy levels of a diatomic molecule. On the horizontal axis are the energy separation between the transition. For example the $P(1)$ $(1-0)$ transition has $\Delta E = 2hB$ and the $P(2)$ $(1-0)$ transition has $\Delta E = 4hB$. Thus the two transition are separated by $2hB$. Image from [17].

Eventually we consider the vibration of the molecule. The length of the chemical bond changes over time and one thus consider the average length in time to compute B_v, D_v, etc... This average length is different from the equilibrium length due to the anharmonicity of the potential. For B_v one gets

$$B_v = \frac{h}{8\pi^2 c\mu} \left[\overline{\frac{1}{R^2}}\right] \tag{2.41}$$

The bar over $1/R^2$ means that we take the average value over time. From the point of view of quantum mechanics we take the expectation value. The rotational term becomes

$$F_v(J) = B_v J(J+1) - D_v J^2(J+1)^2 + H_v J^3(J+1)^3 + ... \tag{2.42}$$

The total term value are then

$$\begin{aligned} T = G(v) + F_v(J) = \omega_e \left(v + \frac{1}{2}\right) - \omega_e x_e \left(v + \frac{1}{2}\right)^2 + \omega_e y_e \left(v + \frac{1}{2}\right)^3 + ... \\ + B_v J(J+1) - D_v J^2 (J+1)^2 + H_v J^3 (J+1)^3 + ... \end{aligned} \tag{2.43}$$

This constitutes the energy spectrum of rovibrational energy levels of a diatomic molecule. Due to the selection rule on the rotational energy levels $\Delta J = \pm 1$, the allowed transition are divided into 3 groups: the R branch that corresponds to rovibrational transition with $\Delta J = +1$, the P branch that corresponds to rovibrationnal transition with $\Delta J = -1$ and also the Q branch that corresponds to purely vibrational transitions with $\Delta J = 0$. A graphical depiction of these transitions is shown in fig. 2.3. Note that this schematics omits the corrections of the non rigid model.

In this master thesis we aim at explaining the asymmetric lineshape of the R(1) (2-0) rovibrational transition of the HD molecule. The "(2-0)" in the notation refers to the vibrational part of the rovibrational transition. It means that the transition is from the 0 vibrational level to the 2 vibrational level. The "R" means that the transition belongs to the R branch and thus corresponds to $\Delta J = +1$ and the "(1)" in "R(1)" means the lower state of the transition has $J = 1$. Thus this transition is from $J = 1$ to $J = 2$.

2.1.4 Basics features of 2-level spectroscopy

Now, we will focus on a 2-level quantum system. The mathematical treatment of this problem follows the one done in [18]. The lower energy state will be called $|\psi_1\rangle$ and the upper energy state $|\psi_2\rangle$. These two states are the stationary states of the Hamiltonian $\hat{H}_0$ that describes the quantum system without external perturbation such as the electromagnetic field. For this reason they can be rewritten as

$$|\psi_1\rangle = \psi_1(\vec{r}) e^{-i\frac{E_1}{\hbar}t} \tag{2.44}$$

$$|\psi_2\rangle = \psi_2(\vec{r}) e^{-i\frac{E_2}{\hbar}t} \tag{2.45}$$

where $\psi_1(\vec{r})$ and $\psi_2(\vec{r})$ are the spatial part of the wave function $|\psi_1\rangle$ and $|\psi_2\rangle$ respectively and E_1 and E_2 are the energy associated to the level 1 and 2 respectively. We adopt the following notation $\psi_i(\vec{r}) = |i\rangle$ and $E_i/\hbar = \omega_i$. The wave function can be described at any time as a linear combination of the two stationary states:

$$|\psi\rangle = c_1(t) e^{-i\omega_1 t} \,|1\rangle + c_2(t) e^{-i\omega_2 t} \,|2\rangle \tag{2.46}$$

with $|c_1|^2 + |c_2|^2 = 1$ at every instant.

The presence of an electromagnetic field is taken into account through $\hat{H}_{int} = -\hat{D} \cdot \vec{E}(\vec{r}_0, t)$ as seen previously. We consider a purely monochromatic electromagnetic wave $\vec{E}(t) = \vec{E}_0 \cos(\omega t)$. Then the Schrödinger equation takes the form

$$i\dot{c}_1 = \Omega_R \cos(\omega t) e^{-i\omega_0 t} c_2 \tag{2.47}$$

$$i\dot{c}_2 = \Omega_R^* \cos(\omega t) e^{i\omega_0 t} c_1 \tag{2.48}$$

where $\omega_0 = (E_2 - E_1)/\hbar$ and

$$\Omega_R = \frac{\langle 1 | q(\hat{\vec{r}} - \vec{r}_0) \cdot \vec{E}_0 | 2 \rangle}{\hbar} = \frac{q}{\hbar} \int \psi_1^*(\vec{r}) \vec{r} \cdot \vec{E}_0 \psi_2(\vec{r}) d^3 r \tag{2.49}$$

The frequency Ω_R is an important quantity in quantum optics and it is called the Rabi frequency. If we suppose that the electric field polarisation is along the x axis then we can write

$$\Omega_R = \frac{qX_{12}|E_0|}{\hbar} \tag{2.50}$$

with $X_{12} = \langle 1|x|2\rangle$.

Now we express the $\cos(\omega t)$ as a sum of exponentials

$$i\dot{c_1} = \Omega_R\{\frac{e^{i\omega t} + e^{-i\omega t}}{2}\}e^{-i\omega_0 t}c_2$$
$$i\dot{c_2} = \Omega_R^*\{\frac{e^{i\omega t} + e^{-i\omega t}}{2}\}e^{i\omega_0 t}c_1$$

and obtain

$$i\dot{c_1} = \frac{\Omega_R}{2}\{e^{i(\omega-\omega_0)t} + e^{-i(\omega+\omega_0)t}\}c_2 \tag{2.51}$$
$$i\dot{c_2} = \frac{\Omega_R^*}{2}\{e^{i(\omega+\omega_0)t} + e^{-i(\omega-\omega_0)t}\}c_1 \tag{2.52}$$

In each equation there is a term that oscillates at the frequency $\omega + \omega_0$ and another one that oscillates at $\omega - \omega_0$. The term with the $\omega + \omega_0$ frequency oscillates much faster and thus "average to zero over any reasonable interaction time" according to [18]. We can thus neglect it. Moreover we define $\delta = \omega - \omega_0$ as the detuning and we obtain the following equations

$$i\dot{c_1} = \frac{\Omega_R}{2}e^{i\delta t}c_2 \tag{2.53}$$
$$i\dot{c_2} = \frac{\Omega_R^*}{2}e^{-i\delta t}c_1 \tag{2.54}$$

This system of equations can be solved easily. A combination of these two equations gives an ordinary differential equation with constant coefficients

$$\frac{d^2}{dt^2}c_2 + i\delta\frac{d}{dt}c_2 + \left|\frac{\Omega_R}{2}\right|^2 c_2 = 0 \tag{2.55}$$

The solution of this equation with initial conditions that correspond to the quantum system initially in the lower energy level, $c_1(t = 0) = 1$ and $c_2(t = 0) = 0$, is

$$|c_2(t)|^2 = \frac{\Omega_R^2}{\Omega^2}\sin^2\left(\frac{\Omega t}{2}\right) \tag{2.56}$$

with Ω the generalized Rabi frequency given by $\Omega^2 = \Omega_R^2 + \delta^2$. The probability of finding the state in the upper energy level oscillates through time at half the generalized Rabi frequency. This phenomenon is called Rabi oscillations. These oscillations are represented on fig. 2.4. Because of the normalisation of the probability, this means that the probability of finding the quantum system in the lower energy state oscillates accordingly. The full solution is

$$c_1(t) = e^{i(\delta/2)t}\left(\cos\left(\frac{\Omega t}{2}\right) - \frac{i\delta}{\Omega}\sin\left(\frac{\Omega t}{2}\right)\right) \tag{2.57}$$
$$c_2(t) = e^{-i(\delta/2)t}\left(\frac{-i\Omega_R}{\Omega}e^{i\phi}\sin\left(\frac{\Omega t}{2}\right)\right) \tag{2.58}$$

The amplitude of the oscillations depends on the detuning of the electromagnetic wave with respect to the transition frequency ω_0 of the system. At resonance, i.e. $\delta = 0$ and $\omega = \omega_0$, the amplitude of the oscillations is one. This situation is shown in fig. 2.4. For a single atom or molecule, this means that the total probability switches from being in one state to being in the other state. For a large amount of particles the probability of excitation can be interpreted as a ratio of the number of particles excited over the total number of particles. This means that the occupation the two energy levels oscillates between being full and being empty.

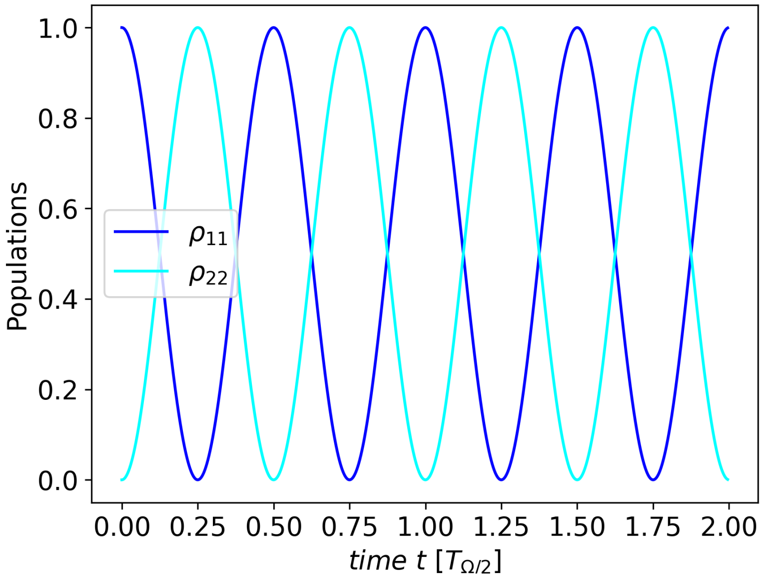

Figure 2.4: Oscillations of the populations with an electric field oscillating at resonance. We see that the populations oscillate at the Rabi frequency and that the amplitude of the oscillations is equal to unity.

The evolution described so far is a coherent evolution following the dynamic of the Schrödinger equation. It describes the processes of stimulated absorption and stimulated emission schematically represented in fig. 2.5. It does not take into account the spontaneous emission process which is a incoherent evolution as explained before.

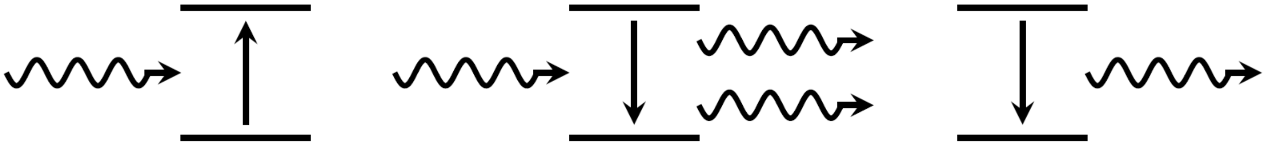

Figure 2.5: Left: Stimulated absorption, Middle: Stimulated emission, Right: Spontaneous emission

The spontaneous emission process can be easily introduced into the Bloch equation formalism. To reformulate the problem into this formalism we make the following change of variable

$$\tilde{c}_1 = c_1 e^{-i\delta t/2} \tag{2.59}$$

$$\tilde{c}_2 = c_2 e^{i\delta t/2} \tag{2.60}$$

The density matrix then becomes

$$\tilde{\rho} = \begin{pmatrix} \tilde{\rho}_{11} = \rho_{11} & \tilde{\rho}_{12} = \rho_{12} e^{-i\delta t} \\ \tilde{\rho}_{21} = \rho_{21} e^{i\delta t} & \tilde{\rho}_{22} = \rho_{22} \end{pmatrix} \tag{2.61}$$

Now we define new variables as

$$u = \tilde{\rho}_{12} + \tilde{\rho}_{21} \tag{2.62}$$

$$v = -i \left(\tilde{\rho}_{12} - \tilde{\rho}_{21} \right) \tag{2.63}$$

$$w = \rho_{11} - \rho_{22} \tag{2.64}$$

These new variables allow to rewritte eqs 2.53 and 2.54 as

$$\dot{u} = \delta v \tag{2.65}$$

$$\dot{v} = -\delta u + \Omega_R w \tag{2.66}$$

$$\dot{w} = -\Omega_R v \tag{2.67}$$

Note that we now have three equations. The reason is that we have replaced two complex equations with a normalisation condition, so three degrees of freedom, by three equations on real valued variables.

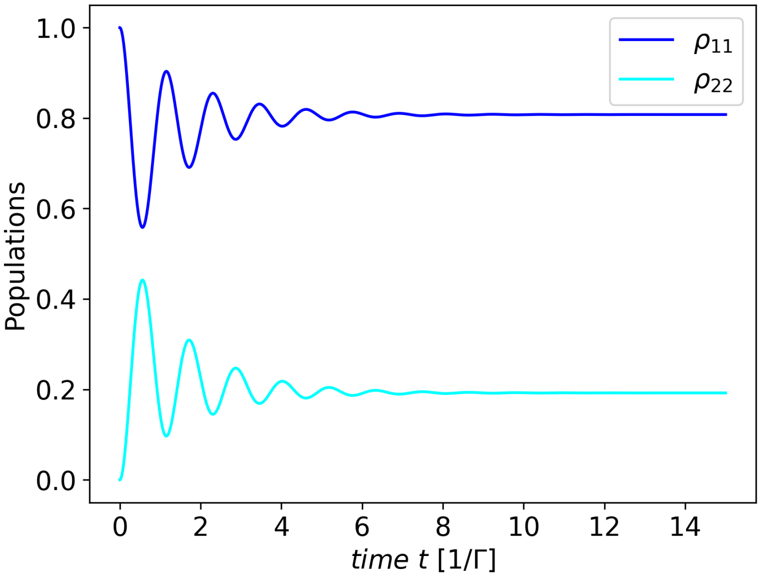

Figure 2.6: Evolution of the populations when spontaneous emission is considered. For this figure the detuning of the laser frequency δ is such that $\delta/\Gamma \approx 3.6$ and $\delta/\Omega_R \approx 0.9$.

Eventually we can add damping terms on this oscillating quantum system that represent the spontaneous emission or, any other incoherent process, based on an analogy with the damping of a classical oscillators. This gives a set of equations known as the optical Bloch equations (which is equivalent to the Lindblad equation writtent for such a 2-level quantum system):

$$\dot{u} = \delta v - \frac{\Gamma}{2} u \tag{2.68}$$

$$\dot{v} = -\delta u + \Omega_R w - \frac{\Gamma}{2} v \tag{2.69}$$

$$\dot{w} = -\Omega_R v - \Gamma(w - 1) \tag{2.70}$$

Where Γ^{-1} is the characteristic lifetime of the upper energy level. For a time much longer than this lifetime the solution converges towards a steady state solution which is

$$\begin{pmatrix} u \\ v \\ w \end{pmatrix} = \frac{1}{\delta^2 + \Omega_R^2/2 + \Gamma^2/4} \begin{pmatrix} \Omega_R \delta \\ \Omega_R \Gamma/2 \\ \delta^2 + \Gamma^2/4 \end{pmatrix} \tag{2.71}$$

For the population of the upper energy level, this steady state solution gives

$$\rho_{22} = \frac{1-w}{2} = \frac{\Omega^2/4}{\delta^2 + \Omega_R^2/2 + \Gamma^2/4} \tag{2.72}$$

A graphical representation of the evolution with spontaneous emission is shown in fig. 2.6. We see that the populations oscillate within an exponentially decaying envelope that leads to a stationary state of the populations.

2.1.5 Basics of absorption spectroscopy

When an electromagnetic wave goes through a medium, some part of the energy carried by the wave can be absorbed by this medium. As seen in the previous section, for such a radiative transition to occur, the medium must possess energy levels that allow a transition from two of its energy levels with a difference in energy corresponding to the energy carried by the photons of the wave. To study this transfer of energy, one uses the amount of energy carried by the wave by unit time and unit surface, i.e. the intensity I. Neglecting nolinear effects, the loss endured by the electromagnetic wave is proportional to the intensity and the proportionality constant is the absorption coefficient α. Thus, if the electromagnetic wave travels along the z axis, the evolution of the intensity is given by

$$\frac{dI}{dz}(\omega, z) = -\alpha(\omega) I(\omega, z) \tag{2.73}$$

After integration one obtain what is known as Beer's Law

$$I(\omega, l) = I(\omega, 0) e^{-\alpha(\omega) l} \tag{2.74}$$

where l is the length over which the electromagnetic wave interacted with the medium.

We would like to link the absorption coefficient to the quantum properties of the medium. We will follow here the mathematical development of [19]. First let's make a link between the absorption coefficient and the dielectric susceptibility of the medium. The absorption coefficient corresponds to twice the imaginary part of the wavevector

$$k = k' + ik'' \tag{2.75}$$

Indeed, the imaginary part of the wavevector gives the exponential decay of the electric field and the intensity is proportional to the square of the electric field amplitude. Hence the square of the exponential decay is $\left(e^{-k''z}\right)^2 = e^{-2k''z}$ and thus $\alpha \equiv 2k''$. The wavevector itself is linked to the refractive index through the relation

$$k = n\frac{\omega}{c} \tag{2.76}$$

and, eventually, the refractive index is linked to the dielectric susceptibility of the medium

$$n^2 = 1 + \chi \tag{2.77}$$

This dielectric susceptibility is thus also a complex number and so $\chi = \chi' + i\chi''$. For a dilute gas, the susceptibility is small compared to unity [19] and thus

$$n \simeq 1 + \frac{\chi'}{2} + i\frac{\chi''}{2} \tag{2.78}$$

Using equations (2.75)(2.76) (2.78) we find

$$k' + i\frac{\alpha}{2} \simeq \left(1 + \frac{\chi'}{2} + i\frac{\chi''}{2}\right)\frac{\omega}{c} \tag{2.79}$$

and thus

$$\alpha \simeq \chi''\frac{\omega}{c} \tag{2.80}$$

Now, we can make the link with the quantum description of the medium. The macroscopic polarization of the medium is related to the microscopic polarization of each individual quantum system. For a dilute gas of non-interacting atoms or molecules with number density N, in the absence of external perturbation other than the electromagnetic field, we have

$$\vec{P} = \langle\hat{\vec{D}}\rangle N \tag{2.81}$$

where $\langle\hat{\vec{D}}\rangle$ is the expectation value of the polarization of a single quantum system. It is equal to

$$\langle\hat{\vec{D}}\rangle = \langle\psi|\hat{\vec{D}}|\psi\rangle \tag{2.82}$$

Once the polarization is computed from the quantum expectation value of the dipole moment operator, $\langle\hat{\vec{D}}\rangle$, we can compare it to the macroscopic formulation of the polarization, which is

$$\vec{P} = \epsilon_0\left[\chi'\vec{E}_0\cos(\omega t + \phi) + \chi''\vec{E}_0\sin(\omega t + \phi)\right] \tag{2.83}$$

for an incident electromagnetic wave of the form $\vec{E}_0\cos(\omega t + \phi)$.

If we consider a single 2-level quantum system as before then the dielectric susceptibility has an analytical solution [20]:

$$\chi = N\frac{X_{12}^2}{\epsilon_0\hbar}\frac{\omega_0 - \omega + i\Gamma/2}{\Gamma^2/4 + \Omega_R^2/2 + (\omega - \omega_0)^2} \tag{2.84}$$

this formula is a Lorentzian function of the detuning $\delta = \omega - \omega_0$. The imaginary part of this formula is represented graphically in fig. 2.7. The peak of the Lorentzian function is centered on ω_0 and the full width at half maximu (FWHM) is given by

$$\Delta\omega_{\text{FWHM}} = \Gamma\left(1 + \frac{I}{I_{sat}}\right)^{1/2} \tag{2.85}$$

where I is the intensity of the electromagnetic wave and I_{sat} the saturation intensity of the absorbing particle [21]. The saturation phenomenon will be discussed later.

In a real absorption experiment, one typically measure the absorption of a gaseous medium. Now we will follow the mathematical treatment done in [22]. The absorption is then the sum of the absorption from each individual particle. Each particle will have a Lorentzian contribution to the total absorption but the total absorption lineshape will not be a Lorentzian. The particles in the gas are not at rest and the velocity distribution is given for example by

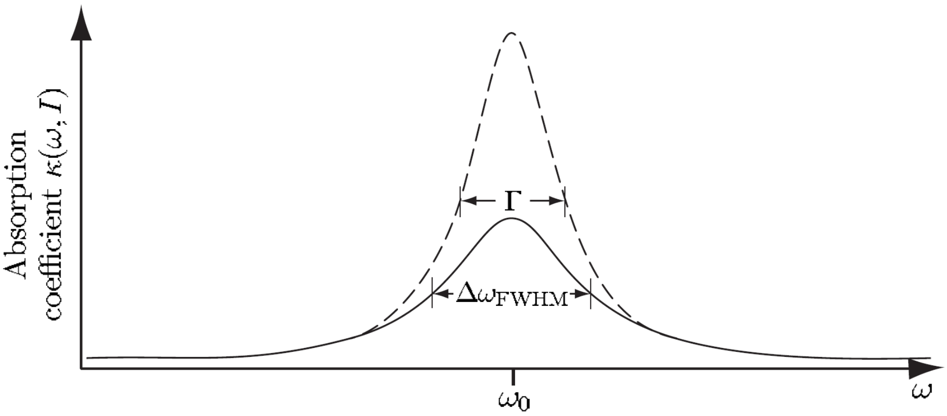

Figure 2.7: Lineshape of the absorption coefficient of a single quantum system with two levels, including spontaneous emission from the upper energy level. This single quantum system is illuminated by an idealized perfectly monochromatic laser source. The shape is a Lorentzian function and it is centred on $\omega_{laser} = \omega_0$. The FWHM is Γ when the intensity is well below the saturation intensity. If the intensity is higher than the saturation intensity then the absorption decreases and the FWHM increases according to eq. 2.85. Image from [21].

the Maxwell Boltzmann law. The velocity of a particle will generate a Doppler shift of the perceived frequency of the laser and thus a shift of the Lorentzian along the horizontal axis relative to the laser frequency. Only the velocity component along the laser beam propagation axis will generate a Doppler shift. For this reason one considers the Maxwell Boltzmann velocity distribution along one axis, let's call it z.

$$f(v_z)dv_z = \sqrt{\frac{m}{2\pi k_B T}}\; e^{-\frac{mv_z^2}{2k_BT}} dv_z \tag{2.86}$$

The resulting absorption lineshape for a gas will be the convolution of the Lorentzian profile with the velocity distribution along the beam axis

$$\chi'' = \int_{-\infty}^{+\infty} f(v_z)\chi''_{\mathrm{Lorentz}}(\omega - kv_z)\; dv_z \tag{2.87}$$

Such a broadened lineshape is represented in the upper part of panel (b) of fig. 2.9. The graph is “upside down” compared to the one previously shown of the Lorentzian lineshape. The reason is that on the graphs of fig. 2.9 the quantity depicted is the signal monitored after absorption and is thus the transmission of the medium as a function of the wavelength. However the lineshape of the transmission and the one of the absorption are obviously similar and directly related.

A broadened absorption signal is less effective for experimental measure of the transition frequency of the medium. The broadening modifies the absorption such that it is not anymore exclusively determined by the properties of the quantum system under study but also determined by the statistical distribution of velocities and thus by the temperature and pressure of the sample. The FWHM with Doppler broadening is given by [22]:

$$\Delta f_{\mathrm{Doppler}} = 2\sqrt{\ln(2)}\frac{v_{\mathrm{mp}}}{c} f_0 \tag{2.88}$$

where v_{mp} is the most probable speed in the gas, c the speed of light and f_0 the transition frequency. For example, considering a HD gas at 300 K we get $\Delta f_{\mathrm{Doppler}} \simeq 1.5$ GHz which is significantly higher than the few hundreds of kHz of the Lamp-dip FWHM measured by the Amsterdam research group in [12] (due to the transit time broadening, it will be explained at the end of this section) and even higher when compared to the natural FWHM of a few Hz. This increases the difficulty of extracting a precise value of the transition frequency of the system from experimental data points. One can play with temperature and pressure to minimize this broadening but there is an easier method the get free from this Doppler broadening.

We can get rid of this Doppler broadening thanks to saturated absorption spectroscopy or Lamb-dip spectroscopy. Any medium has a property known as the saturation intensity. Saturation is due to the impossibility of the medium to keep increasing its absorption proportionally to the increase of the incoming intensity when the later is too high. When the incoming intensity is low compared to the saturation intensity any increase of it will be absorbed proportionally. For example if we double the intensity and it is still low compared to the saturation intensity then the medium goes from absorbing αI to absorbing $2\alpha I$. However as the number of excited particles increases the fluorescence increases also. Moreover the increase in the number of excited particles obviously decreases the number of unexcited particles (available for absorbing photons) and this decrease makes it more and more difficult to absorb more photons. The populations of excited particles ρ_{22} (and unexcited ones ρ_{11}) converges asymptotically towards 0.5. When the magnitude of the intensity is equal to the saturation intensity, any further increase of the incoming intensity will be accompanied by a greater increase of fluoresence and absorption will start to decrease. This is shown in fig. 2.7 where the dashed curve is the absorption bellow saturation and the full curve is the absorption above saturation.

The idea in saturated spectroscopy is to use a pump laser and a probe laser. The pump laser has a very high intensity such that it saturates the medium. At an arbitrary frequency close to the transition frequency of the particle at rest in the medium, there is a corresponding amount of particles with the right velocity such that the Doppler shift implies that the perceived frequency in their reference frame is exactly the transition frequency ω_0. If the intensity of the laser is sufficiently high the laser will excites a non negligible amount of the individual particles of the medium around this velocity class of particles. The medium is then less capable of absorbing more photon because many particles are already excited: the medium saturates. The particles of the medium capable of absorbing are the particles in the lower energy state called 1 in fig. 2.9. The number density of particles in this state is named accordingly N_1. We can see in this figure that the laser has “burned a hole” in the velocity distribution of the lower energy state particles. For this reason the medium becomes partially transparent to a frequency of the probe linked to the frequency of the pump that caused the saturation.

Once the medium is saturated by the pump laser comes into play the probe laser. The probe is sent through the medium but in the opposite direction. Because the pump laser beam and the probe laser beam are counter propagating, a particle of the medium will perceived the electromagnetic wave of these two lasers with opposite Doppler shifted frequencies as depicted in fig. 2.8. The medium will be transparent for the probe when the frequency of the pump and the frequency of the probe matches in the reference frame of the absorbing particle. In the reference frame of the particle the two lasers have opposite Doppler shifts. Mathematically this means:

$$\omega_{pump} + k_{pump} v_z = \omega_{probe} - k_{probe} v_z \tag{2.89}$$

This implies that there is only one specific velocity for which the partial transparency of the medium will be maximized

$$v_z = \frac{\omega_{probe} - \omega_{pump}}{k_{probe} + k_{pump}} \tag{2.90}$$

This means that the transparency "dip" or "Lamb-dip" in the Doppler broadened absorption lineshape is not sensitive to the Doppler effect. The transparency dip will thus depend solely on the medium properties and have a full width at half maximum equal to the one of the Lorentzian absorption lineshape. Hence the central frequency of the Lamb-dip can be extracted as precisely as the transition frequency would be from data points of a Lorentzian absorption curve.

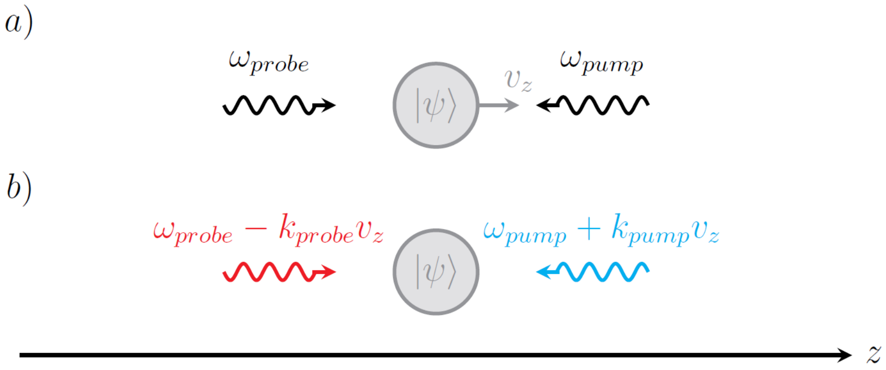

Figure 2.8: Saturated absorption. Representation of the absorption of a photon from the pump laser and a photon from the probe laser. Panel a) reference frame of the laboratory. Panel b) reference frame of the particle.

However there is still a problem, the central frequency of the Lamb-dip is not known and can't be obtained from the transparency dip as it depends on the wavelength chosen for the pump laser. To solve this issue, one use the same frequency for the pump laser and the probe laser. This implies that $\omega_{probe} - \omega_{pump} = 0$ and so

$$v_z = 0 \tag{2.91}$$

The Lamb-dip is now centred on the frequency that corresponds to a null Doppler shift, which means $\omega_{pump} = \omega_0$. The lamb-dip is centred on the transition frequency. This allows to have access to the transition frequency with the same precision as the Lorentzian absorption lineshape would allow. This is known as Doppler free spectroscopy or Lamb-dip spectroscopy. The typical signal of a Doppler free spectroscopy is shown on fig. 2.9

Although Doppler free spectroscopy allows to get rid of the Doppler broadening, there exist other broadening mechanisms that prevent experiments from accessing directly the lowest uncertainty on the transition frequency that is the natural broadening which is an intrinsic property of the quantum system (and the vacuum that surrounds it). Among the other existing broadening mechanisms are the ones induced by the interaction with the laser beam. These are transit time broadening and power broadening. Moreover in a gas, each particle interacts with the other ones through collisions which also induce some collisional broadening. All these processes generate uncertainty on the transition frequency because they all act on the effective lifetime of the upper energy level. The frequency of a sine or cosine is more resolved in frequency when the oscillation lasts over a long period of time. Hence the limiting process will be the one that induces the shortest lifetime for the excited state.

The transit time broadening is due to the finite interaction time between the laser beam and the sample. The reason is that the laser beam has a cross section that is smaller than the cross section of the sample container. Therefore particles of the sample will not interact indefinitely with the laser but rather cross the laser beam from time to time. This finite duration

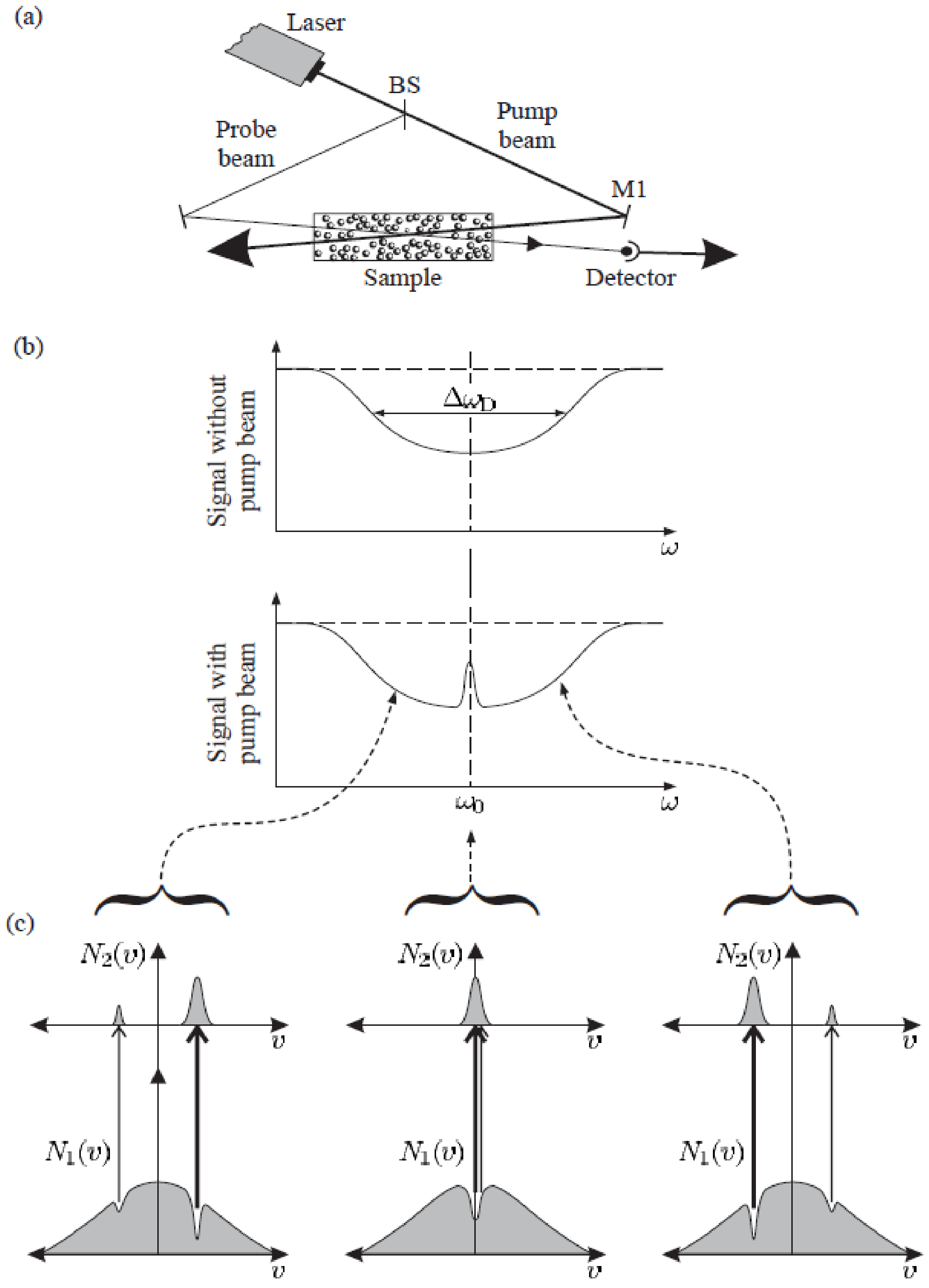

Figure 2.9: Doppler Free Spectroscopy. Panel a) Expirmental setup: the pump laser and the probe laser come from the same source and thus have the same frequency in the laboratory reference frame. They are separated by a beam splitter (BS). Panel b) The Doppler broadened signal (above) and the Doppler free signal (below). Panel c) Representation of the velocity distribution of the particles in the two states respectively. Far from the frequency transition of the quantum system at rest, the pump laser frequency and the probe laser frequency don't match. Image from [22].

interacting window is the transit time.

The power broadening becomes significant when Ω_R is on the order of Γ. The physical reason of the broadening is that the faster the Rabi oscillations the less time is spent in each energy level within one oscillation. The frequency resolution thus decreases as the duration of the occupation of the excited level decreases.

Eventually collisional broadening is due to the finite duration between two collisions that interrupt the coherent evolution of the system. This type of broadening thus depends on the mean free path of the particles and therefore on the pressure inside the gas. Reducing the pressure reduces collisional broadening.

2.2 Experimental methods

In this section, we will cover the main ideas of the experimental setups used by the research teams that are working on the absorption spectrum of HD. The researchers from Amsterdam use a method called noise-immune cavity-enhanced optical heterodyne molecular spectroscopy. The researchers from Heifei use another method called cavity ringdown spectroscopy. These two methods are cavity enhanced absorption spectroscopy. This means that the use of an optical cavity helps to improve the measurement. This improvement is based on the ability of optical cavities to store light at high powers for a considerable amount of time.

An optical cavity is an electromagnetic wave resonator. Let's consider the most simple type of optical cavity: the Fabry Perot cavity. It is made of two mirrors facing each other. The light bounces on the mirrors and it is then trapped in the resonator until it escapes due a non zero probability of crossing the mirrors or due to misalignment with the axis of the resonator. This allows to increase interacting time of the light with a sample if it is placed in the optical cavity because going back and forth many times in the cavity and through the sample is equivalent to going through a very long sample [23].

Inside the cavity the surface of the mirror imposes two boundary conditions that restrict the value of half the wavelength of standing waves to be an integer subdivision of the length of the cavity L_c:

$$n\frac{\lambda_{\text{standing wave}}}{2} = L_c \tag{2.92}$$

The cavity thus filters out some frequencies. This would imply that only very specific frequencies regularly spaced could exist in the cavity. However this is true only for electromagnetic wave that would be trapped indefinitely in the cavity. As it is not the case, the intensity of light transmitted by a Fabry Perot cavity is composed of broadened peak regularly spaced in frequency. The spacing of the peak maxima is called the free spectral range (FSR) because ideally there would be no transmission in between these maxima. It is given (for a medium with constant refractive index n) by

$$\Delta f_{\text{fsr}} \simeq c/nL \tag{2.93}$$

or

$$\Delta\lambda_{\text{fsr}} \simeq \lambda^2/nL \tag{2.94}$$

The time spend by the light in the cavity is determined by the reflectivity and transparency of the mirrors and of course the length of the cavity. The more time the electromagnetic wave is trapped in the cavity the more resolved its frequency is and thus the resolution of the peaks increases. Mathematically this is expressed by the full width at half maximum of the peaks δf. Eventually the finesse $\mathcal{F}$ of the cavity is the quotient of the FSR and δf that measures the ability to easily identify separated peaks of the cavity spectrum.

$$\mathcal{F} = \frac{\Delta f}{\delta f} \tag{2.95}$$

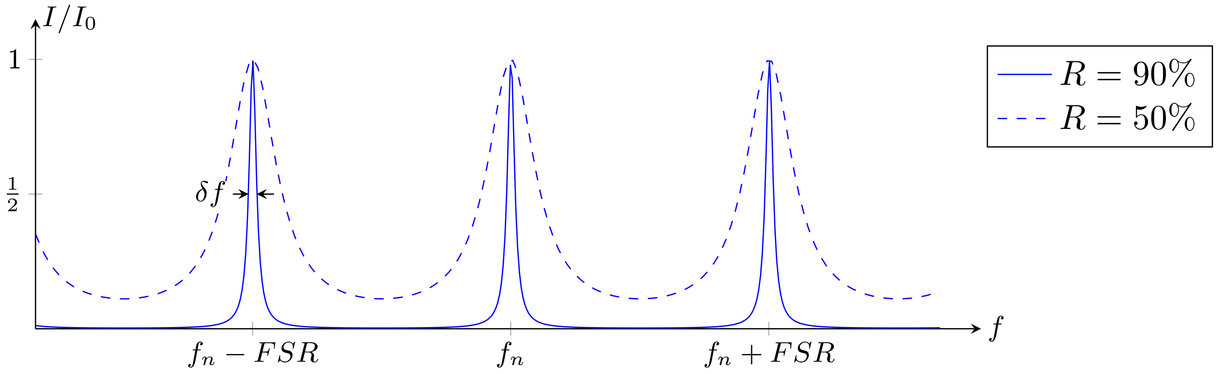

Figure 2.10: Frequency spectrum of a Fabry Perot interferometer with two different finesses. The greater the reflectivity of the mirrors the better the frequency is resolved. Image from [24] (modified).

The previous description of an optical cavity consider two flat mirrors and obviously some light will escape the cavity simply due to misalignment of the wave propagation axis and the cavity axis. To reduce the loss of light due to misalignment it is better to use curved mirrors. Then the standing wave in the cavity can not be plane wave anymore but they must rather adopt a Gaussian profile with wavefront having a curvature that matches the curvature of the mirror at the boundary of the cavity. The study of such electromagnetic wave profile is called Gaussian optics.

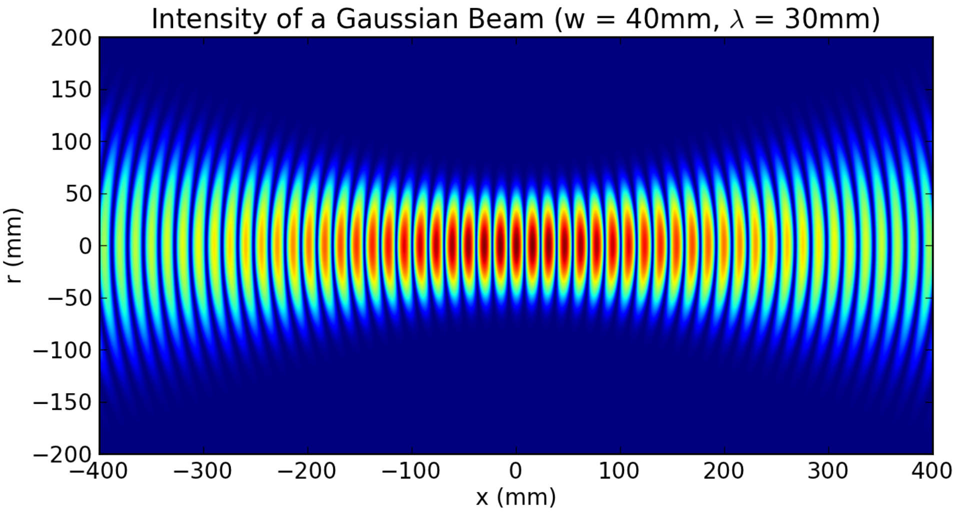

Figure 2.11: Instantaneous absolute value of the real part of electric field amplitude of TEM_{00} Gaussian beam. Image from [25].

In fig. 2.11 is represented the instantaneous amplitude of a transverse electromagnetic mode of order 00 (TEM_{00}). Higher order corresponds to mode TEM_{mn} with m and n that increase as the number of node in the transverse plane (x, y if the z axis is the axis of the cavity) increases. Back to fig. 2.11 we can see the node and maxima of amplitude of the Gaussian beam form curved surfaces transverse to the axis of the cavity. This allows to match the electromagneitc wave with the boundary conditions of the cavity imposed by the curvature of the mirrors. Obtaining the best match between the beam and the cavity is important to maximize the intensity injected in the cavity and this is called mode matching.

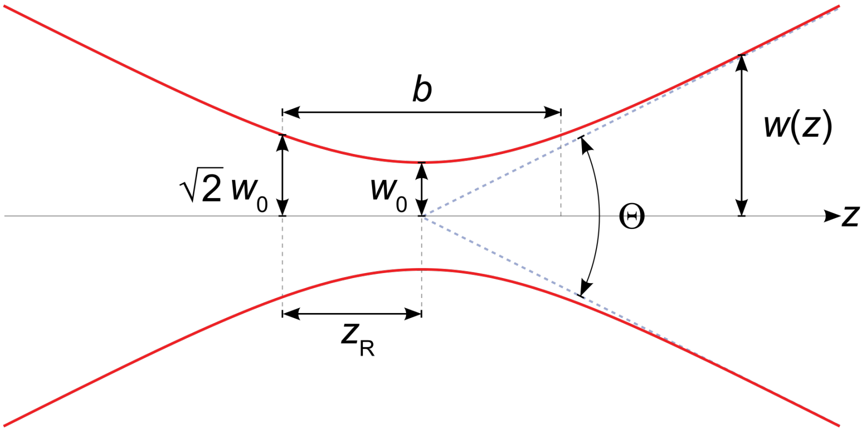

Figure 2.12: Envelope of a Gaussian beam with the parameters that describes it. These are the width $w(z)$, the waist w_0, the Rayleigh distance z_R, the depth of focus b and the total angular spread Θ. Image from [26].

In fig. 2.12 is shown the envelope of a Gaussian beam. This envelope is characterised by a few parameters that are directly related. These are the beam waist w_0, the Rayleigh distance z_R, the total angular spread Θ. The shape of this envelope is however entirely determined by each of these parameters alone for a given wavelength. For this reason the curvature of the mirrors will thus fully determine the shape of the Gaussian beam at this given wavelength. The focusing of the beam at the waist w_0 is thus not arbitrary. Also the divergence of the beam is inversely proportional to the waist size. Thus the more focused the beam the more divergent it is and conversely. This works similarly to an uncertainty principle and Gaussian beams have the smallest uncertainty product between angular spread and beam focusing. For this reason Gaussian beam are said to be diffraction limited [27].

All these properties of Gaussian beams affects the interaction with the sample placed in the cavity. The intensity distribution varies through space in an optical cavity as can be clearly seen in fig. 2.11. This variation happens along the cavity axis and also in the transverse direction. Thus the electric field seen by a particle of the sample as it crosses the beam along an arbitrary direction is not trivial.

2.2.1 The NICE-OHMS method

The Noise-Immune Cavity-Enhanced Optical Heterodyne Molecular Spectroscopy Technique (NICE-OHMS) is a detection technique with high sensitivity. The following description of the method comes from [28].This method allows to monitor a great variety of signals. It produces both Doppler broadened (Db) signal and sub-Doppler signals (sD). Additionnaly it provides both dispersive and absorption signals. Eventually a supplementary wavelength modulation or frequency modulation can be applied to further improve noise reduction.

Optical Heterodyne Molecular Spectroscopy (OHMS) is a method detection that relies on the comparison of a signal that has been interacting with some target sample with a reference signal that oscillates at a different frequency than the signal probing the sample. The offset in frequency between the reference and the wave probing the sample is what heterodyne refers to. If the same source of electromagnetic wave was used to generate a beam probing the sample and a reference beam, via a beam splitter for example, then the reference and the probe would have the same frequency and the detection method would be called homodyne.

NICE-OHMS is thus a detection method that uses different frequency of the electromagnetic spectrum (OHMS) with a noise-immune property (NI) and a cavity-enhanced property (CE). The enhancement of the measurement due to a cavity has been explained in the previous section: a cavity allow a longer interaction time between the sample and the probing beam. The noise immune property relies on the property of what is called Frequency Modulation Spectroscopy (FMS).

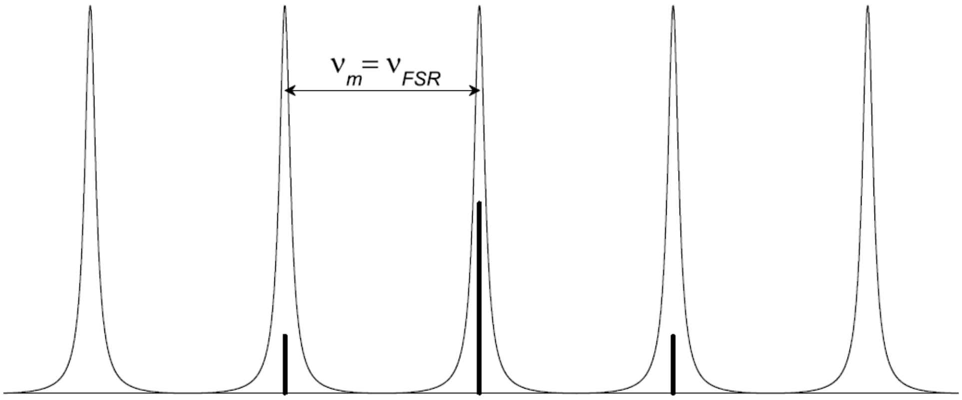

Figure 2.13: The carrier frequency and the two sidebands of an electromagnetic wave in NICE OHMS represented along with the spectrum of the cavity. We see that the sidebands frequencies match with the cavity spectrum such that all frequencies benefits from the cavity enhancement. Image from [28].

In FMS, the electromagnetic wave used to probe the sample is modulated at some frequency f_m:

$$\vec{E}^{\text{fm}}(f_c,t) = \frac{E_0}{2}\vec{\epsilon}e^{i(2\pi f_c t + \beta\sin(2\pi f_m t))} + c.c. \tag{2.96}$$

where E_0 is the amplitude of the electric field, $\vec{\epsilon}$ is the polarization vector, f_c is the carrier frequency (the frequency without modulation), f_m is the modulation frequency and β is called the modulation index. If $\beta < 1$ the beam is mainly composed of three frequency components. These are the carrier frequency f_c and two sidebands at frequencies $f_c \pm f_m$. The amplitudes of these components are given by Bessel functions and the resulting wave is:

$$\vec{E}^{\text{fm}}(f_c,t) = \frac{E_0}{2}\vec{\epsilon}\left[J_0(\beta) + J_1(\beta)e^{i2\pi f_m t} - J_1(\beta)e^{-i2\pi f_m t}\right]e^{i2\pi f_c t} + c.c. \tag{2.97}$$

The sidebands interfere with the carrier and each produces a beat signal. In the absence of sample the beat signal of the lower frequency sideband and the carrier is cancelled by the one of the higher frequency sideband and the carrier. The signal recovered is the intensity at the frequency modulation and thus there is no signal. When there is a sample present along the wave trajectory the balance between the two beat signal is broken and a signal is measured that contains information on the sample response to the wave. Moreover the noise introduced in the wave will be identical for the carrier and the sidebands and the frequency modulation spectroscopy thus cancel automatically the noise signal. This is the noise-immune property of the method.

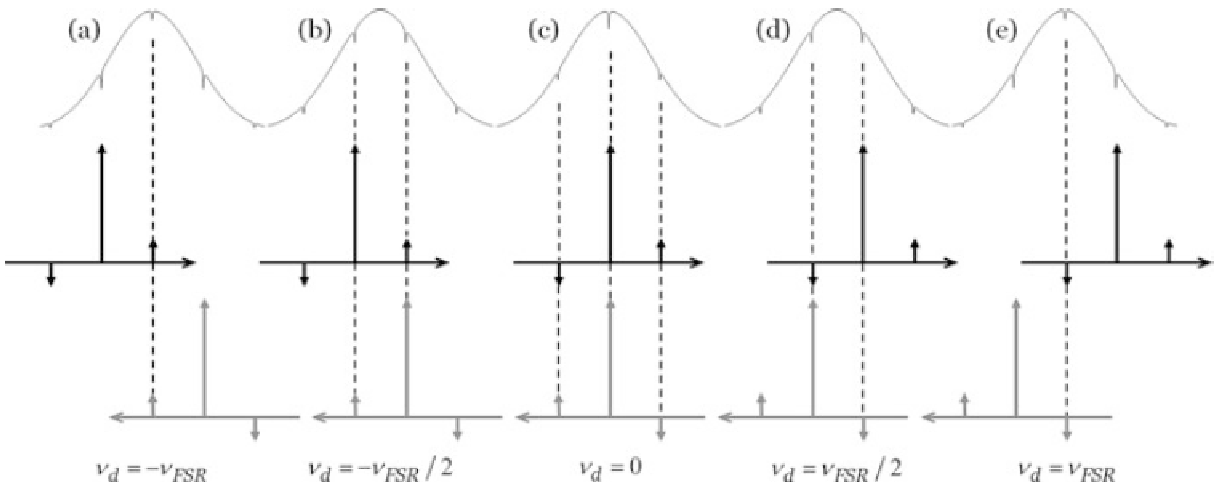

Figure 2.14: Burned velocity distribution in NICE-OHMS. We see that there are several velocity classes that benefits from the absorption from both sides giving rise to Lamd-dips. Image from [28].

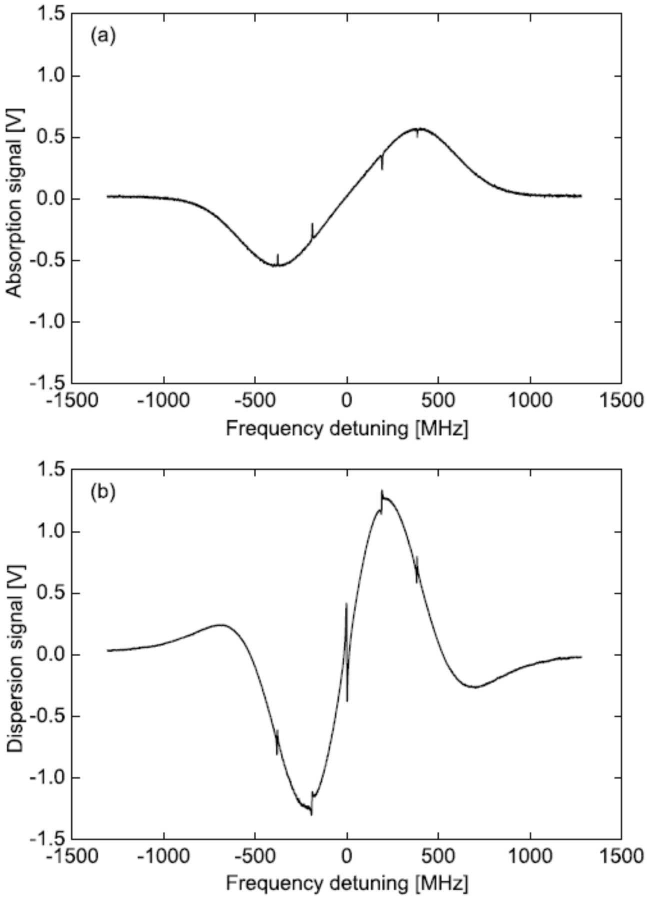

Figure 2.15: Typical lineshape of sub-Doppler signals in NICE-OHMS. We can distinguish the Lambd-dips on top of the Doppler broadened signal. Image from [28].

In the NICE-OHMS method the noise-immune aspect is coupled to the cavity-enhanced aspect. This means that the carrier wave and the two sidebands must travels inside the cavity. In other words the carrier and the sidebands must belong to the cavity spectrum. Hence the frequency modulation is usually equal to the FSR of the cavity and of course the carrier frequency must be a mode of the cavity. This is represented in fig. 2.13.

Eventually, the presence of counter propagating electromagnetic wave inside the cavity allows for Doppler free spectroscopy or sub-Doppler spectroscopy. As there are three frequencies propagating in the cavity instead of one there are nine possibility of combinations between one specific propagating frequency and another one counter propagating frequency. These combinations are illustrated in fig.2.14 and generate several "hole" in the velocity distribution of the gas sample. The resulting burned velocity distribution generates the dispersive signal and absorption signal shown in fig. 2.15.

2.2.2 The CW-CRDS method

Cavity RingDown Spectroscopy (CRDS) measures the intensity leaking from the cavity as a function of time. The following description of the method comes from [29]. The photons have a certain probability to escape the cavity each time it bounces on a mirror of the cavity. The higher the intensity the higher the number of photons leaving the cavity at the same time. The intensity leaving the cavity and reaching the detector is thus proportional to the intensity inside the cavity. As part of the intensity is lost continuously and proportionally to the intensity inside the cavity, when the laser source is switched off the measured signal is a decreasing exponential of the intensity versus time. This is depicted in fig. 2.16.

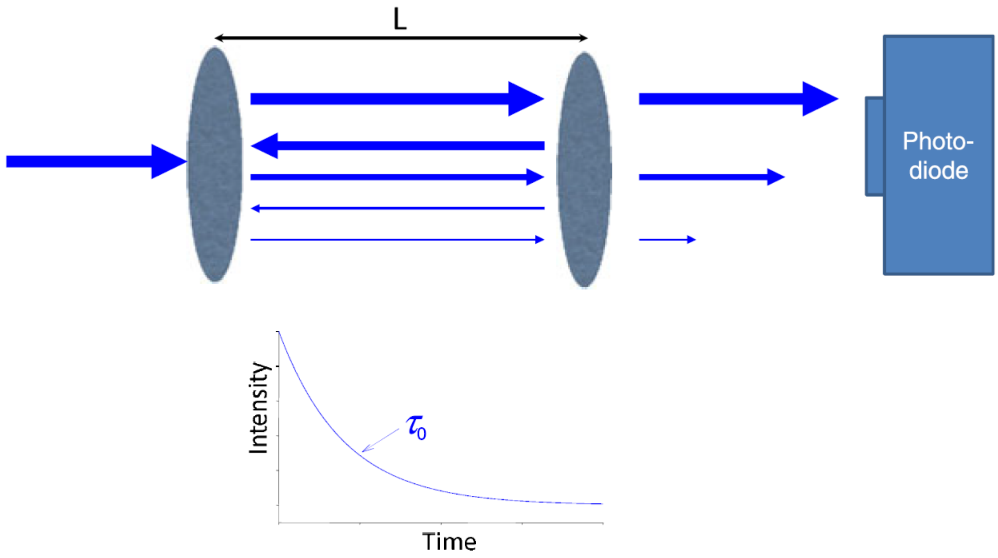

Figure 2.16: Schematic representation of a cavity ringdown spectroscopy experiment and the typical measured signal. Image from [29].

As always for measuring exponential decay a characteristic time scale is defined. Thus one calls τ_0 the ringdown time that corresponds to a decay of the measured signal from 1 to $1/e$. This ringdown time is given by:

$$\tau_0 = \frac{L/c}{(1-R)} \tag{2.98}$$

where L is the length of the cavity, c the speed of light and R the reflectivity of the mirror. When a sample is introduced inside the cavity it affects the ringdown time. Some part of the intensity inside the cavity is absorbed by the sample and thus the decrease in intensity measured at the detector is faster. When the sample is not saturated such that the absorption depends linearly on the intensity, the decay is still exponential. The ringdown time in this case is given by:

$$\tau = \frac{L/c}{1 - R + N\sigma(f)l} \tag{2.99}$$

where N is the number density of the sample, $\sigma(f)$ the absorption cross section as a function of the frequency and l is the path length of the absorber. The quantity $N\sigma(f)$l is the absorbance at the frequency f. With equations (2.98) and (2.99) one obtains:

$$A = \frac{L}{c\tau} - \frac{L}{c\tau_0} \tag{2.100}$$

There are two ways of performing a CRDS, either the source signal is pulsed either the source signal is a continous wave (CW-CRDS). The CW-CRDS is more sensitive than pulsed CRDS because the continous wave source as a narrower linewidth than a pulse and CW also allow to control more precisely the mode matching and the steady state reached in the cavity before shutting down the source and measuring the ringdown signal. This makes possible to perform sub-Doppler spectroscopy in addition to the Doppler broadened signal and thus the observation of a Lamb-dip.

2.3 The past and current research on the HD spectroscopy

2.3.1 Historical and current motivation

The H_2 molecule has no dipole transition due to the absence of electric dipole. This is due to its symmetry. On the countrary the HD molecule was expected to present a (small) dipole transition due to the presence of an extra neutron in the deuterium nucleous making the molecule slightly asymmetric. This dipole transition was observed in 1950 by Herzberg [30]. Then transition frequencies in the $(2-0)$ band were observed experimentally with increasing precision. However these experiments were still Doppler limited [4].

Recently, in 2018, the HD R(1) $(2-0)$ transition has been observed with the NICE OHMS method (Amsterdam's research group [12]) and the CRDS method (Heifei's research group [11]) allowing for Doppler free spectroscopy. This has lead to the observation of the asymmetry of the spectrum where a symmetrical Lamb-dip would have been expected as mentioned in the introduction. Also mentioned in the introduction was the interest of the HD precision experiment to confront theory with extreme accuracy allowing for the search of new physics. Now we will discuss in a bit more details what has been done regarding recent spectroscopy experiments and then present the attempts that came with those experiments to explain this asymmetry.

2.3.2 The asymmetric spectrum

The hyperfine structure and crossover resonances - Amsterdam

The first appearance of the asymmetric lineshape was shown in the introduction. Further investigation by the research team from Amsterdam lead to better resolution of this asymmetric profile. In 2019, the research team from Amsterdam obtained the absorption profile shown in fig. 2.17. Again we can observe that the asymmetry of the lineshape is greater when the pressure is higher [4].

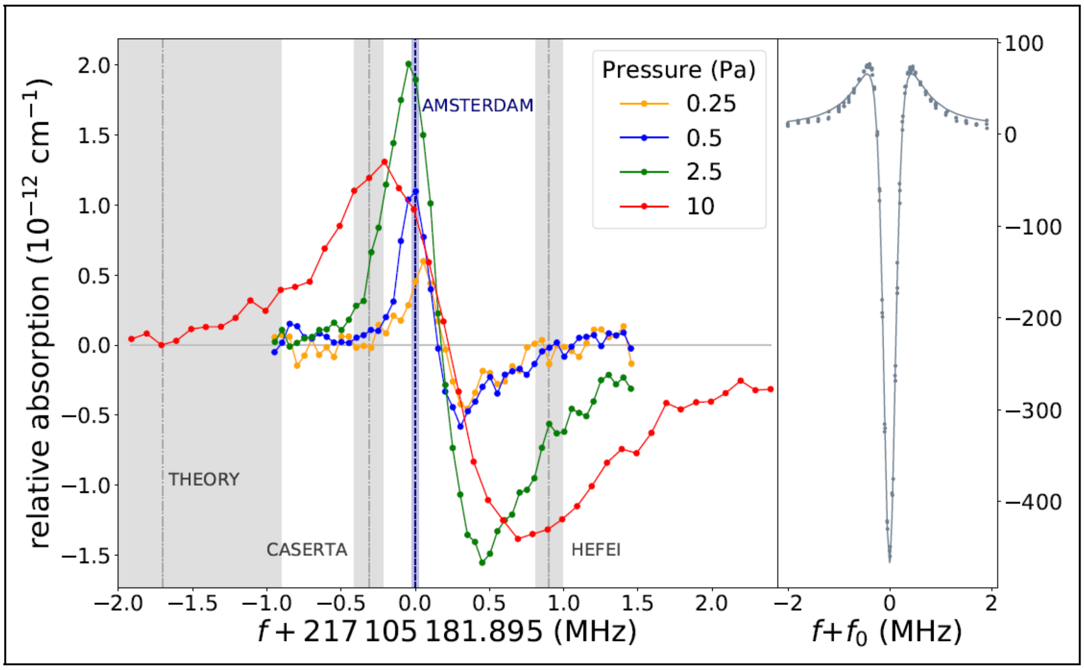

Figure 2.17: Right: Absorption spectrum of the HD R(1) (2 − 0) transition at several different pressures. Left: Typical NICE-OHMS signal obtained with acetylene. Image from [4].

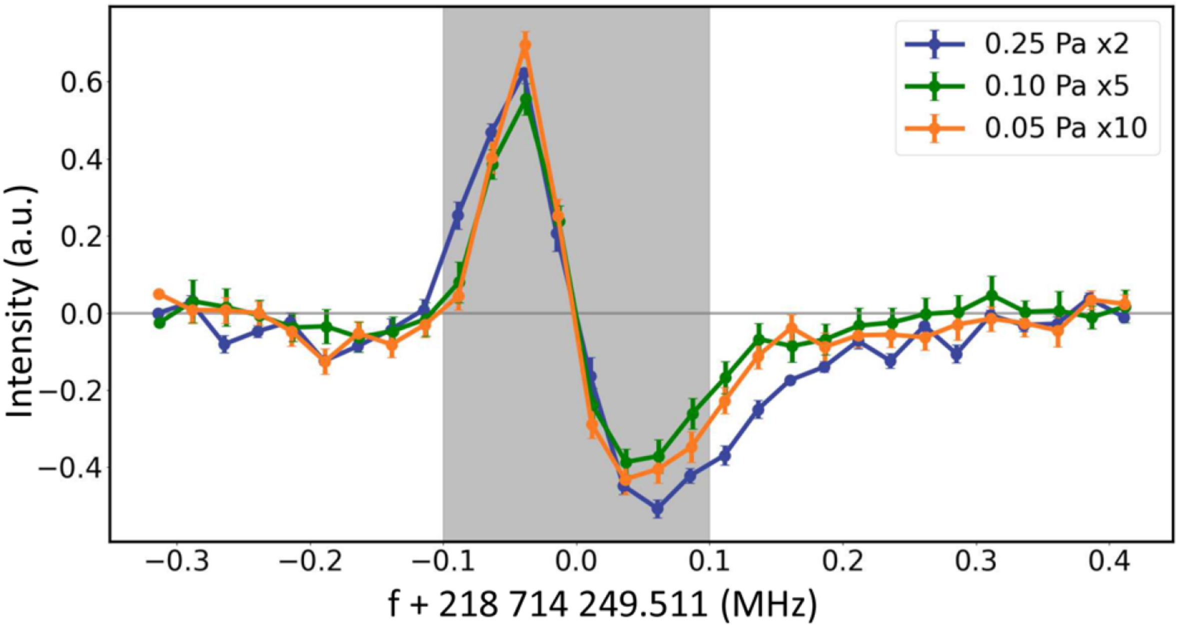

Figure 2.18: Absorption spectrum of the $R(14e)$ (4 0 0 15) ← (0 0 0 01) transition line of the $^{12}C^{16}O_2$ molecule. The spectrum is obtained with the same NICE-OHMS technique as for the HD. We can observe an asymmetric absorption lineshape despite the absence of hyperfine structure in the case of $^{12}C^{16}O_2$. Image from [31].

At that time the research group of Amsterdam attributed this asymmetric behavior to crossover resonances due to the hyperfine structure of the HD spectrum. They thus developed a model of these cross resonances using the optical Bloch equations including different hyperfine components. However, in 2022, they conducted experiments on the $R(0)$, $R(2)$ and $P(2)$ rovibrational transitions in the $(2-0)$ overtone band of HD and observed similar asymmetric absorption lineshape [31]. The same model was thus applied to these transition and unfortunately it does not reproduce the asymmetric lineshape of the $R(0)$ transition which present the simplest hyperfine signature since it start from $J = 0$. Moreover an asymmetric lineshape was experimentally observed by the Amsterdam group for a transition of the $^{12}C^{16}O_2$. However this molecule has no hyperfine structure. They thus discarded the possibility that the hyperfine structure is the cause of the asymmetry.

Fano-like resonances - Heifei

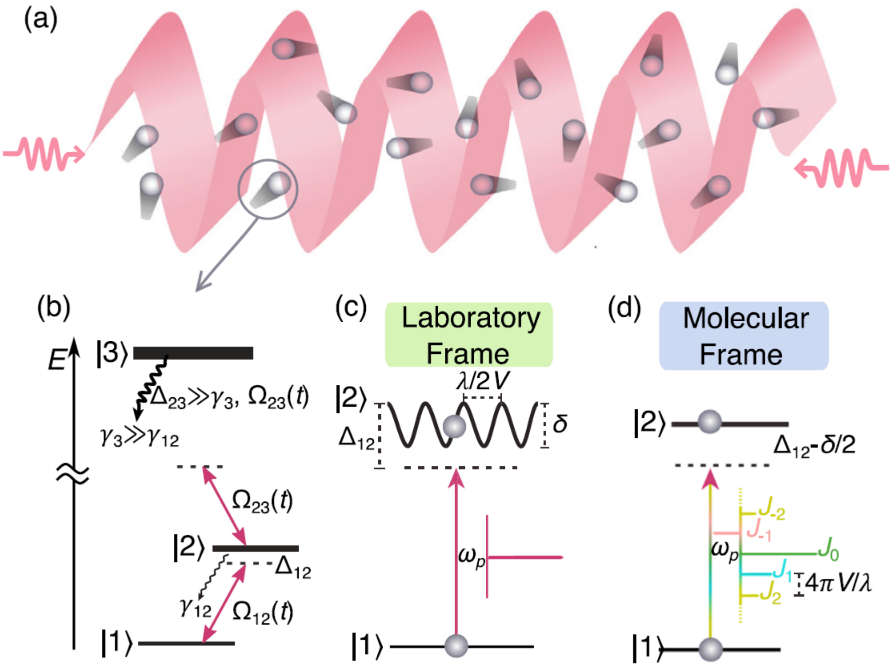

Figure 2.19: Schematic representation of the physics behind the Fano-like resonance mechanism. Panel a): Stationary wave with particles moving inside the wave. Panel b): Diagram of the energy levels of an individual particle and the corresponding coupling. Panel c): Effect of the third level on the second level in the laboratory frame. The modulation of the wave due to motion is perceived as an oscillation of the energy level. Panel d): Effect of the third level on the second level in the particle moving frame. The modulation of the wave due to motion is perceived as sidebands. Image from [32].

The Heifei research group has proposed another mechanism that could explain the asymmetric lineshape [32]. This mechanism is based on what they call nonlinear Fano-like resonance. The transition we want to probe is a weak transition due to the small value of the dipole moment. Therefore the coupling to the electromagnetic field is weak and requires very high laser intensity to compensate that. Let's call the states of this transition $|\psi_1\rangle$ and $|\psi_2\rangle$. Due to the high intensity of the laser beam the coupling to an off resonance transition that is not weak might be non negligible. Let's consider such a transition exist between the state $|\psi_2\rangle$ and another energy level with state $|\psi_3\rangle$. Because the particle of the gas that is probed is moving in a standing wave inside the cavity it sees an oscillation through space of the amplitude of the time oscillation of the electric field. This induces a AC Stark effect and the energy level of the state $|\psi_2\rangle$ oscillates as the particle moves inside the standing wave. This amplitude modulation can be reformulated as the presence of sidebands and the asymmetry emerges from a π phase difference between the sidebands that create the Fano-like interference. The Fano-like mechanism was tested numerically and experimentally verified on CO_2 rovibrational spectroscopy.

Chapter 3

Toy model for numerical computation of the absorption coefficient of a 2-level quantum system

3.1 Numerical setup

Let's consider the useful parameters for absorption spectroscopy of the HD molecule, we have

$f_{R(1)\ (2-0)} = 217\ 105\ 181\ 895(20)$ kHz	Source [4]
$D_{R(1)\ (2-0)} = 0.20(2)\ 10^{-4}$ D	Source [33]
$\Gamma_{\text{spont. em.}} \approx 1$ Hz	Source [4]

where appear in order the transition frequency, the dipole moment associated to this transition and finally the spontaneous emission rate of the upper energy level of the transition. Moreover the asymmetric profile extends over roughly ±1 MHz around the transition frequency as can be seen on the experimental observation shown in the previous chapter (see fig. 1.2, fig. 1.3 and fig. 2.17). So we would like to numerically investigate the absorption for detuning values that go to around 1 MHz: $\delta \approx 1$ MHz. As mentioned in the previous chapter if the electric field perturbation associated to the laser beam is given by $\vec{E} = \vec{E}_0 \cos(\omega t + \phi)$ then the polarization is given by

$$P = \epsilon_0 \left[\chi' \vec{E}_0 \cos(\omega t + \phi) + \chi'' \vec{E}_0 \sin(\omega t + \phi) \right]$$

In the case of HD this means that the polarization will oscillates extremely rapidly (compared to the lifetime of the upper energy level) because the frequency of the laser $\omega_{R(1)\ (2-0)} \pm \delta$ will be 10^{14} order of magnitude higher than the frequency associated to the lifetime. This makes it numerically extremely demanding to sample the time with sufficient precision such that the frequency of the polarization is correctly captured by the numerical time sampling over a time window on the order of several times the lifetime such that steady state is reached. We will thus put that issue aside for the moment and use a toy model with arbitrary value that permit an easy analysis of the interactions between different phenomenons. Moreover if a satisfying mechanism that explains the asymmetry is found it would be nice to use it on other quantum systems to make predictions. So let's not worry for now about the numerical issue to implement specific value of a specific species.

Although the model we will analyse first is a toy model the numerical analysis was made using atomic units from the beginning. As a remainder the definition of the atomic units is

$$\hbar = e = m_e = 4\pi\epsilon_0 = 1 \tag{3.1}$$

with $\hbar$ the reduced Planck constant, e the elementary electric charge, m_e the mass of the electron and ϵ_0 the void dielectric permittivity. This implies that

$$c \approx 137.0360013696001 \tag{3.2}$$

$$h = 2\pi \tag{3.3}$$

where c and h are obviously the speed of light and the Planck constant. In the numerical simulations associated to the toy model the value used for the speed of light was rounded thus $c = 137$. In the atomic unit system the following units are defined: energy unit (Hartree) $\mathrm{E_H}$, length unit (Bohr radius) $\mathrm{a_0}$.

The toy model will have the following parameters chosen close to unity to avoid large number in the simulations as much as possible as the goal is at first to test the numerical method to compute the absorption profile rather than focusing on the order of magnitude of a real physical problem:

$$f_0 = 5\ \mathrm{E_H}/\hbar \tag{3.4}$$

$$D_{12} = 1\ e\mathrm{a_0} \tag{3.5}$$

where f_0 is the transition frequency and D_{12} is the dipole moment of the transition. For comparison, HD has $f_0 \simeq 5.25\ 10^{-3}\ \mathrm{E_H}/\hbar$ and $D_{12} \simeq 7.87N\ 10^{-6}\ e\mathrm{a_0}$ (see chapter 5). We ignore the details of a Gaussian beam. Hence we suppose that the electromagnetic wave going through the particle is a plane wave polarized such that the electric field is along the x axis. Thus $E(t) = E_{0x}\cos(\omega t + \phi)$. The lifetime of our toy model will be given by the Einstein coefficient $\Gamma = A_{21}$. The latter is given by [18]

$$A_{21} = \frac{g_1}{g_2}\frac{4\alpha}{3c^2}\omega_0\,|D_{12}|^2 \tag{3.6}$$

We do not consider degeneracy of the levels so $g_1/g_2 = 1$. Eventually the saturation intensity is given by [21]

$$I_{\mathrm{sat}} = \frac{\pi}{3}\frac{hc}{\lambda_0^3\tau} \tag{3.7}$$

where λ_0 is the wavelength (in vacuum) corresponding to the transition frequency and $\tau = \Gamma^{-1}$ is the liftetime of the upper energy level.

The numerical simulation were performed using python code. The Lindblad master equation was solved using the library QuTiP [34].

3.2 Time evolution of the density matrix and computation of the absorption coefficient

3.2.1 Time evolution without decoherent processes

The first objective was to obtain a numerical solution of the Rabi oscillations that fit the analytical solution. The general problem is

$$\begin{aligned}
\dot{\hat{\rho}}(t) &= -\frac{i}{\hbar}\left[\hat{H}(t), \hat{\rho}(t)\right] \\
\hat{H}(t) &= \frac{1}{2}\begin{pmatrix} 0 & \Omega_R\exp(i(\delta t + \phi)) \\ \Omega_R\exp(-i(\delta t + \phi)) & 0 \end{pmatrix} \\
\hat{\rho}(0) &= \begin{pmatrix} \rho_{11}(0) & \rho_{12}(0) \\ \rho_{21}(0) & \rho_{22}(0) \end{pmatrix}
\end{aligned}$$

The chosen initial condition is that the quantum system is in its lower state with a probability of 1. The laser has an offset in frequency with respect to the transition which is equal to $0.01f_0$. Thus $f = 1.01\ f_0$ and $\delta = \omega - \omega_0 = 0.01\ \omega_0$. The initial phase is set to $\phi = 0$. The problem becomes

$$\begin{aligned}\dot{\hat{\rho}}(t) &= -\frac{i}{\hbar}\left[\hat{H}(t), \hat{\rho}(t)\right]\\ \hat{H}(t) &= \frac{1}{2}\begin{pmatrix} 0 & \Omega_R \exp(i0,01\omega_0 t) \\ \Omega_R \exp(-i0,01\omega_0 t) & 0 \end{pmatrix}\\ \hat{\rho}(0) &= \begin{pmatrix} 1 & 0 \\ 0 & 0 \end{pmatrix}\end{aligned}$$

With a time step in the solver that is $1/50\ T_{\Omega/2}$ where $T_{\Omega/2} = 2\pi/(\Omega/2)$ is the period of the Rabi oscillation then the numerical solution fits the analytical solution and the oscillations are smooth and well resolved. This is shown for the populations of the density matrix operator in fig. 3.1 for a simulation from $t = 0$ to $t = 10\ T_{\Omega/2}$. The analytical solution was obtained in the last chapter and it gives in this case

$$|c_2(t)|^2 = \rho_{22} \approx 0.237 \sin^2(0.180t) \tag{3.8}$$

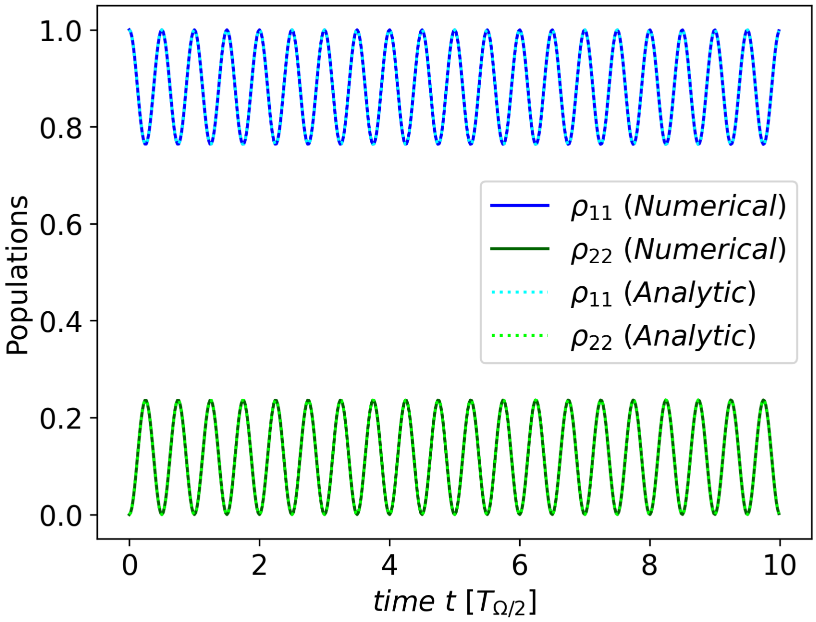

Figure 3.1: Time evolution of the populations of a 2-level quantum system perturbed by an off resonance monochromatic electric wave $E = E_0 \cos(\omega t)$ and without spontaneous emission. The detuning of the laser is $\delta = 10^{-2} f_0$.

3.2.2 Time evolution with decoherent processes

Now we include the spontaneous emission process. The parameter are the same except that now $\Gamma = A_{21} \approx 0.016\ \mathrm{E_H}/\hbar$ (Instead of $\Gamma = 0$). The Hamiltonian of the problem and the initial condition remain the same. However the equation becomes

$$\begin{aligned}\dot{\hat{\rho}}(t) &= -\frac{i}{\hbar}\left[\hat{H}(t), \hat{\rho}(t)\right] + \frac{1}{2}\left[2\hat{C}\hat{\rho}\hat{C}^\dagger - \hat{\rho}\hat{C}^\dagger\hat{C} - \hat{C}^\dagger\hat{C}\hat{\rho}\right]\\ \hat{C} &= \sqrt{\Gamma}|\psi_1\rangle\langle\psi_2|\end{aligned}$$

Again we want to compare to the analytical solution. This time we don't have an analytical solution for this exact problem but we saw in the last chapter that the Bloch equations allow to compute a steady state solution. The comparison with this solution is shown in fig. 3.2. We observe that the Rabi oscillations are damped and reach a steady state solutions after several times the characteristic time of the exponential period which is here $1/\Gamma$. Again the numerical solution agrees with the theoretical one.

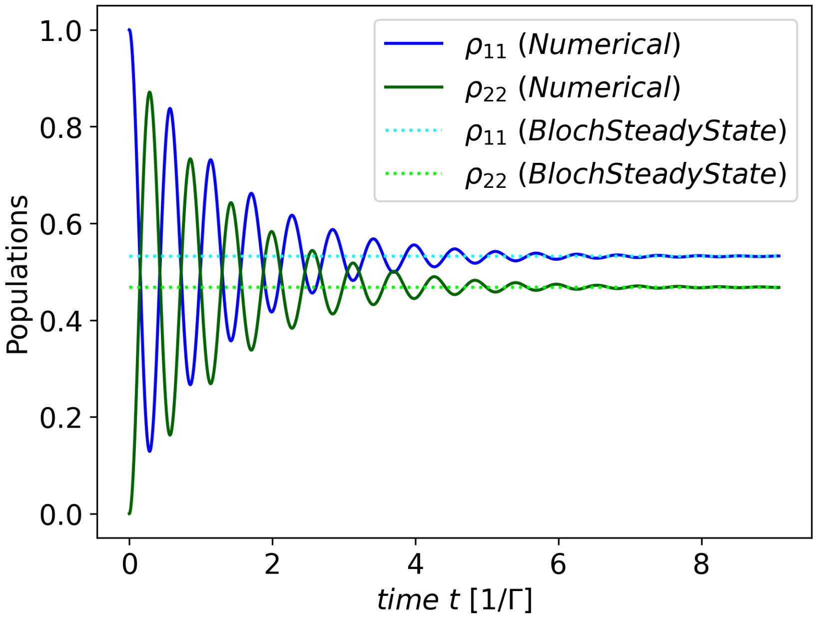

Figure 3.2: Time evolution of the populations of a 2-level quantum system perturbed by an off resonance monochromatic electric wave $E = E_{0x} \cos(\omega t)$ and with spontaneous emission. The detuning of the laser is $\delta = 10^{-3} f_0$.

3.2.3 Computation of the absorption coefficient

We saw that the absorption coefficient is linearly linked to the χ'' coefficient that appears in the polarization of the quantum system. Hence the polarization must be properly computed numerically. Unfortunately the time step chosen so far is too big because the polarization oscillates at the same frequency as the incident electric wave and consequently much faster than the Rabi oscillations. Now the time step is $1/10000\ T_{\Omega/2}$ in order to obtain a smooth curve.

The full time evolution of the polarization is represented in fig. 3.3. We can observe as for the populations a transient regime until the steady state solution is reached. Because the polarization oscillates very quickly the oscillations can not be seen on this graph. A zoom on the last 5 periods of the oscillations of the polarization is shown in fig. 3.4. On top of the numerical solution is plotted the analytical solution. We see that the two graphs match perfectly and the numerical solution is thus valid so that it can be used to extract the value of the χ'' coefficient.

To evaluate the coefficient χ'' we could perform a fast Fourier transform. However as we already know the frequency present in the signal and as this frequency is unique we can easily extract the $\sin(\omega t)$ component. The computation works as follow:

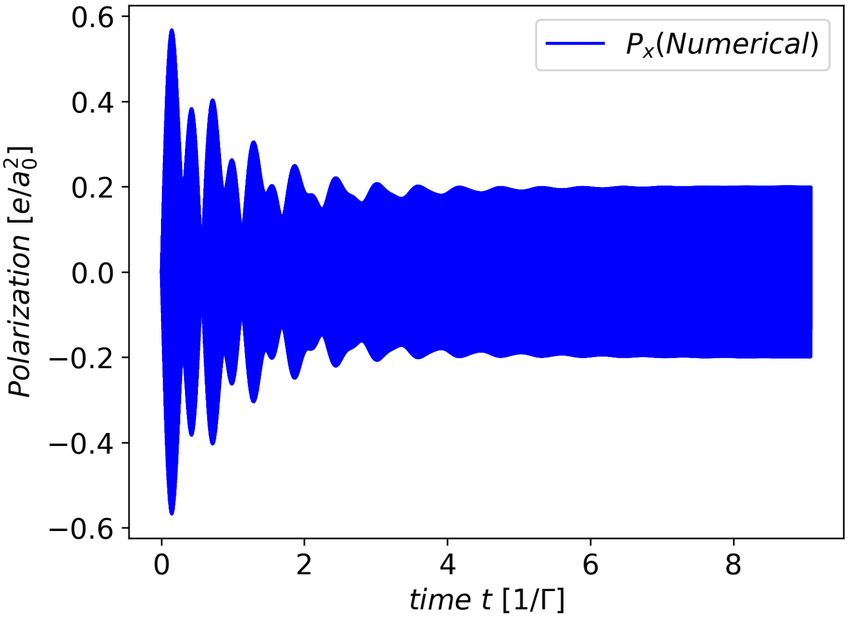

Figure 3.3: Time evolution of the polarization of the quantum system over the whole simulation. The signal is composed of a transient regime and a steady state regime.

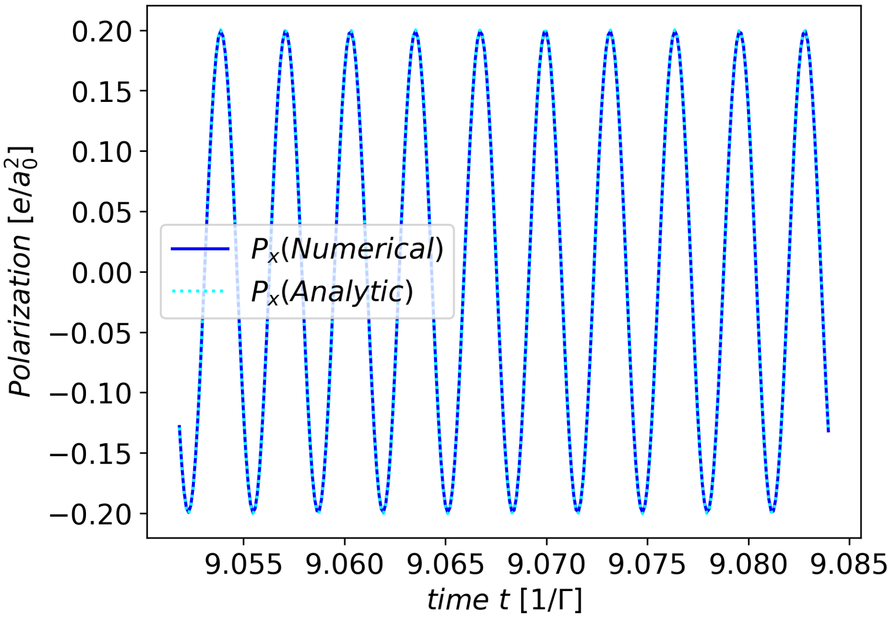

Figure 3.4: Last 10 periods of oscillations of the numerical evaluation of the polarization of the quantum system. The numerical solution fits perfectly the analytical solution.

$$
\begin{aligned}
\int_{t_f-n\frac{T}{2}}^{t_f} P_x(t)\ \sin(\omega t+\phi)\ dt &= \int_{t_f-n\frac{T}{2}}^{t_f} \epsilon_0[\chi' E_{0x}\cos(\omega t+\phi)\sin(\omega t+\phi)+\chi'' E_{0x}\sin^2(\omega t+\phi)]\ dt \\
&= \int_{t_f-n\frac{T}{2}}^{t_f} \epsilon_0[\chi' E_{0x}\frac{\sin(2\omega t+2\phi)}{2}+\chi'' E_{0x}\frac{1-\cos(2\omega t+2\phi)}{2}]\ dt \\
&= \int_{t_f-n\frac{T}{2}}^{t_f} \epsilon_0\frac{E_{0x}}{2}[\chi'\sin(2\omega t+2\phi)+\chi''-\chi''\cos(2\omega t+2\phi)]\ dt \\
&= \int_{t_f-n\frac{T}{2}}^{t_f} \epsilon_0\frac{E_{0x}}{2}\chi''\ dt \\
&= \frac{1}{2}\epsilon_0 E_{0x}\chi''[t_f-(t_f-n\frac{T}{2})] \\
&= n\epsilon_0 E_{0x}\frac{T}{4}\chi''
\end{aligned}
$$

Where t_f is the end value of the time sample in the simulation, n is a positive integer and $T = 2\pi/\omega$. The cos and sin disappear between lines 3 and 4 because the integration is performed over n-times the period of these functions. The integration window is at the end of the time sample such that the solution is the closest from a steady state solution. The integration was performed numerically using the Simpson integration scheme.

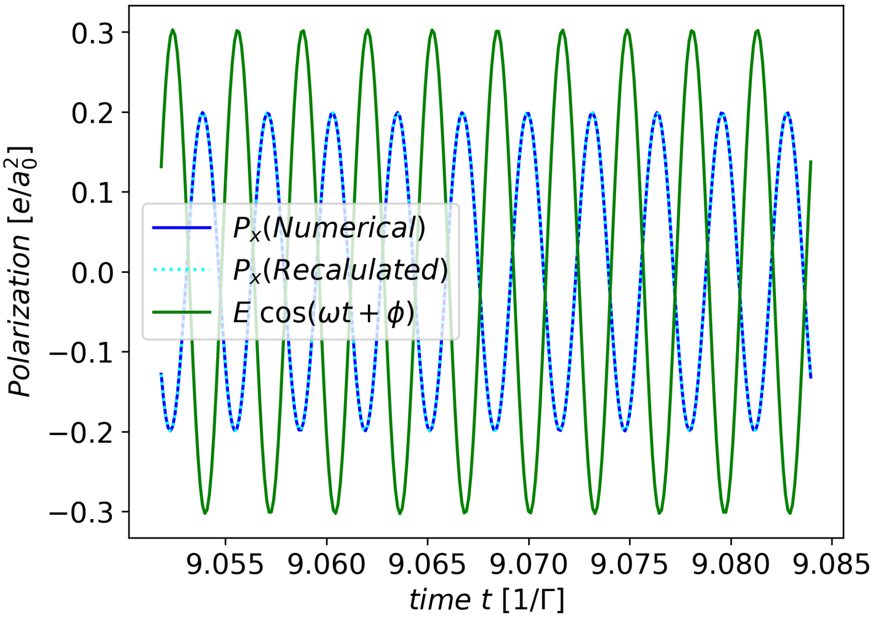

Figure 3.5: Last 10 periods of oscillations of the numerical evaluation of the polarization of the quantum system. The coefficient χ' and χ'' computed from the numerical solution are used into the analytical form of the polarization (eq. 2.83) to reconstruct the signal. The perfect fit ensures that the computation of these coefficients is correct and sufficiently accurate.

Hence, we can find the imaginary part of the dielectric susceptibility coefficient χ'':

$$
\chi'' = 4\frac{\int_{t_f-n\frac{T}{2}}^{t_f} P_x(t)\ \sin(\omega t+\phi)\ dt}{n\epsilon_0 E_{0x} T} \tag{3.9}
$$

Similarly, we have:

$$\chi' = 4\frac{\int_{t_f-n\frac{T}{2}}^{t_f} P_x(t)\ \cos(\omega t+\phi)\ dt}{n\epsilon_0 E_{0x} T} \tag{3.10}$$

We can check a posteriori that the coefficients are accurately computed by recalculating the polarization signal from its analytical form. This is shown in fig. 3.5 where we can observe that the recalculated signal fits perfectly the numerical signal. The coefficient obtained are thus correctly extracted. These are $\chi' = -8.014924412749526$ and $\chi'' = 2.0522401785301403$ and correspond to the values obtained with the analytical formula given by eq. 2.84: $\chi' = -8.053956727179143$ and $\chi'' = 2.0608960019817175$.

In fig. 3.5 is also shown the incident electric wave and we see that the polarization signal is primarily composed of a sine component which is consistent with the frequency of the wave being closed to the transition frequency that maximizes absorption.

3.3 Natural, Doppler broadened and saturated lineshapes

3.3.1 The Lorentzian lineshape

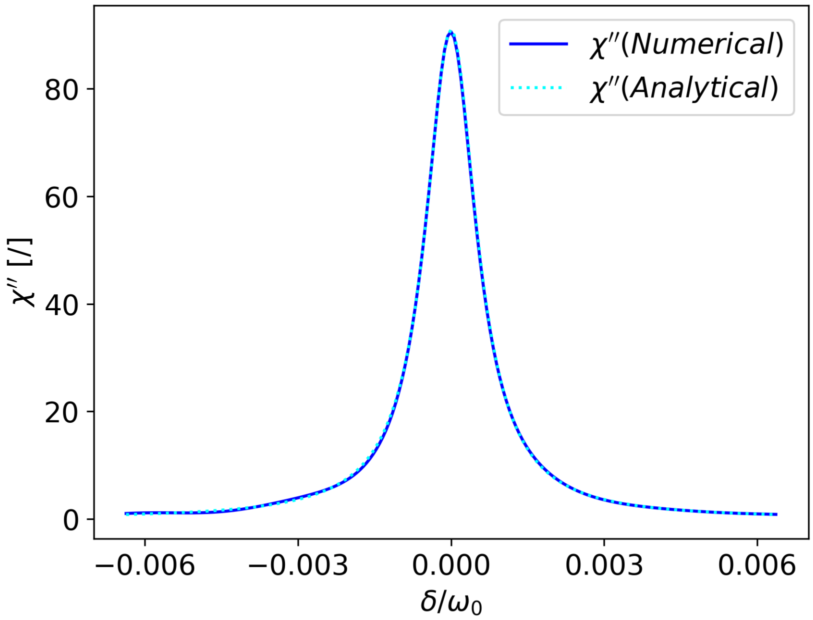

Figure 3.6: Lorentzian profile of the imaginary part of the dielectric susceptibility χ'' of a two level quantum system perturbed by an electric wave with a frequency close to its transition frequency.

In the previous section we saw how to extract the χ'' coefficient from the simulation of a 2-level quantum system perturbed by a electric wave. From there it suffices to run the same code over a frequency window centred on the transition frequency to obtain the χ'' coefficient as a function of the frequency of the wave. The χ'' coefficient is proportional to the absorption coefficient as mentioned in the previous chapter and the lineshape of the $\chi''(\omega)$ curve must be a Lorentzian as for the absorption coefficient. The curve obtained through numerical computation is shown in fig. 3.6. On top is plotted the analytic curve and we see that they match.

Also, the intensity of the electric wave is reduced in this simulation compared to the previous ones ($I = 0.5\ E_{\mathrm{H}}^2/(a_0^2\hbar) \rightarrow I = 0.01\ E_{\mathrm{H}}^2/(a_0^2\hbar)$) and the duration of the simulation has been increased ($t_f = 10\ 1/\Gamma \rightarrow t_f = 50\ 1/\Gamma$). The reason is that the value computed numerically would be oscillating around the exact (analytic) value due to the still non-steady state behavior of the numerical solution after 10 $1/\Gamma$. The procedure to compute χ'' is thus correct but the value used for representing the Rabi oscillations accurately on a time scale comparable to the amortisation time scale lead to very long computation time to ensure convergence of the solution. The reduction of the intensity reduces the Rabi oscillations and the longer time simulation allow the solution to come closer to steady state.

3.3.2 The Doppler broadened lineshape and saturation

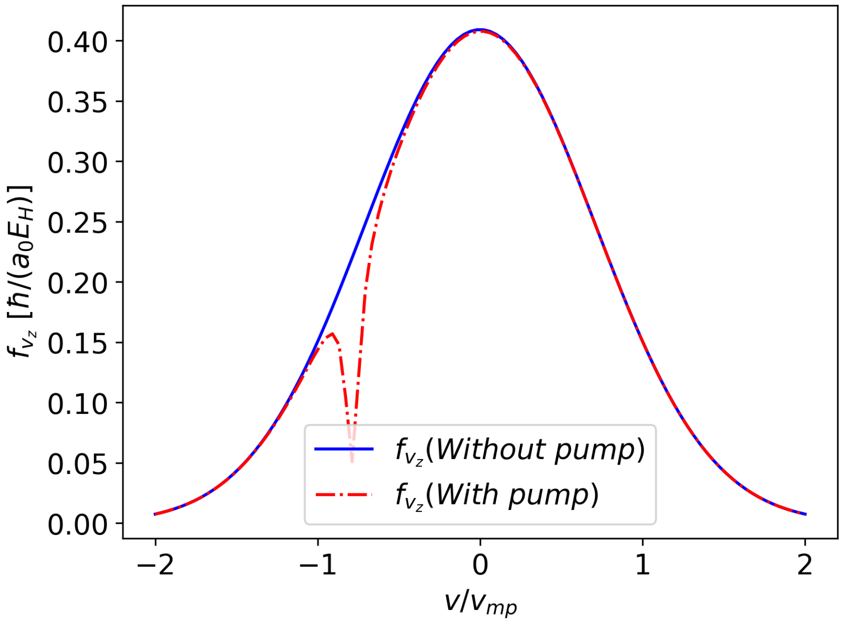

Figure 3.7: Velocity distribution of a gas made of the same 2-level quantum system submitted to a high intensity pump laser with a frequency slightly offset from the quantum system transition frequency.

As explained in the previous chapter the absorption spectrum in a gas is broadened due to the Doppler effect. As a result the absorption lineshape is a convolution of the natural absorption spectrum and the 1D velocity distribution inside the gas (velocity component along the beam axis). The 1D velocity distribution follows the Maxwell-Boltzmann distribution, noted f_{v_z} and is easily implemented:

$$f_{v_z} = \sqrt{\frac{m}{2\pi k_{\mathrm{B}}T}} \exp\left(-\frac{mv_z^2}{2k_{\mathrm{B}}T}\right) \tag{3.11}$$

As the model is a toy model the value of the parameter have no physical relevance. The real value of the Boltzmann constant k_{B} (in atomic unit for consistency) is used and the temperature is set to 300 K. The mass used in the simulations is $m = 0.001\ m_e$ in atomic unit. This mass is ridiculously small and the sole purpose of this value is to obtain a Doppler broadening visible with the non-physical parameter of the toy model quantum system. The corresponding velocity distribution is shown in fig. 3.7.

The previous section showed that the present numerical computation performs well at evaluating the natural absorption spectrum. Only the convolution of the Lorentzian profile with the velocity distribution is left to do. The convolution algorithm is already implemented in the python library SciPy [35]. Using this implementation the absorption spectrum shown in fig. 3.8 in blue is obtained.

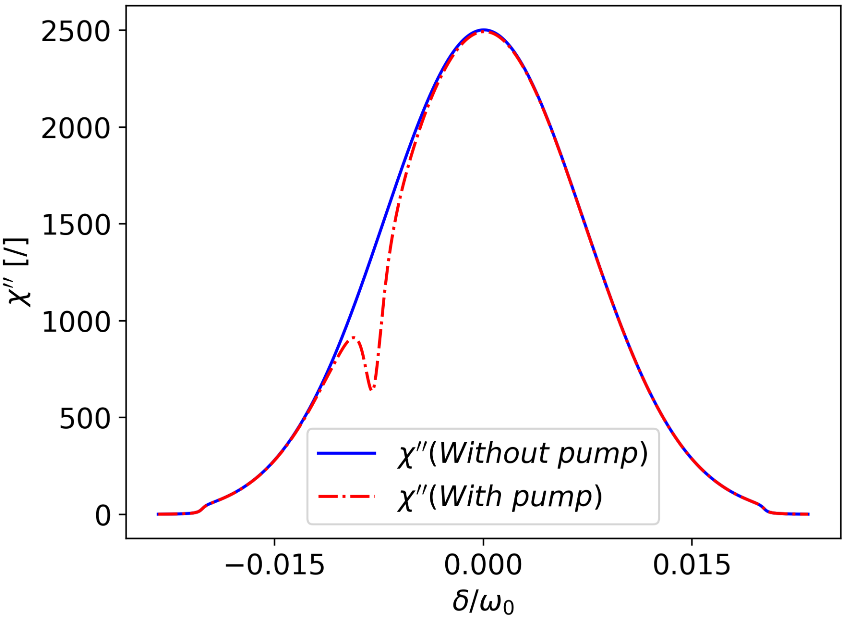

Figure 3.8: Saturated and non saturated Doppler broadened profile of the imaginary part of the dielectric susceptibility of a gas made of the same 2-level quantum system perturbed by an electric wave with a frequency close to its transition frequency.

Now we would like to implement saturation spectroscopy. This is done experimentally with a pump laser and a probe laser. The pump laser “burns a hole” in the velocity distribution. The numerical computation must thus take into account the effect of the pump laser on the velocity distribution before computing the convolution. The absorption of photons from the pump by the medium translates into an important occupation of the upper energy level of the 2-level system and a depopulation of the lower energy level. But we can already access the occupation of both levels as it is given by the diagonal elements of the density matrix. Hence, the evolution of the density matrix is computed with the electric field given by the intensity of the pump laser until steady state is reached for all velocity classes evaluated by the Maxwell-Boltzmann distribution. With the density matrix obtained the difference $\rho_{11} - \rho_{22}$ is evaluated. Why $\rho_{11} - \rho_{22}$ and not ρ_{11} ? Because the absorption is due to the population in the lower energy level and on top of that the population in the upper energy level cancels some absorption due to stimulated emission. The difference $\rho_{11} - \rho_{22}$ thus gives an effective number of particles that contributes to the net absorption. The “burned” velocity distribution, noted $f_{v_z,\text{burned}}$, is thus given by $f_{v_z,\text{burned}} = (\rho_{11} - \rho_{22})f_{v_z}$. With a pump laser and a probe laser having respectively 10 times and 0.1 times the saturation intensity of the transition we obtain the “burned” velocity distribution represented in fig. 3.7 and the saturated absorption lineshape represented in fig. 3.8. Note that the transition frequency is 5 $\mathrm{E_H}/\hbar$ and the pump laser has a fixed frequency of 5.04 $\mathrm{E_H}/\hbar$.

Discussion on the pump/probe approach

Now that we have obtained a Lamp-dip the final step would be to allow the pump frequency to vary with the probe frequency such that the Lamb-dip is centred on the transition frequency of the system. Then we would have obtained the symmetric Lamb-dip lineshape of Doppler free spectroscopy and carry on to apply it to the HD molecule. However when the frequency of the pump varies, the implementation becomes a little more complicated as the convolution can not be use directly anymore. Indeed when the pump frequency was fixed the "burned velocity distribution" was fixed, i.e. the location of the hole in the velocity distribution was fixed. This velocity distribution with a hole at a fixed velocity class is $f_{v_z,\text{burned}}(\omega_{\text{pump}})$. When the pump frequency is not fixed, the velocity distribution changes because the location of the hole changes and the coefficient χ'' is not anymore given by

$$\chi''(\omega) = \int_{-\infty}^{+\infty} f_{v_z,\text{burned}}(\omega_{\text{pump}})\chi''_{\text{Lorentz}}(\omega - kv_z)\ dv_z$$

but by

$$\chi''(\omega) = \int_{-\infty}^{+\infty} f_{v_z,\text{burned}}(\omega)\chi''_{\text{Lorentz}}(\omega - kv_z)\ dv_z$$

The numerical implementation changes a only a bit. However taking the time to actually implement it might be worthless because it relies on the separation of the pump effect and the probe effect. The pump "act first" on the medium and produce a dip in the velocity distribution and then the probe "act last" and probe the pumped medium. However in the case of HD $R(1)$ $(2-0)$ spectroscopy the transition frequency is weak and thus requires a high intensity laser beam. This is acheive experimentally through cavity enhanced spectroscopy but this implies that there are no more pump or probe. The sample sees very intense beams coming from both directions along the cavity axis. As in an optical cavity the electromagnetic wave "bounces" between the mirrors, it may be that a decomposition such as "the N first reflections act first as a pump and then the remaining intensity probe the medium over the last reflections before leaving the cavity" has no physical sense and is artificial. The pump/probe approach is thus questionnable for the problem we aim at analysing. In this master thesis, this approach has thus been abandonned and another method to compute the absorption based on the populations rather than the coherences has been used. This alternative method is the topic of the next chapter and we will see it is more suited for our purpose.

Chapter 4

Toy Model : Absorption spectroscopy of a 2-level quantum system in a laser cavity

We now turn our attention to the analysis of a 2-level quantum system moving in an optical cavity with a high intensity standing wave trapped in the cavity. We ignore Gaussian modes and consider the simpler situation of plane waves. The standing wave inside the cavity can be described as follow

$$E(z,t) = E_0 \cos(kz + \phi_{space}) \cos(\omega t + \phi_{time}) \tag{4.1}$$

where ω and k are the frequency and the wavenumber respectively of the laser beam in the lab reference frame. ϕ_{space} and ϕ_{time} are arbitrary initial phases. Eventually E_0 is the amplitude of the electric field given by the intensity of the wave through $I = 1/2\epsilon_0 c E_0^2$.

The standing wave is equivalent to two counterpropagating waves. This is easily obtained with Simpson's trigonometry formula

$$\cos(x)\cos(y) = \frac{1}{2}\{\cos(x+y) + \cos(x-y)\} \tag{4.2}$$

which gives

$$E(z,t) = \frac{E_0}{2}\{\cos(kz + \phi_{space} + \omega t + \phi_{time}) + \cos(kz + \phi_{space} - \omega t - \phi_{time})\} \tag{4.3}$$

and because $\cos(z) = \cos(-z)$ we can highlight the opposite direction of propagation by rewritting the field as:

$$\begin{aligned} E(z,t) &= \frac{E_0}{2}\{\cos(\omega t + kz + \phi_{time} + \phi_{space}) + \cos(\omega t - kz + \phi_{time} - \phi_{space})\} && (4.4)\\ &= \frac{E_0}{2}\cos(\omega t + kz + \phi_1) + \frac{E_0}{2}\cos(\omega t - kz + \phi_2) && (4.5) \end{aligned}$$

where $\phi_1 = \phi_{time} + \phi_{space}$ and $\phi_2 = \phi_{time} - \phi_{space}$. We can see that the two propagating waves have each half the amplitude of the standing wave as expected.

Eventually, we can rewritte this field in the reference frame of the particle by substituting $z(t) = v_z t$. The electric field is then written as

$$\begin{aligned} E(t) &= \frac{E_0}{2}\cos(\omega t + kv_z t + \phi_1) + \frac{E_0}{2}\cos(\omega t - kv_z t + \phi_2) && (4.6)\\ &= \frac{E_0}{2}\cos((\omega + kv_z)t + \phi_1) + \frac{E_0}{2}\cos((\omega - kv_z)t + \phi_2) && (4.7) \end{aligned}$$

In conclusion, a particle moving in the cavity perceives two counterpropagating waves with equal amplitudes and opposite Doppler shifts.

4.1 Time evolution of the density matrix

In the basis $|\psi_1\rangle$, $|\psi_2\rangle$ of the eigenstates of the Hamiltonian, the Schrödinger equation is now

$$i\dot{c}_1 = \Omega_R \left(\cos((\omega + kv_z)t + \phi_1) + \cos((\omega - kv_z)t + \phi_2)\right) e^{-i\omega_0 t} c_2 \tag{4.8}$$

$$i\dot{c}_2 = \Omega_R^* \left(\cos((\omega + kv_z)t + \phi_1) + \cos((\omega - kv_z)t + \phi_2)\right) e^{i\omega_0 t} c_1 \tag{4.9}$$

Develloping the cosine with exponentials and neglecting the rapidly oscillating exponentials that contain $\omega + \omega_0$, we obtain:

$$i\dot{c}_1 = \frac{\Omega_R}{2} \left(e^{i(\omega-\omega_0+kv)t+\phi_1} + e^{i(\omega-\omega_0-kv)t+\phi_2}\right) c_2 \tag{4.10}$$

$$i\dot{c}_2 = \frac{\Omega_R^*}{2} \left(e^{-i(\omega-\omega_0+kv)t+\phi_1} + e^{-i(\omega-\omega_0-kv)t+\phi_2}\right) c_1 \tag{4.11}$$

We define now the detuning, $\delta_0 = \omega - \omega_0$ and the shifted detunings $\delta_{red} = \delta_0 - kv$ and $\delta_{blue} = \delta_0 + kv$ such that

$$i\dot{c}_1 = \frac{\Omega_R}{2} \left(e^{i\delta_{blue}t+\phi_1} + e^{i\delta_{red}t+\phi_2}\right) c_2 \tag{4.12}$$

$$i\dot{c}_2 = \frac{\Omega_R^*}{2} \left(e^{-i\delta_{blue}t+\phi_1} + e^{-i\delta_{red}t+\phi_2}\right) c_1 \tag{4.13}$$

Hence the Hamiltonian of the system is equal to

$$H = \frac{1}{2} \begin{pmatrix} 0 & \Omega_R \left(e^{i\delta_{blue}t+\phi_1} + e^{i\delta_{red}t+\phi_2}\right) \\ \Omega_R^* \left(e^{-i\delta_{blue}t+\phi_1} + e^{-i\delta_{red}t+\phi_2}\right) & 0 \end{pmatrix} \tag{4.14}$$

This Hamiltonian leads to a new behavior of the populations over time. This behavior depends on the relative values of the frequencies in the physics of the problem. These frequencies are the Rabi frequency Ω_R, the detuning δ, the spontaneous emission rate Γ and the frequency associated to the motion of the particle inside the standing wave $2kv_z$. The last one $2kv_z$ is linked to the spatial variation of the amplitude of the electric field $E(z,t) = E_0 \cos(kx + \phi_{space}) \cos(\omega t + \phi_{time})$. A particle moving inside the cavity will thus alternate between the maximum value of the amplitude of the time oscillations and the nodes of the standing wave. When the particle is going through a maximum of the electric field oscillations it will converge towards the same response as for a stationnary particle in an oscillating electric field. This convergence towards the same value as the stationnary particle solution is shown on each of the three figures below. The time evolution of the moving particle corresponds to the curves with a light blue color and a light green color whereas the time evolution of the particle at rest (at a maximum of the standing wave) correspond to the curves with a deep blue color and deep green color. When the particle is on a node of the standing wave it will converge towards a unperturbed solution, i.e. the lower energy state is fully populated due to spontaneous emission and the absence of excitation. The travelling partcle will thus alternate between these two behaviors periodically.

Depending on the value of Ω_R, δ and Γ relatively to kv_z the periodic behavior will be different. If the values of Ω_R, δ and Γ allow for the particle to reach the steady state solution (corresponding to the local amplitude of the oscillating electric field) on a time scale sufficiently shorter than $2\pi/(2kv_z)$ then the populations will show a smooth sinusoïdal oscillation. At each instant the value of ρ_{11} and ρ_{22} but also of the coherence are given by the steady state solution. The coherence will have the corresponding amplitude of oscillations slowly adjusting as the particle moves. This situation is shown in fig. 4.1 for the populations and in fig. 4.2 for the real part of the coherence $\rho_{12}\,(=\rho_{21})$.

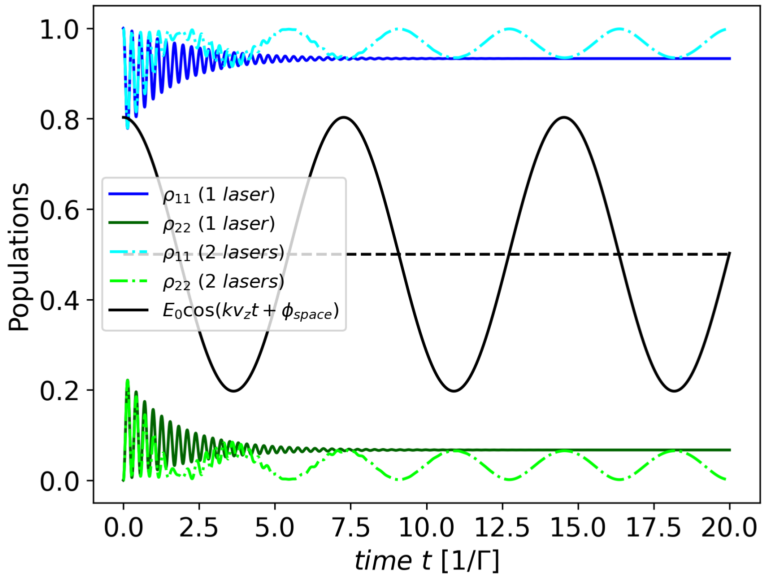

Figure 4.1: Time evolution of the populations of a moving 2-level quantum system perturbed by an off resonance monochromatic standing electric wave $E_0\cos(kz+\phi_{space})\cos(\omega t+\phi_{time})$ and with spontaneous emission. For this simulation $\Omega_R \approx 3\times 2kv_z$, $\delta \approx 11\times 2kv_z$ and $\Gamma \approx 0.5\times 2kv_z$. The shape of the spatial variation of the amplitude of the electric field of the standing wave inside the cavity is shown. The electric field curve is scaled and offset to see the correlation with the time evolution of the populations more easily.

From the situation shown in fig. 4.1, if the value of Ω_R is increased, i.e. if the electric field is increased, then the amplitude of the oscillations are higher and the smooth sinusoidal oscillations becomes sharp peaks. What happens is that the electric field is stonger than previously and thus its intensity is high (compared to the saturation intensity which is a property of the transition) over most part of the standing wave. Hence the nodes are associated to sharp peaks. This situation is shown in fig. 4.3. With a higher spontaneous emission rate and thus a higher damping, the population would evolve in a similar way with sharp peaks near the nodes except that the curve would be more smooth. This smooth evolution is shown in fig. 4.4. This absence of smoothness in fig. 4.3 is linked to the inability of the system to reach the steady state value corresponding to the instantaneous value of the amplitude of the electric field oscillations. These regimes can be thought of as repeating pattern of critical damping.

Eventually, if we reduce the detuning compared to the situation of fig. 4.1 instead of increasing the laser intensity, then the amplitude of the oscillations is more significant and the convergence is slower. As for the previous case, the system does not have time to reach the value of the steady state solution associated to the instantaneous value of the amplitude of the electric field oscillations. However this time the repeating transient evolution pattern is not a critical-damping-like shape but a subcritical damping of the Rabi oscillations. This situation is shown in fig. 4.5.

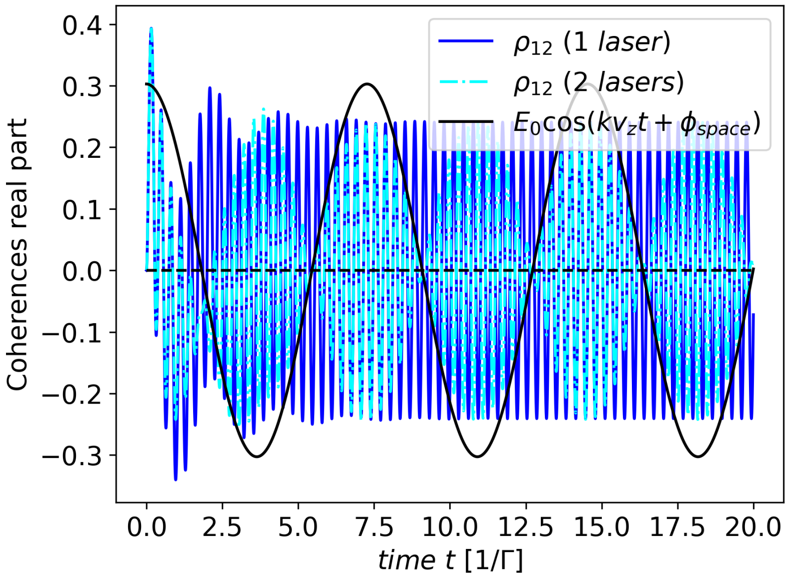

Figure 4.2: Time evolution of the real part of the coherence ρ_{12} (ρ_{21}) of a moving 2-level quantum system perturbed by an off resonance monochromatic standing electric wave $E_0\cos(kz + \phi_{space})\cos(\omega t + \phi_{time})$ and with spontaneous emission. For this simulation $\Omega_R \approx 3 \times 2kv_z$, $\delta \approx 11 \times 2kv_z$ and $\Gamma \approx 0.5 \times 2kv_z$. The shape of the spatial variation of the amplitude of the electric field of the standing wave inside the cavity is shown. The electric field curve is scaled to see the correlation with the time evolution of the populations more easily.

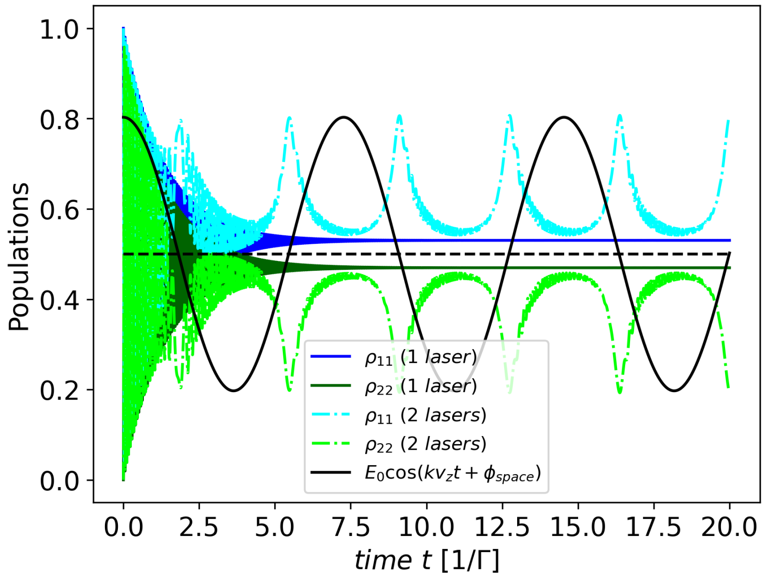

Figure 4.3: Time evolution of the populations of a moving 2-level quantum system perturbed by an off resonance monochromatic standing electric wave $E_0\cos(kz + \phi_{space})\cos(\omega t + \phi_{time})$ and with spontaneous emission. For this simulation $\Omega_R \approx 31 \times 2kv_z$, $\delta \approx 11 \times 2kv_z$ and $\Gamma \approx 0.5 \times 2kv_z$. The Rabi frequency Ω_R has increased compared to fig. 4.1 and so did the generalized Rabi frequency Ω. As can be seen on this graph, the oscillations of the populations are indeed more rapid. The shape of the spatial variation of the amplitude of the electric field of the standing wave inside the cavity is shown. The electric field curve is scaled and offset to see the correlation with the time evolution of the populations more easily.

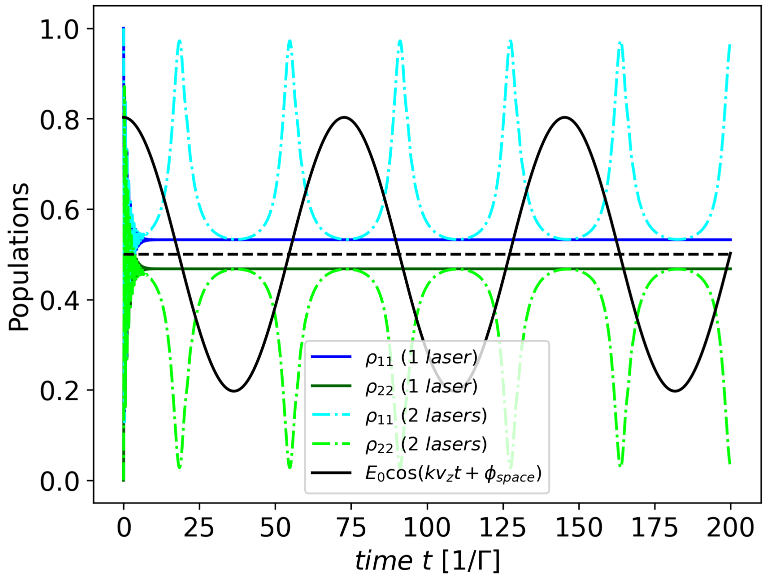

Figure 4.4: Time evolution of the populations of a moving 2-level quantum system perturbed by an off resonance monochromatic standing electric wave $E_0\cos(kz+\phi_{space})\cos(\omega t+\phi_{time})$ and with spontaneous emission. For this simulation $\Omega_R \approx 31\times 2kv_z$, $\delta \approx 11\times 2kv_z$ and $\Gamma \approx 5\times 2kv_z$. The shape of the spatial variation of the amplitude of the electric field of the standing wave inside the cavity is shown. The electric field curve is scaled and offset to see the correlation with the time evolution of the populations more easily.

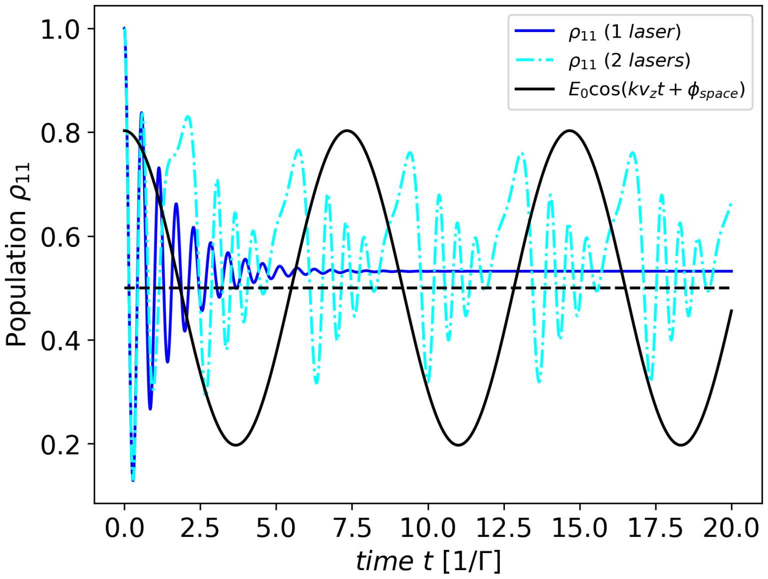

Figure 4.5: Time evolution of the populations of a moving 2-level quantum system perturbed by an off resonance monochromatic standing electric wave $E_0\cos(kz+\phi_{space})\cos(\omega t+\phi_{time})$ and with spontaneous emission. For this simulation $\Omega_R \approx 3\times 2kv_z$, $\delta \approx 2kv_z$ and $\Gamma \approx 6\times 2kv_z$. This time, it is the detuning that has been reduced compared to the simulation shown in fig. 4.1. For this reason the generalized Rabi frequency is lower and the oscillations of the populations are slower than in fig. 4.1. The shape of the spatial variation of the amplitude of the electric field of the standing wave inside the cavity is shown. The electric field curve is scaled and offset to see the correlation with the time evolution of the population more easily.

In conclusion, the diversity of behaviors can be summarized as follow. The frequency linked to the motion of the particle inside the cavity imposes a repetition pattern, which is sufficiently long to allow to reach a sinusoidal regime or not. If not the repeating pattern looks like a subcritical, a critical or supercritical damping of the Rabi oscillations. Note that all this is valid for single particle or a gas of particles with a lower rate of collisions in comparison of all the frequencies of the other physical processes that come into play. A summary of the parameters used in the simulations is presented in table 4.1 here below (where A_{21} is given by eq. 3.6):

	I	f	Γ	v_z
Fig. 4.1	$0.5\ E_{\mathrm{H}}^2/(a_0^2\hbar)$	$(1+10^{-2})f_0$	$\Gamma = A_{21}$	$6\ 10^{-2}\ E_{\mathrm{H}}a_0/\hbar$
Fig. 4.3	$50\ E_{\mathrm{H}}^2/(a_0^2\hbar)$	$(1+10^{-2})f_0$	$\Gamma = A_{21}$	$6\ 10^{-2}\ E_{\mathrm{H}}a_0/\hbar$
Fig. 4.4	$50\ E_{\mathrm{H}}^2/(a_0^2\hbar)$	$(1+10^{-2})f_0$	$\Gamma = 10\ A_{21}$	$6\ 10^{-2}\ E_{\mathrm{H}}a_0/\hbar$
Fig. 4.5	$0.5\ E_{\mathrm{H}}^2/(a_0^2\hbar)$	$(1+10^{-3})f_0$	$\Gamma = A_{21}$	$6\ 10^{-2}\ E_{\mathrm{H}}a_0/\hbar$

4.2 Computation of the absorption

4.2.1 Absorption computed from the polarization

From the evolution of the density matrix we want to extract the polarization as the first step towards the computation of the absorption coefficient. The polarization is computed exactly as previously from the coherences of the density matrix. However as the density matrix shows a repeating pattern over time for moving particles so does the polarization with a corresponding diversity of behaviors. The time evolution can thus be quite complex in general as shown in fig. 4.6 and this raises the question on how to compute the absorption coefficient: What is the analytical expression of the polarization? What is the link between the polarisation and the absorption coefficient ? These questions are not as straightfoward as before. There might not be any analytical expression as the density matrix and thus the polarization goes through a repeating transient regime signal in the general case. Previously the polarization data were fit on the steady state solution which was easier. Regardless of the existence of an analytical solution, one could simply compute the Fourier transform of the signal. However the difficulties would remain as the link between the Fourier transform signal and the absorption coefficient is not any easier. For this reason the computation of the absorption coefficient from the coherences has not been explored further in this master thesis.

4.2.2 Absorption computed from the the spontaneous emission

It is possible to obtain the absorption spectrum without computing the time evolution of the polarization of the quantum as explained in [36]. We saw in the second chapter that three processes take place when a quantum system interacts with light. These are stimulated absorption, stimulated emission and spontaneous emission. When the emission happens through stimulated emission the photons emitted are the same as the one absorbed. From the point of view of the absorption of the medium stimulated emission thus compensate some part of the absorption or stated otherwise it does not participate to the net absorption. Indeed in an absorption experiment we compare the intensity of the beam before travelling through the medium and after. Stimulated emission restitutes some part of the intensity that has been absorbed such that the only missing photons on the photodetector compared to the total amount incident on the medium are lost through spontaneous emission. Spontaneous emission is isotropic and

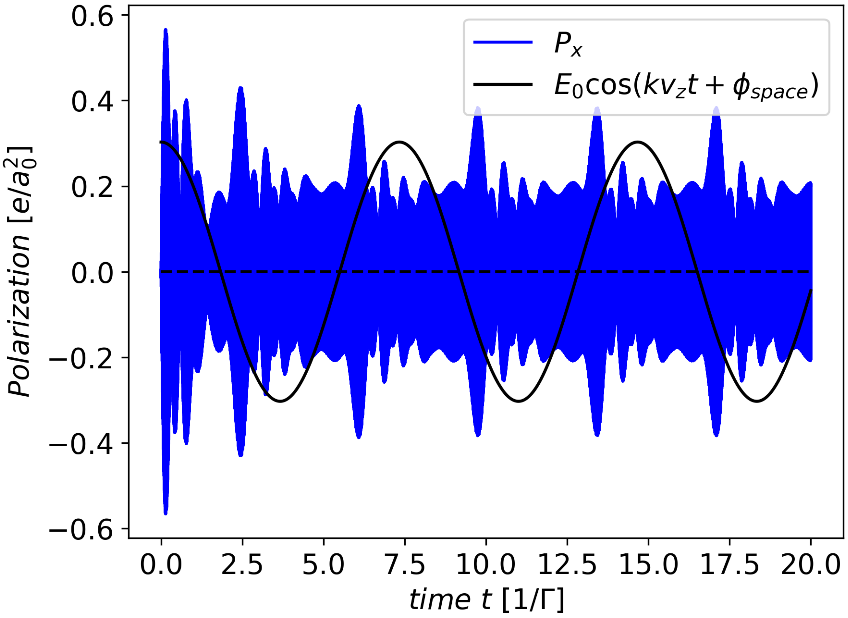

Figure 4.6: Time evolution of the polarization of a moving 2-level quantum system perturbed by an off resonance monochromatic standing electric wave $E_0\cos(kz+\phi_{space})\cos(\omega t+\phi_{time})$ and with spontaneous emission. For this simulation $\Omega_R \approx 3\times 2kv_z$, $\delta \approx 2kv_z$ and $\Gamma \approx 6\times 2kv_z$. The shape of the spatial variation of the amplitude of the electric field of the standing wave inside the cavity is shown. The value are scaled and offset to see the correlation with the time evolution of the polarization more easily.

obviously some part of the photons emitted through this process will reach the photodectector. Still, the total loss of photon which is directly related to the total loss of intensity is directly proportionnal to the spontaneous emission process. For this reason we can expect to obtain the absorption coefficient through spontaneous emission or more precisely counting the intensity lost through this process.

For a large amount of particle in the upper energy level the spontaneous emission rate Γ gives the number of photons emitted by unit time. The number density of particles in the upper energy level is $\rho_{22}N$ with N the number density of particles by unit volume and ρ_{22} the population in the upper energy level. Therefore the number of photons emitted through spontaneous emission by unit volume by unit time R_{photon} (noted R for rate) is

$$R_{\text{photon}} = \Gamma\rho_{22}N \tag{4.15}$$

Multiplying this quantity by the energy of a photon $\hbar\omega$ gives the total amount of energy emitted through spontaneous emission by unit time, i.e. the power of the loss through spontaneous emission by unit volume:

$$P_{\text{spont.}} = \hbar\omega\Gamma\rho_{22}N \tag{4.16}$$

The decrease of intensity of a beam as it propagates through an absorbing medium is given by

$$\frac{dI}{dz} = -\alpha I \tag{4.17}$$

Thus if we consider an infinitesimal volume with unit cross section along the laser beam axis $\Delta x\Delta y = 1$ and a length dz along the beam axis then we can consider the intensity of the beam to be constant inside the volume (see fig. 4.7). The infinitesimal loss of intensity is then $dI = -\alpha I dz$ where I is taken as the intensity inside the infinitesimal volume. As explained at

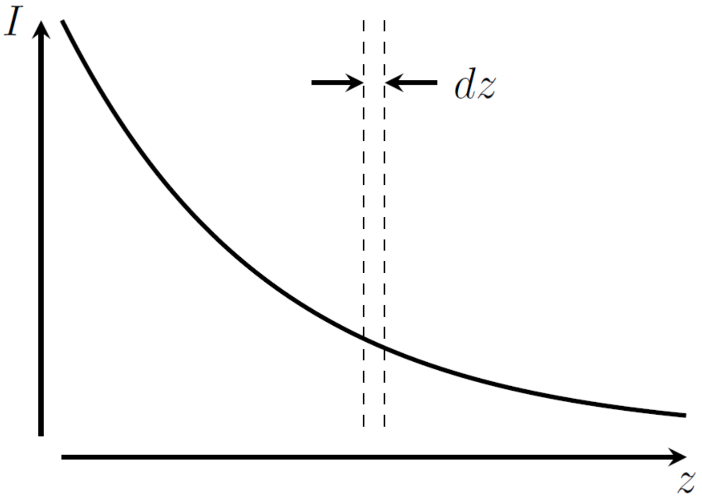

Figure 4.7: The infinitesimal decrease of intensity dI over a infinitesimal volume of cross section unity and length dz is $dI = -\alpha I dz$ where I is taken at the position of the infinitesimal volume.

the begining of this section we expect the loss of intensity through spontaneous emmision to be proportional to the net loss of intensity, i.e. the absorption, such that the following equation must holds:

$$\frac{dI}{dz} \propto -P_{\text{spont.}} = -\hbar\omega\Gamma\rho_{22}N \tag{4.18}$$

and thus

$$-\hbar\omega\Gamma\rho_{22}N \propto -\alpha I \tag{4.19}$$

such that eventually

$$\alpha \propto \frac{\hbar\omega\Gamma\rho_{22}N}{I} \tag{4.20}$$

At the beginning of this chapter we saw that the populations ρ_{11} and ρ_{22} does not reach a steady state value when the particle moves in the standing wave inside the cavity. As the absorption lineshape from experiment results do not oscillate over time, we can assume that even though moving particles have a time evolving response, the total contribution of a specific velocity class does not vary over time. Indeed at steady state the spatial distribution of velocities does not varies in time such that if a moving particle goes from a maximum of absorption to a minimum then another particle with the same velocity goes from a minimum to a maximum. If we assume ergodicity then averaging over space for a given velocity is the same as averaging over time for this velocity. Thus the population ρ_{22} in the last equation must be averaged over a time period to get the steady state absorption contribution of the velocity class considered. If this time period start from t_0 and ends at t_f we can define the average population as

$$\tilde{\rho}_{22} = \frac{\int_{t_0}^{t_f} \rho_{22}\, dt}{t_f - t_0} \tag{4.21}$$

Eventually this gives the following formula

$$\alpha \propto \frac{\hbar\omega N\Gamma}{I}\frac{\int_{t_0}^{t_f} \rho_{22}\, dt}{t_f - t_0} \tag{4.22}$$

Before looking at moving particle, let's check the agreement with theory for a particle at rest. For this the population ρ_{22} must be taken at steady state.

The result of the numerical evaluation of the absorption coefficient through spontaneous emission are shown in fig. 4.8. Unfortunately the output of the implemented algorithm described above did not agreed with the theoretical formula as far as the value of the coefficient is concerned. However when multiplied by a correction coefficient (for the simulation shown in fig. 4.8 this coefficient is 158) the curves obtained through numerical computation match the theoretical curves perfectly. In other words the lineshape, i.e. the dependence of the absorption coefficient on the detuning, match perfectly. More importantly we can see that the dependence on the intensity correctly reproduced saturation. We can thus perform saturation spectroscopy simulation from the spontaneous emission confidently. One must only take care to fit the numercial results once on the theoretical curve to find the accurate correction coefficient.

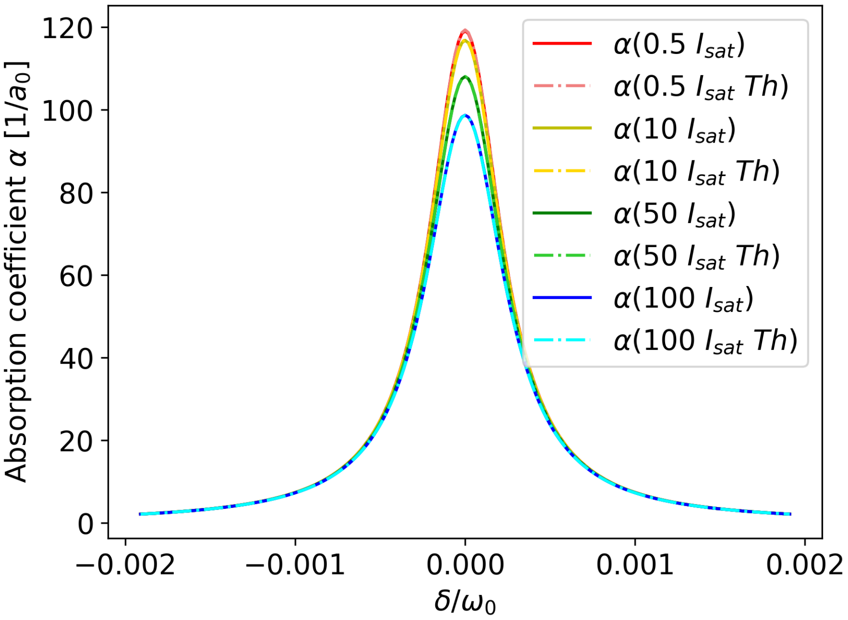

Figure 4.8: Lorentz absorption lineshape of a stationnary two level quantum system in an oscillating electric field. The absorption coefficient is computed from the spontaneous emission and adjusted to the theoretical value (dashed curve) given by $\alpha = \omega/c\chi''$ where χ'' is given by the imaginary part of eq. 2.84. The coefficient used to adjust the numerical value is 158.

4.2.3 Absorption lineshape of a moving particle

We now turn our attention to a moving particle. The goal is to compute the absorption for a moving particle using the same method as for a particle at rest in the previous section. For this reason the code used to compute the absorption for particles at rest is the same as for moving particles. Only the time sampling is different because an adaptative time sampling for the moving particles has been implemented. The implemented time sampling ensures that the evaluation of the absorption coefficient is done at steady state for particles at rest or when the periodic solution is reached in the case of moving particles.

Before attempting to simulate the absorption of a gaseous medium with a velocity distribution we analyse the evolution of the lineshape of the absorption coefficient with respect to change in the velocity along the cavity axis v_z. The absorption coefficient is evaluated over the periodic solution thus not taking into account the transient regime of the density at the beginning of the simulation (as for particles at rest when reaching steady state). This is equivalent to considering that the transit time is infinite. In such a situation the particle moving at a certain velocity will have a periodic evolution of ρ_{22} through time. However all the particles belonging to the same velocity class will not have the same initial value for $\rho_{22}(t)$ as the spatial phase of the electric field standing wave is different for particles at different locations inside the cavity. Hence, the absorption in this case is given by averaging over one period of the population $\rho_{22}(t)$. In the numerical implementation the average is taken over several time the period of ρ_{22} to ensure numerical convergence.

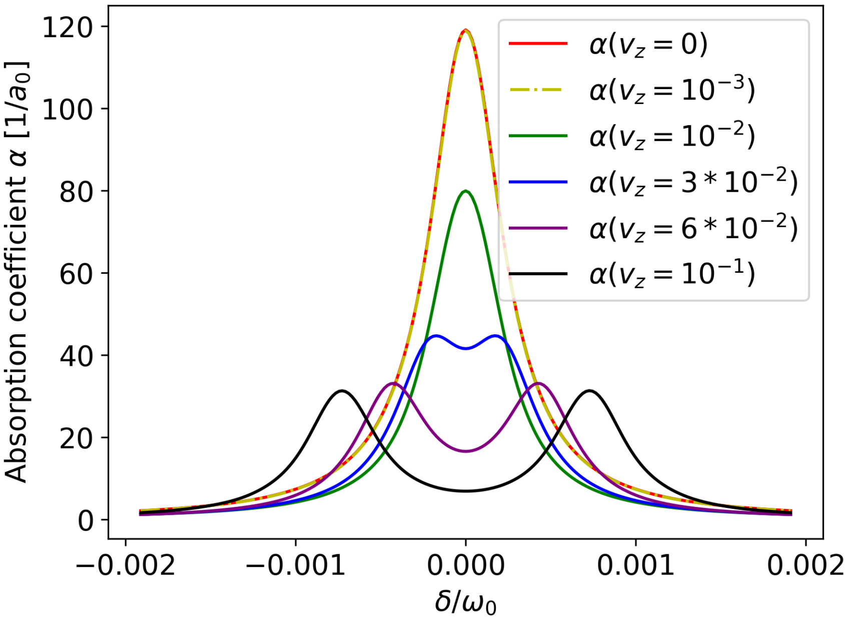

Figure 4.9: Absorption lineshape of a 2-level quantum system moving in a standing wave for several different velocities (with in addition the special case of null velocity, i.e. a particle at rest). The intensity of the standing wave is 0.5 I_{sat}. The absorption coefficient is computed from the spontaneous emission and adjusted to the theoretical value (dashed curve). This coefficient is the same for all velocities. When the particle is stationnary (or with a sufficiently low velocity, see below) the position of the particle is supposed to correspond to a maximum of the standing wave. The unit of the velocity in the legend is $E_{\mathrm{H}}a_0/\hbar$ but was omitted in the figure to avoid an overlap with the curves.

The evolution of the absorption coefficient lineshape with the velocity is shown in fig. 4.9. We can see that for the toy model the absorption lineshape is not affected noticeably by the velocity until at least $v_z = 10^{-3}\ E_{\mathrm{H}}a_0/\hbar$. Then the Lorentzian peak decreases as the velocity increases until it split into two Lorentzian peaks. This two peaks are just the Lorentz absorption lineshape shifted due to the Doppler shift. There are two peaks because each velocity class perceives one half of the standing wave amplitude as a blue-shifted propagating wave and the other half as a red-shifted propagating wave. Each peak has the same FWHM as the absorption peak of the particle at rest (FWHM: $\Delta\omega = 5.5\ 10^{-4}\omega_0$). On the contrary we can notice the height of the peaks not being equal to half of the Lorentzian peak at v_z. This is expected since the two peaks are due to the absorption of only one half of the amptlitude of the electromagnetic wave. When the velocity is 0 (or so small that the simulation time required to travel across a wavelength of the standing wave is too large and thus impossible to simulate) the particle position in the standing wave is supposed to correspond to a maximum of the electric field amplitude. For this reason, particle at rest sees a sinusoidal wave $E_0 \cos(\omega_{\mathrm{laser}} t)$ and the associated intensity is proportional to E_0^2. The particles moving in the standing wave see two counterpropagating wave with half the amplitude $E_0/2$ and thus one quarter of the intensity $E_0^2/4$. The decrease in absorption by one quarter is thus expected because we compare moving particles with particles at rest at the maximum of the standing wave. However, this looks like the sum of the intensity of the two propagating waves does not equal the total intensity of the standing wave but this is not the case. The moving particles see the variation of the electric field through time and space. To obtain the intensity of the standing wave we must take into account the variation of the standing wave across space. The variation across space can be taken into account by taking the effective value of the electric field over a wavelength of the standing wave. This is $E_0/\sqrt{2}$ and thus the intensity is $E_0^2/2$ which is equal to the sum of the intensity of the two propagating waves. The results here thus show a comparison between two propagating wave with an amplitude $E_0/2$ and one propagating wave with amplitude E_0. In the next section we consider the absorption of a gas in a cavity and discuss how to deal with the contribution of particles at rest at different locations of the standing wave.

4.3 Doppler broadened spectrum and Lamb-dip

We now turn our attention to the absorption spectrum obtained for a gaseous medium.

4.3.1 Particle at rest: dealing with different position in the standing wave

In the previous section the absorption spectrum of particles with different velocities was computed. This absorption coefficient was obtained through the integration over the periodic variation of the population $\rho_{22}(t)$ over time. This procedure allows to exctract an absorption coefficient that is time independant. As particles with a non-zero velocity move inside the standing wave, the average over time correspond also to an average over space. However particles with a null velocity do not move at all and the contribution of one specific particle at rest on the total absorption obviously depends on its location along the standing wave spatial variation. As the standing wave is a sinusoïdal wave, the expected contribution from a uniform distribution over space of particle at rest is one half of the contribution of a particle located at a maximum of the standing wave, multiplyied by the density of particles at rest. The effective absorption of one particle is thus one half of the maximum absorption. This is expected since the effective amplitude of a sine wave is $1/\sqrt{2}$ and thus the effective intensity, linked to the square of the electric field amplitude, is $I/2$. This is what is observed in fig. 4.10

This discussion raises the question of the validity of this approach. Indeed, the signal observed in an absorption experiment is obtained through a photon detector that "count" photons. It is thus linked to the intensity of the light wave at the surface of the detector but it depends also on the integration over time due to the acquisition time of the detector. Hence, whereas it is obvious that particles at rest must be averaged over the spatial variation of the standing wave, some velocity might required also average somehow over space. For non-zero but arbitrary small velocities the contribution to the absorption must converge towards the one of the particles at rest but we saw in the previous section that the contribution of small velocities converges towards the absorption coefficient of a particle at rest at a maximum of the standing wave. We will not deal with this issue further in this thesis. In the following, the integration over the velocity distribution will be symmetric around $v_z = 0$ and excluding $v_z = 0$. We will consider also that the sampling of the velocities in the Maxwell-Boltzmann distribution will be such that the numerical step between the first velocity sampled before zero and after zero is

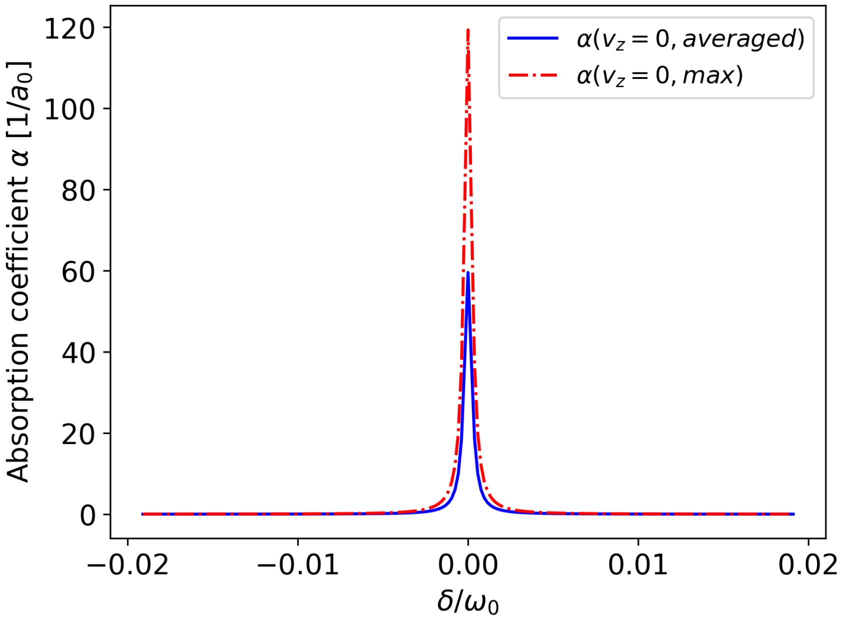

Figure 4.10: Absorption lineshape of a stationnary 2-level quantum system in a standing wave. The intensity of the standing wave is $0,5\ I_{sat}$. The absorption coefficient is computed from the spontaneous emission and adjusted via a coefficient equal to 158. The dashed curve is the Lorentzian absorption spectrum of a particle lying at the maximum of the standing wave. The full blue curve is the average of the Lorentzian absorption from stationnary particles uniformly placed along the spatial variation of the standing wave.

large enough so that averaging over a time period correctly average over the spatial distribution.

4.3.2 Adaptative velocity sampling for splitted Lorentzian peak

When computing the absorption spectrum of a gas, the contribution to the absorption of each velocity class must be added. In the case of a single propagating electromagnetic wave, we saw that for each angular frequency of the laser ω the absorption coefficient is given by a convolution between the velocity distribution and the Lorentzian absorption profile. The convolution was due to a single Doppler shift of the Lorentzian absorption peak as the velocity distribution is scanned. For the present case the existence of two counterpropagating laser lead to the following integral

$$\alpha(\omega) = \int_{-\infty}^{\infty} f_{v_z}(v_z)\alpha_{v_z}(\omega, v_z)\ dv_z \tag{4.23}$$

where f_{v_z} is the one dimensional velocity distribution along the cavity axis and α_{v_z} is the absorption coefficient contribution of the velocity class v_z. The integral is thus not a convolution anymore because the Lorentzian peak splits into two smaller peaks instead of just shifting position.

One way to evaluate the previous integral is to compute α_{v_z} at each value of the numerical sampling of f_{v_z}. Then one compute the product of $f_{v_z}\alpha_{v_z}$ at each sampling point and perform numerically the integration with a integration scheme already existing. The integration scheme used in this work is the Simpson numerical integration. This approach works fine as long as the velocity sampling is adequate. Indeed the absorption profil of a single velocity class α_{v_z} is composed of two Lorentzian peaks (for non zero velocities) with different positions in the velocity space for different values of the angular frequency of the laser ω. If the sampling of the velocies is not well resolved, the Lorentzian peaks might be centered between two sample points of the velocity distribution. This situation would lead to a truncation or even a complete miss of the Lorentzian peaks. One could just ensure that the sampling is dense enough but this would be computationnaly demanding and also unefficient as the same dense sampling would cover the absorption curve α_{v_z} outside of the two Lorentzian peaks. For this reason an adaptative velocity sampling has been implemented.

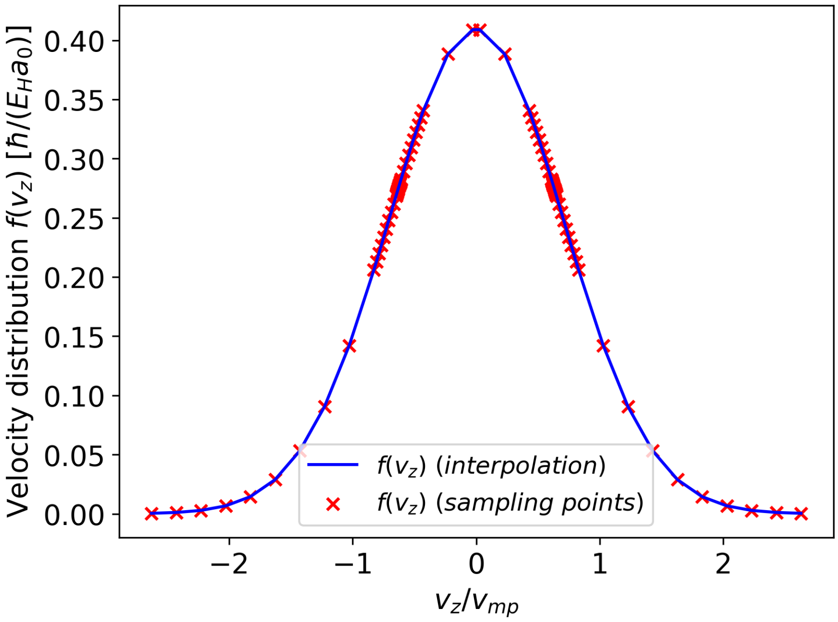

Figure 4.11: Example of the adaptative velocity sampling implemented. The sampling is composed of two set of points, one for the velocities below zero and one for the velocities above zero. These two sets are centered on the velocity corresponding to the resonant frequency as perceived by the particle taking into account the Doppler shift. For this sampling $\omega = \omega_0 + 0.2$ rad. $E_\mathrm{H}/\hbar$

The adaptative velocity sampling is shown in fig. 4.11. For a given value of ω two sets of sampling point are generated. Each of these sampling sets is shifted from v_z to the center of the absorption peak above $v_z = 0$ for one and below $v_z = 0$ for the other. Let's call the velocity corresponding to the centers of the peaks v_c and $-v_c$. Then the most propable velocity of the Maxwell-Boltzmann distribution is computed

$$v_{mp} = \sqrt{\frac{2k_B T}{m}} \tag{4.24}$$

with k_B Boltzmann constant, T the temperature of the gas and m the mass of the particle. The sampling then proceeds as follows: the velocity distribution is evaluated at N_points points between $v_c + 2v_{mp}$ and $v_c + 2v_{mp}/10$ but also bewteen $v_c - 2v_{mp}$ and $v_c - 2v_{mp}/10$ for the peak centered at v_c. The velocity is then again sampled with N_points between $v_c + 2v_{mp}/10$ and $v_c + 2v_{mp}/100$ and between $v_c - 2v_{mp}/10$ and $v_c - 2v_{mp}/100$. This procedure is repeated as many times as required. The same sampling is done for the other peak located at $-v_c$. This allows to have a denser sampling close to the two Lorentzian peaks. Eventually the sampling points from the peak located at v_c might fall below zero and conversely the one from the peak at $-v_c$ might fall above zero. These points are simply discarded to avoid an overlap between the sampling relative to each peak ($v_z = 0$ is also discarded for reasons explained in the previous section).

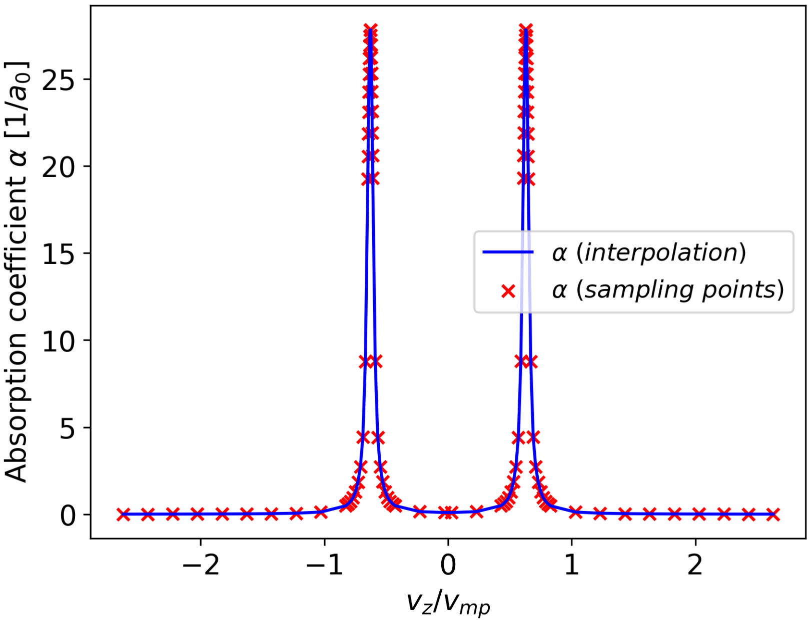

Figure 4.12: Example of the adaptative velocity sampling implemented. On the figure is shown the absorption coefficient computed for each sampled point of the velocity distribution. We can observed that the sampling is adapted to the two Doppler shifted peaks occurring in the absorption curve relative to the velocity. The more refined sampling close to the center of the peak allow to better account for the area under the curve when the integration over all velocity classes is performed to obtain the value of the absorption coefficient. This simulation corresponds to the sampling of fig. 4.11, i.e. $\omega = \omega_0 + 0.2$ rad. $E_{\mathrm{H}}/\hbar$.

This sampling procedure leads to the sampling shown on fig. 4.11. We can see clearly a symetric sampling around zero with two denser regions shifted from $v_z = 0$. In fig. 4.12 we can see that the sampling correctly match the absorption peaks for the considered velocity class. This allows a good resolution of the absorption peaks and thus a good evaluation of the integral 4.23.

4.3.3 Saturated absorption spectrum: Lamb-dip

The Doppler broadened absorption curve can now be computed using for each laser frequency the adaptative velocity sampling. This allows to capture precisely the area under the curve of the absorption coefficient when integrating over all velocity classes. In the previous section the sampling was $N_{\text{points}} = 10$ for the figure to be clear. However, this sampling leads to oscillations on the Doppler broadened absorption curve that are important relatively to the close-up region chosen for the numerical evaluation of the curve. This is due to the poor density of sampling points. With an increased number of points these oscillations reduces and one obtains the curves plotted in fig. 4.13 when using $N_{\text{points}} = 20$. The curves are smooth and one clearly spot the apparition of a Lamb-dip above the saturation intensity threashold. This Lamb-dip is more pronouced as the laser intensity increases as expected. The Lamb-dip is also symmetric and centered on the resonance frequency ω_0 of the system. This thus constitutes a benchmark in this thesis for the numerical evaluation of the absorption lineshape. It must be stressed that the benchmark is on the lineshape and not the absolute value of the curve because it required a fit to the theory. Despite this small issue one can carry on with this approach as the ultimate goal is to explain the asymmetric spectrum which is mostly a qualitative feature of the lineshape. The absolute value of the absorption coefficient can be adjusted with a correction factor.

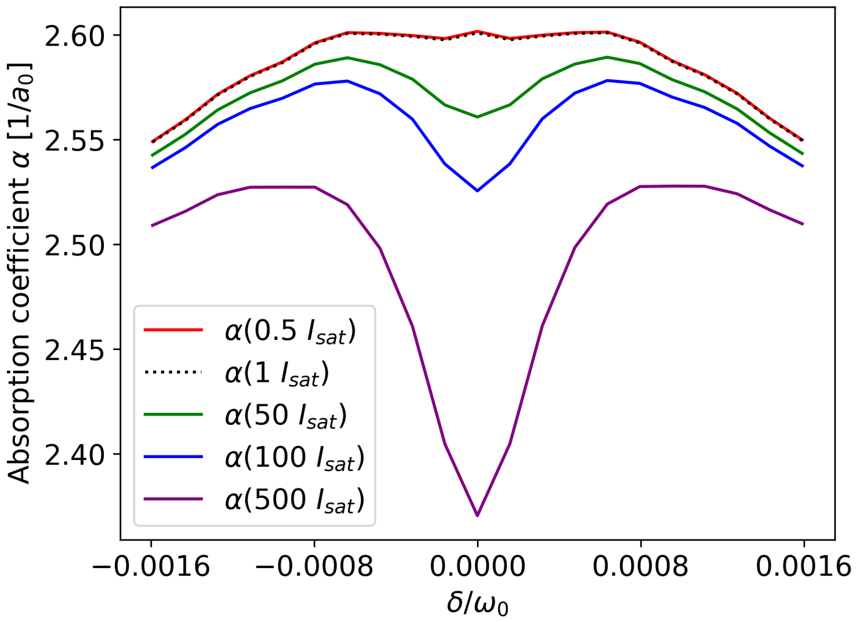

Figure 4.13: Close-up view on the top of the Doppler broadened absorption curve. The curve is evaluated for several laser intensities and we observe that above the saturation intensity a Lamp dip start to form due to saturation of the medium. Note that the value of the absorption are corrected with a coefficient of 158 as was explained before when fitting on the theoretical curve. Also what seems like a small peak on the red and black curves is just a numerical artefact: numerical oscillations were present on the curve for less dense numerical sampling of the velocity distribution. The small peak is only a residue of these oscillations and increasing the sampling would solve this. However the present graph was already very demanding in terms of numercial ressources and we already see that the simulation converges towards a smooth curve.

Chapter 5

Application to HD cavity spectroscopy

5.1 Parameters used for the HD gas and for the laser

Now that we have a functional code at hand that can simulate the Lamb-dip that forms in a saturated absorption experiment where the probe and the pump are both intense, we can look at the particular case of HD saturated absorption. Therefore we will first recall the physical parameters of the HD molecule as well as the parameters of the laser cavity. The reference for the present numerical simulations will be the saturated absorption experiment on HD done by the research group of Wim Ubachs from Amsterdam [4]. The goal of this chapter is to apply the numerical calculation of the absorption coefficient to realistic values for the HD $R(1)$ $(2-0)$ transition line and check that the simulation correctly reproduces a symmetric lineshape with a Lamb-dip for those values. This also implies checking that the correct lineshape is obtained even when the time evolution of the density matrix does not allow to reach steady state.

5.1.1 Parameters for the HD transition and HD gas

The HD $R(1)$ $(2-0)$ transition has the following physical properties:

Property	International System units	Atomic units	Sources
$f_{R(1)\ (2-0)}$	217 105 181 895 kHz	$5.251523382054423\ 10^{-3}\ \mathrm{E_H}/\hbar$	[4]
$D_{R(1)\ (2-0)}$	$6.671\ 10^{-35}$Cm	$7.869\ 10^{-6}\ e\mathrm{a}_0$	[33]
$\Gamma_{\text{spont. em.}}$	≈ 1 Hz	$2.419\ 10^{-17}\ \mathrm{E_H}/\hbar$	[4]
$\Gamma_{\text{Collisions}}$	$\approx 10^5$ Hz	$2.419\ 10^{-12}\ \mathrm{E_H}/\hbar$	[12]

The value of the dipole moment of the transition corresponds to $0.20\ 10^{-4}$D. The value of the spontaneous emission rate 1 Hz is very low compared to the relaxation rate due to collisions. This later value is taken from fig. 5.1. In this figure is shown a variation with pressure of the central frequency of the Lamb-dip as well as its full width at half maximum (FWHM). We already saw in the first chapter that collisions in a gas can induce an increase in the FWHM of the Lamb-dip if the collision rate shortens the lifetime of the upper level significantly compared to all the other processes affecting the lifetime of the upper energy level. On the contrary, we did not discuss so far the shift of the central frequency of the Lamb-dip due to collisions.

A shift of the central frequency of the dip means a shift of the transition frequency of the saturated transition under study. The reason for this shift is the short range interaction of the particles that constitutes the gaseous medium. Let's consider a collision between two particles and let's consider that one of the two particles absorbs a photon. Let's call the absorbing particle *absorber* and the other one *perturber*. The perturber will obviously come closer to the absorber in a collision process. The collision itself reduces the lifetime of the upper energy state of the transition but on top of that the presence of the perturber also modifies the energy levels of the absorber due to short range interactions. The higher the gas density the more the particles are closely packed together thus reinforcing the overall contribution of the short range interactions. The change in energy levels due to these short range interactions translates into a change in the frequency transition of absorbing particles. This qualitative explaination can be translated into detailed calculations as done in [37]. The details of the quantum treatment of collisions is however not considered in the present work. Moreover the shift of the central frequency is not implemented into the code. In fact, neither the linear variation of the central frequency nor the linear variation of the broadening is implemented in the code so far (This linear variation can easily be implemented using the slope of the curve of fig. 5.1 which is given in the corresponding paper [12]). Thus the results for the simulation of the HD absorption spectrum in this work were obtained for only one value of the pressure. The research group at Amsterdam did the absorption experiment for pressure values p of 0.25 Pa, 0.5 Pa, 2.5 Pa and 10 Pa. The collision rate $\Gamma_{\text{Collisions}} = 10^5$ Hz corresponds to the lowest pressure in the cavity. For this reason the simulations were done using a pressure of 0.25 Pa which is the lowest pressure used by the reasearch group. Eventually, the temperature of the HD gas was the room temperature in the Amsterdam experiments. So the temperature used in the simulation is $T = 300$ K as the exact value is not mentioned in their paper. The properties of the HD gas in the simulations are summarized in the following table:

Property	International System units	Atomic units	Sources
p	0.25 Pa	$8.497\ 10^{-15}\ \mathrm{E_H/a_0^3}$	[4]
N	$1.002\ 10^{-4}$ mol/m^3	$1.485\ 10^{-35}\ \mathrm{mol/a_0^{-3}}$	[4]
T	300 K	300 K	[4]

The density is evaluated from the ideal gas law:

$$N = \frac{p}{RT} \tag{5.1}$$

with R the ideal gas constant (SI units : $R = 8.314\ \mathrm{JK^{-1}mol^{-1}}$, Atomic units : $R = 1.907\ 10^{18}\ m_e \mathrm{E_H^2 a_0^2} \hbar^{-2} \mathrm{K^{-1} mol^{-1}}$).

5.1.2 Parameters for the laser cavity and transit time

The power circulating in the cavity of the Amsterdam experiment is evaluated at $P = 100$ W [4]. The intensity of the laser is the relevant quantity for the simulation so we need to divide the power by the cross section of the laser. A good measure of the order of magnitude of the laser cross section is of course its waist w_0. The size of the waist is $w_0 = 450\mu$m [38]. The cross-section is then simply obtain by $A = \pi w_0^2$. From the light intensity we can extract the electic field amplitude and compute the Rabi frequency Ω_{R}. This gives

Property	International System units	Atomic units	Sources
P	100 W	$5.548\ 10^2\ \mathrm{E_H^2}/\hbar$	[4]
w_0	450 μm	$8.504\ 10^6\ \mathrm{a_0}$	[38]
A	0.636 mm^2	$2.272\ 10^{14}\ \mathrm{a_0^2}$	/
I	$1.572\ 10^2$ W/mm^2	$2.442\ 10^{-12}\ \mathrm{E_H^2}/(\hbar \mathrm{a_0^2})$	/
Ω_{R}	$2.000\ 10^4$ Hz	$4.839\ 10^{-13}\ \mathrm{E_H}/\hbar$	/

The interaction of the gas with the laser is quite complex because the gas is made of a lot of particles having different trajectories and different velocities along those trajectories. The existence of different trajectories means the existence of different paths across the Gaussian

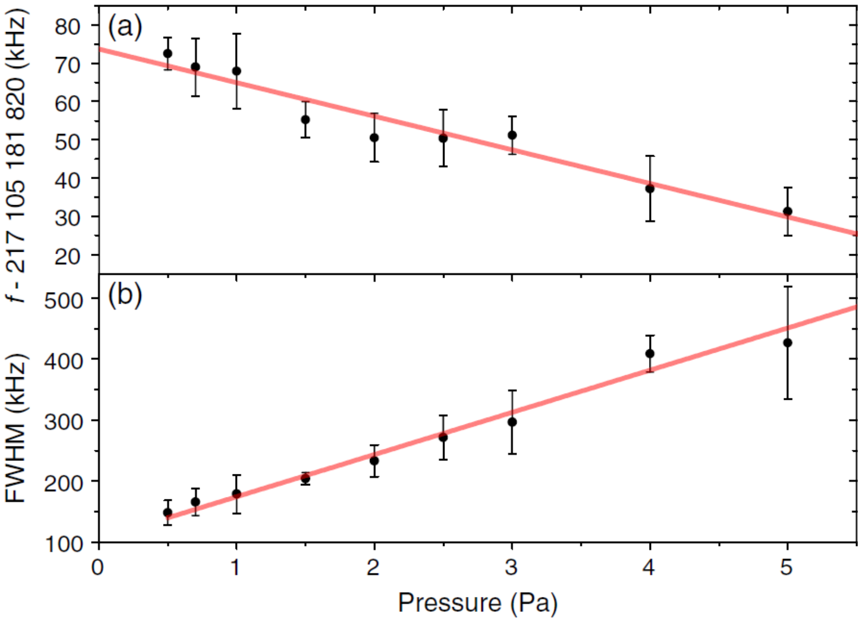

Figure 5.1: (a) Evolution of the central frequency of the Lamb-dip of the HD saturated $R(1)$ $(2-0)$ transition with pressure. (b) Evolution of the full width at half maximum of the Lamb-dip of the HD saturated $R(1)$ $(2-0)$ transition with pressure. Image from [12]

beam and thus complex variations of the laser amplitude across space must be taken into account. Also the velocity distribution in the gas implies that the interaction time with the laser varies from one particle of the gas to another. This means that one would need to sample numerically a significant amount of those trajectories and velocities. This is computationnally very demanding and needs a significant adaptation of the code used to obtain the Lamb-dip in the previous section.

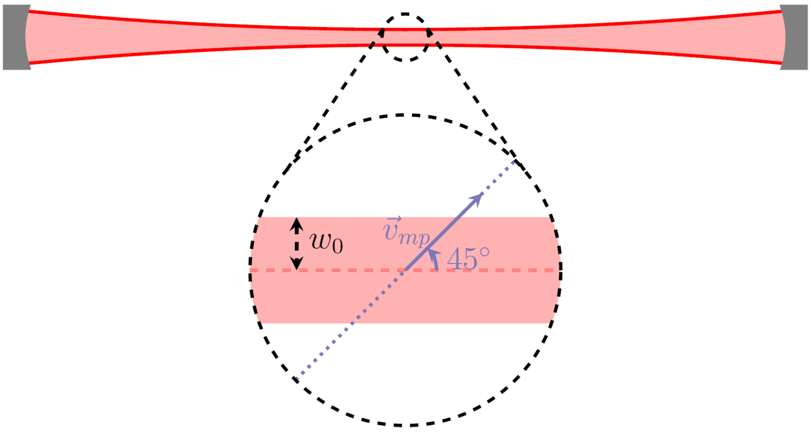

Figure 5.2: Schematic of the Gaussian laser beam with a zoom on the waist of the beam below. The zoom corresponds to what is actualy implemented in the code. In blue color is depicted the path of a HD molecule crossing the beam at a 45 degrees angle close to the waist of the beam with a velocity equal to the most probable velocity of the HD gas velocity distribution. This is used to evaluate the order of magnitude of the transit time in the absorption cavity spectroscopy of Amsterdam.

Instead, we will follow what was done in [36], i.e. the same paper that showed that the absorption could be computed from the spontaneous emission solely. In this paper they assumed that "*assuming a fixed uniform field amplitude, corresponding to the central intensity of a Gaussian laser profile, and a fixed interaction time, are reasonable approximations*". The absorption spectrum studied in [36] corresponds to strong transition in the Rb atom and so the steady state regime is reached much faster than the transit time. Therefore the assumption might not hold for the weak transition of the HD molecule considered in this chapter as the time to reach steady state for HD is much longer than the transit time. However as it saves a lot time by avoiding sampling the trajectories across the laser beam it is worth trying to see the results.

The fixed amplitude used in the simulations of this chapter is the one derived from the intensity value calculated before. In this chapter, the fixed interaction time is chosen to be the one of a particle crossing the beam at a 45° angle at the position of the beam waist with a velocity equal to the most probable velocity of the Maxwell-Boltzmann velocity distribution. This situation is illustrated in fig. 5.2. The beam waist gives the caracteritic size of the beam cross section as said before and taking an angle of 45° is a compromise between particles with trajectories perpendicular to the beam axis and particles with trajectories along the beam axis. In the numerical implementation the simulation start at $t = 0$ with the fixed electric field amplitude until $t = t_{\text{transit}}$. This method thus models the laser as an abrupt field variation across space. With the parameters cited above, the most probable velocity in the HD gas is $v_{\text{mp}} = 1290$ m/s and this translates into a transit time of $t_{\text{transit}} = 9.870\ 10^{-7}$ s (In atomic units: $v_{\text{mp}} = 5.894487690816786\ 10^{-4}\ \mathrm{a_0 E_H}/\hbar$ and $t_{\text{transit}} = 4.080\ 10^{10}\ \hbar/\mathrm{E_H}$).

5.2 Results of the simulations

5.2.1 Evolution of the populations

Fig. 5.3 shows the time evolution of the population in the upper energy state over the interaction time chosen for the simulations. The laser frequency has no detuning and matches the resonance frequency of the transition in the reference frame of the laboratory. We see that the transit time is shorter than the period of the Rabi oscillations. The parameters of the laser cavity are based on [4] where the Lamb-peak and Lamb-dip extended over a frequency range on the order of 1 MHz. We can look at some multiples of the velocity v_{1MHz} corresponding to a Doppler shift of 1 MHz. This corresponds to the different curves shown in fig. 5.3 and we see that the area under the ρ_{22} curves decreases significantly when the velocity along the beam axis is close to v_{1MHz}. Therefore this means that the spontaneous emission is very low and so is the absorption coefficient. Also one observes the oscillations of the population as the HD molecule travels along the beam axis for $v = v_{1\text{ MHz}}$ and $v = 2v_{\text{1MHz}}$. We see that the period of those oscillations is reduced by one half when the velocity doubles comfirming this interpretation. For a velocity of 0.1 v_{1MHz} the area under the curve decreases slightly compared to $v = 0$.

In fig. 5.4 is also shown the time evolution of the upper energy level but this time the laser has a detuning of $\delta = 1$ MHz in the reference frame of the laboratory. We see that the absorption of the particle at rest and the particle moving at $v = 0.1v_{\text{1MHz}}$ is lower. The particle moving at $v = v_{\text{1MHz}}$ benefits from a Doppler shift of 1 MHz that cancels the detuning of one of the two counterpropagating waves inside the cavity (while the other wave has an increased detuning). The evolution of the population for this particle thus looks a bit like the one of the particle at rest when the laser was not detuned but with oscillations superposed on it due to the motion of the particle inside the standing wave. We can check that the population at the end of the transit has reached $\rho_{22} \simeq 0.0009$ for the particle moving at $v = v_{\text{1MHz}}$ when

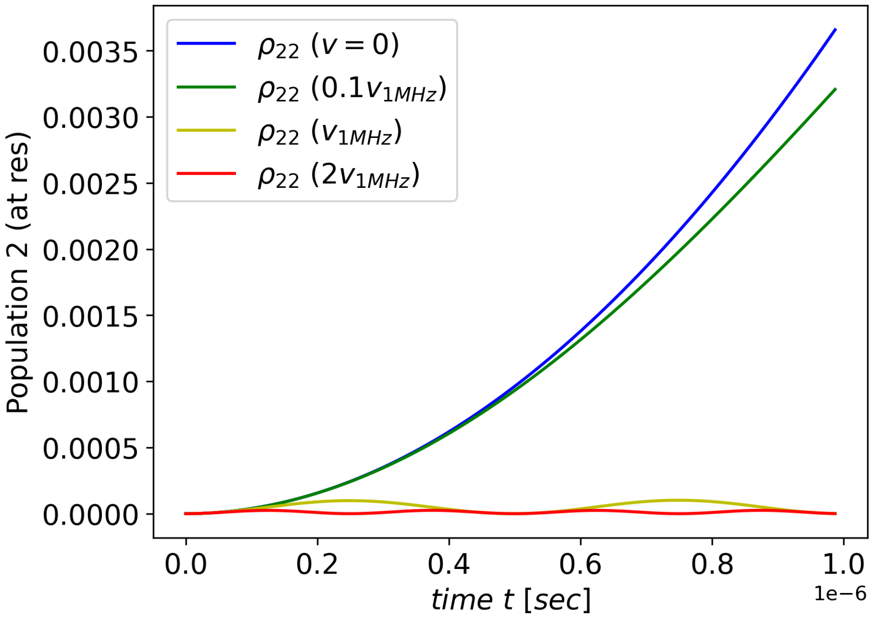

Figure 5.3: Time evolution of the population in the upper energy state over an interaction time that corresponds to a HD particle moving along a trajectory at 45° angle at the beam waist for a HD particle travelling at the most probable velocity. The different curves correspond to different velocity along the axis of the cavity. These velocities are multiple of $v_{1\mathrm{MHz}}$ which is the velocity that corresponds to a Doppler shift of 1 MHz. The laser is resonant.

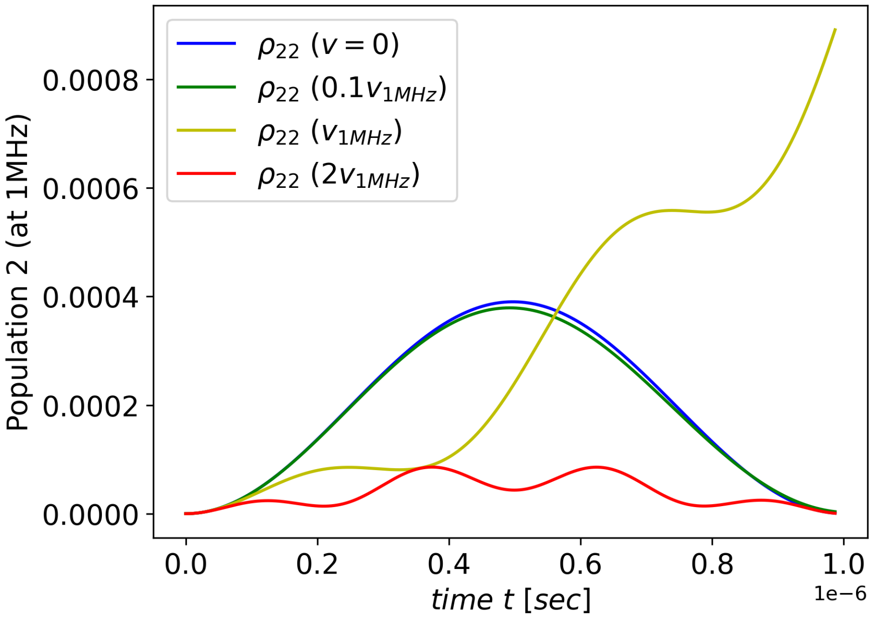

Figure 5.4: Time evolution of the population in the upper energy state over an interaction time that corresponds to a HD particle moving along a trajectory at 45° angle at the beam waist for a HD particle travelling at the most probable velocity. The different curves correspond to different velocity along the axis of the cavity. These velocities are multiple of $v_{1\mathrm{MHz}}$ which is the velocity that corresponds to a Doppler shift of 1 MHz. The laser frequency has a detuning of 1 MHz.

the laser has a detuning of 1 MHz. This is consistent because it corresponds to 1/4 of the population reached by the particle at rest at a maximum of the standing wave when the laser is not detuned $\rho_{22} \simeq 0.0036$. We saw in the previous chapter that the height of the absorption peak for a moving particle is divided by four. As the absorption is given by the area under the ρ_{22} curve, we expect this area to be divided by four and, because the interaction time is the same, the value of ρ_{22} must be divided by four. Eventually, for the laser detuned by $\delta = 1$ MHz, we can compare the evolution of ρ_{22} for the particle at rest and for the particle moving at $v = 2v_{\mathrm{1MHz}}$. The particle at rest perceives the laser frequency with the detuning of 1 MHz obviously and so does the moving particle except only one of the two propagating waves is seen with a 1 MHz detuning (because of the opposite Doppler shift). The amplitude of the population ρ_{22} during the interaction time is thus lower for the moving particle as expected. Moreover the moving particle shows clear oscillations due to its motion through the standing wave. The observations are thus in agreement with what was expected from the toy model.

5.2.2 Evolution of the absorption with velocity

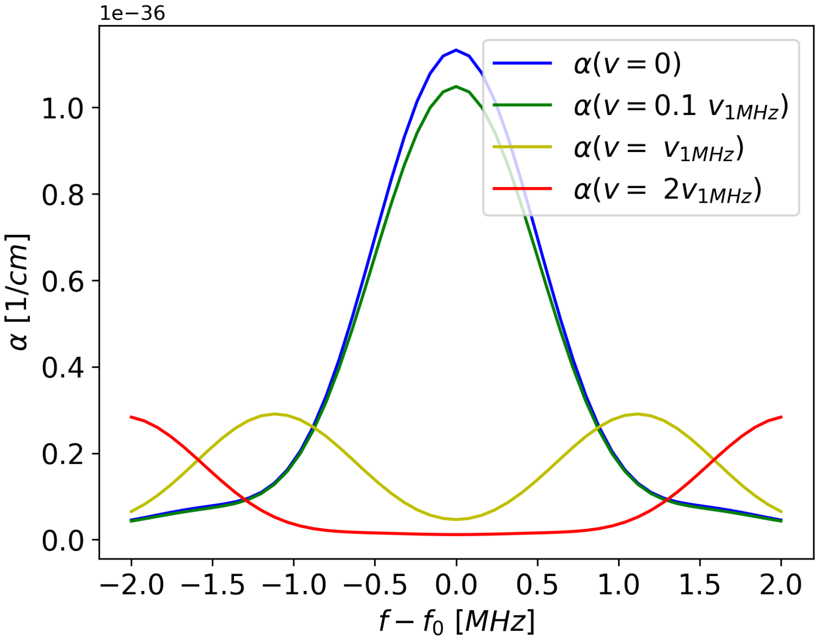

Figure 5.5: Absorption curve of single HD particles (or single velocity classes of HD particles) interacting with an infrared laser beam over an interaction time that corresponds to a HD particle moving along a trajectory at 45° angle at the beam waist for a HD particle travelling at the most probable velocity. The different curves correspond to different velocity along the axis of the cavity. These velocities are multiple of v_{1MHz} which is the velocity that corresponds to a Doppler shift of 1 MHz.

We have seen that the evolution of the population ρ_{22} over the interaction time does not allow to reach a steady state regime. However we saw the amplitude of ρ_{22} for a particle moving with sufficient speed is 1/4 of the one for a particle at rest when both percieve the frequency of the electromagnetic wave as resonant. This is due to the separation of the standing wave into two counterpropagating waves with 1/4 of the intensity carried by each of them as explained before. We can see this effect more clearly with the evolution of the absorption curves of single particles with different velocities like what was done for the toy model. The Lorentzian absorption peak of the rest particle splits into two small peaks with 1/4 of the initial amplitude. One can note that the shift of the absorption peaks does not coincides precisely to the Doppler shift. Indeed the absorption peaks for the particle moving at $v_{1\mathrm{MHz}}$ are not centered on the frequencies $f_0 \pm 1$ MHz. This might be attributed to the oscillations of the population evolution over the interaction time for moving particles. The absorption is computed from the area under the $\rho_{22}(t)$ curve. The oscillations thus impact the area under the curve and with it the absorption coefficient.

5.2.3 Saturated absorption of the HD gas

In order to compute the absorption coefficient as a function of the laser frequency we need to sample properly the two absorption peaks that correspond to each one of the two counter-propagating waves in the cavity (Otherwise the numerical integration performs poorly). This was achieved for the toy model with an adaptative velocity sampling that samples the velocity distribution more densely around the velocities that correspond to the two absorption peaks. The size of the two subsets were determined by the most probable velocity in the absorbing gas v_{mp}. Because we want to sample the velocities that contribute to the Lamb-dip we want to use a velocity with an order of magnitude relevant to the HD gas, i.e. of the same order of magnitude as the width of the Lamb-dip. In the toy model, the Doppler broadening and the width of the Lamb-dip were sufficiently close in term of order of magnitude such that sampling the absorption peaks using v_{mp} was efficient. For the HD gas, the width of the Doppler broadened absorption peak and the Lamb-dip have extremely different orders of magnitude: the first one is $\Delta f \simeq 1.5$ GHz as given by eq. 2.88 and the later is on the order of a few hundred kHz as measured in the experiment of the Amsterdam research group [12]. Thus it is more efficient to replace v_{mp} by another velocity in the sampling algorithm explained for the toy model. We can use a multiple of $v_{1\mathrm{MHz}}$ because the detuning of the laser on the absorption graph presenting the asymmetry 2.17 takes value on the order of 2 MHz. The velocity used eventually in the sampling algorithm is $10 v_{1\mathrm{MHz}}$ after some trials as will be explained in the next paragraph. To conclude on the sampling, the number used for the density of the sampling N_{points} is 100. To give an idea of the density of the sampling, in fig. 5.6 is represented the adaptative sampling of the velocity distribution for a laser frequency with a detuning of 8 MHz and in this figure, $N_{\mathrm{points}} = 30$ for clarity. With $N_{\mathrm{points}} = 100$ the sampling is thus extremely dense. This was necessary because the Lamb-dip amplitude is less than 1% of the absolute value of the absorption coefficient. With a less dense sampling numerical oscillations were present. A possible explanation is that the dense sampling allows to avoid trunctation of the area under the curve in the case of a peak being located between two sampling point for example.

In fig. 5.8 is plotted the saturated absorption coefficient curve of the HD gas. The saturated absorption spectrum shows a symmetric Lamb-dip as expected. The absolute value of the absorption coefficient is not correct. As we have seen before the numerical implementation only reproduces the correct lineshape and a correction factor was needed for the absorption curve of the toy model. For comparison, a simulated Doppler broadened absorption peak (using HITRAN [39]) is shown in fig. 5.9 where the temperature and pressure of the HD gas are the same as in the other simulations of this chapter. The value of the absorption coefficient of HD is on the order of 8 10^{-9} cm^{-1}. The values from the implemented python code in this master thesis are on the order of 5 10^{-40}cm^{-1} and thus differs significantly. This discrepancy is now much bigger than for the toy model where the correction coefficient was 158. Also the relative variation of the absorption at the location of the dip is on the order of 10^{-42} cm^{-1} whereas the relative absorption in the experiment from Amsterdam was on the order of 10^{-12}cm^{-1}. With a

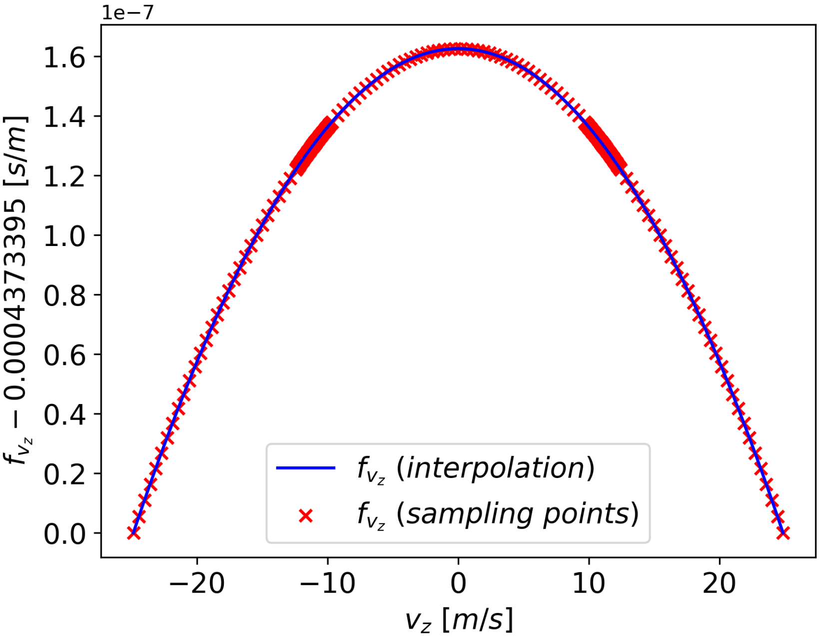

Figure 5.6: Adaptative sampling of the Maxwell-Boltzmann velocity distribution for the HD gas at 0.25 Pa and 300 K. The detuning of the laser is 8 MHz such that the two principal subsets of the velocity are centred on $\pm v_{8\text{MHz}}$, i.e. the velocities that correspond to a Doppler shift of ±8 MHz. These two principal subsets are themselves made of subsets that are denser when closer to the central velocity of the subset which is $\pm v_{8\text{MHz}}$. Each of these subsets is made of 30 points on this figure with 3 subsets on each side of the central velocity. The two principal subsets sample velocity in the range $[-v_{8\text{MHz}} - 10v_{1\text{MHz}}, -v_{8\text{MHz}} + 10v_{1\text{MHz}}]$ and $[v_{8\text{MHz}} - 10v_{1\text{MHz}}, v_{8\text{MHz}} + 10v_{1\text{MHz}}]$ respectively. The value on the vertical axis are offset for clarity.

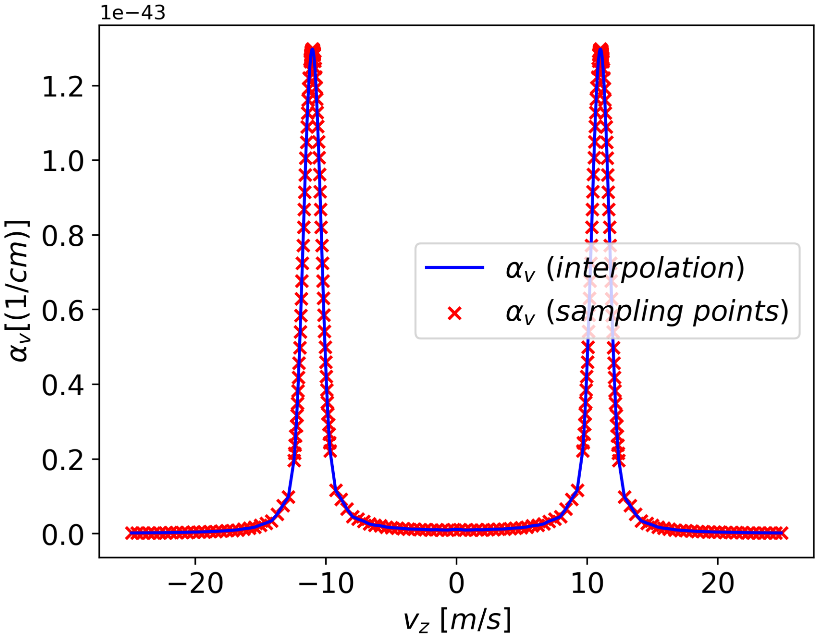

Figure 5.7: Absorption coefficient α_v of a given velocity class as a function of the velocity. The detuning of the laser is 8 MHz and thus the sampling of the velocity distribution is the one shown on fig. 5.6.

correction coefficient on the order of 10^{31} the simulation of the master thesis would match the order of magnitude of the simulation from HITRAN. In addition the relative variation of the absorption coefficient would go from 10^{-42} cm^{-1} to 10^{-11}cm^{-1} and so it would be approximately one order of magnitude greater than what is measured in the experiment.

The Lamb-dip has a FWHM on the order of 2 MHz and the curve becomes flat at approximately ±8 MHz around the resonant frequency. This is the reason why $10v_{1\text{MHz}}$ was used to sample the velocity distribution. This allows to have a continuous sampling of the velocity distribution between the two Doppler shifted peaks. If the velocity range was narrower the two subsets of the velocity sampling would not reach values close to $v = 0$ and the sampling would then not be "continuous " at $v = 0$. The separation bewteen the two subsets would be problematic when integrating over all velocity classes to obtain the absorption coefficient. Indeed, during trial and error to find a good parameter for the sampling range around the Doppler shifted peaks, the separation of the two subsets by a large region with no sampling points appeared to be problematic with sometimes negative absorption coefficient as a result of the integration.

The FWHM of the Lamb-dip is 2.2 MHz. This is one order of magnitude greater than expected from the relaxation rate due to collisions; i.e. $\text{FWHM}_{\text{Collisions}} = 10^5$ Hz. However the FWHM seems consistent with the approximation made about the interaction time. Indeed the interaction time is roughly $\tau_{\text{transit}} \simeq 1$ μs such that the transit time broadening is on the order of $1/\tau_{\text{transit}} \simeq 1$ MHz. The discrepancy with the FWHM due to collisions means that the fixed interaction time chosen for the simulation is not valid as we should have obtain the same FWHM as in the experiment from which the parameters were taken. Instead the FWHM obtain here is larger due to the transit time broadening. Therefore the simulation is limited by transit time broadening whereas the experiment is limited by pressure broadening. Hence it would probably work with a better choice of the fixed interaction time parameter. One that could work would be some kind of average of the interaction time distribution in the gas from all the possible trajectories and their distributions. As mentioned before, the Lamb-dip is related to a small part of the velocity distribution and some arbitrary selection or weighted average of the most relevant trajectories and velocities that contribute to the Lamb-dip would be, a priori, more suited and more efficient. The interaction time would then be more adequate to the physics of the problem. Otherwise a satistical sampling of the different trajectories across the gaussian laser beam would be needed. Either way the choice of the approximation done on the transit time is not accurate and a longer interaction time is needed to reach a resolution on the frequency one order of magnitude better. An increase of the interaction time would at the same time increase the value of the absorption coefficient and it might solve the issue with the depth of the Lamb-dip discussed above. Despite these issues, the agreement between the interaction time and the transit time broadening shows the good behavior of the simulation for a non steady state evolution of the density matrix.

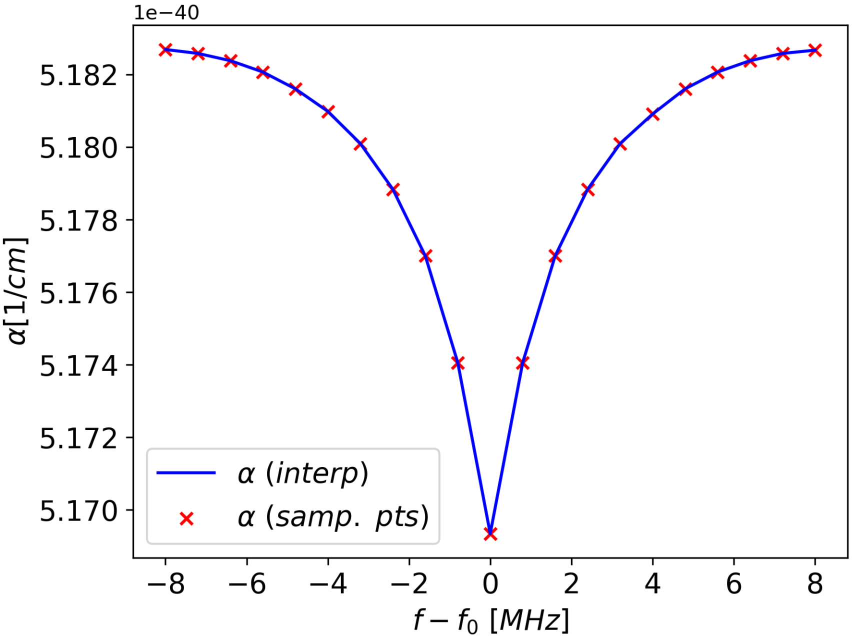

Figure 5.8: Simulation of a Lamb-dip of the absorption coefficient curve of a saturated HD gas at 0.25 Pa and 300 K using the approximation of fixed electric field amplitude perpendicular to the cavity axis and arbitrary fixed interaction time with the laser beam. The interaction time is chosen as the transit time of a HD molecule going through the beam at the waist location with a 45° angle with respect to the cavity axis. (Note: the "pointy" look of the Lamb-dip is due to the few density of sampling points used for the simulation as this simulation takes a lot of time.)

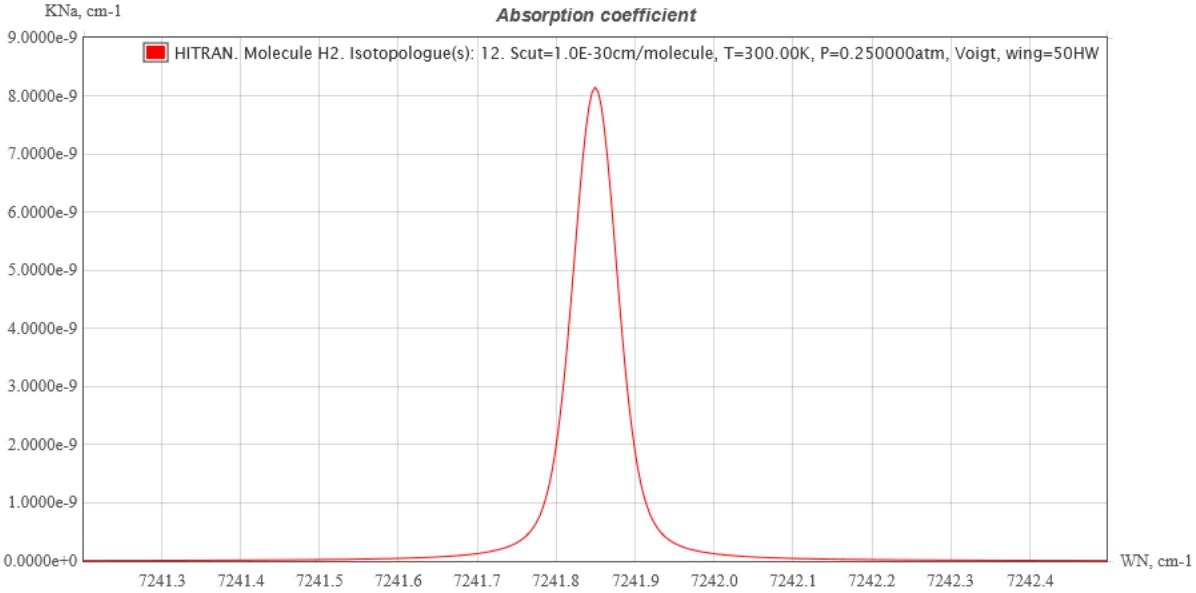

Figure 5.9: Absorption curve of a HD gas obtained with a simulation using HITRAN on the web [39]. The parameters of the HD gas are the same as for the simulations of this chapter, i.e. $N = 0.25$ Pa, $T = 300$K. This simulation on HITRAN was done with no effect of the apparatus. The frequency of the peak is the one of the R(1) (2 − 0) transition expressed in cm^{-1}: $f_{\mathrm{R(1)}\ (2-0)} \simeq 7214.8$ cm^{-1}.

Chapter 6

Conclusions & perspectives

6.1 Conclusions

The recent precision experiments such as the saturation spectroscopy of relatively simple quantum systems like the hydrogen molecule and its isotopologs offers new ways to test fundamental physics. The precision reached on the saturation spectroscopy of HD allows to test extremely small effects of speculative new fundamental physics like extra-dimensions or the existence of a fifth force of nature. From these experiments, new constraints on these theories can be achieved. Although the ability to test these speculative theories is interresting, the ability to confront the current fundamental physics with new experimental results is even more interresting. Indeed, whereas new physics is highly speculative, the validity or not of the current theory is of upmost importance. The theory that describes atoms and molecules the most accurately is quantum field theory. Quantum physics describes three of the four fundamental interactions known. Among these interactions there is the quantum electrodynamics (QED) that is the dominant interaction when one study the spectroscopy of atoms or molecules. The saturated spectroscopy of HD and the recent progress in theoretical QED calculations for the hydrogen isotopologs allow to test directly the validity of QED applied to molecules.

The results of the measurements of rovibrationnal transitions in the HD spectrum seems to be in contradiction with the prediction made from QED. The results of these experiments disagree with theory and the error margin of both do not overlap. This discrepancy is thus very interesting for fundamental physics and thus motivates the research on these transitions. However, one must be careful as both approaches use approximations. This is the case of the experimental measurement of the HD $R(1)$ $(2-0)$ transition.

The measure of the absorption coefficient of the HD molecule as a function of frequency was expected to show a symmetric lineshape but an unexpected asymmetric lineshape was observed. This unexpected profile increases the uncertainty on the measurement of the transition frequency. An explanation of this asymmetry should only reduces the error margins of the experimental measurement of the transition frequency and would in principle not solve the discrepancy between theory and experiment. However this result reminds us that the processes happening in those HD saturated cavity absorption spectroscopy still requires a better understanding.

Hence the goal of this master thesis was to work towards a better understanding of HD cavity saturated absorption spectroscopy experiments. In order to test rapidly processes that could explain the asymmetry of the absorption profile, one can use a numerical simulation of the experiment. For that purpose a numerical simulation of the HD cavity saturated absorption spectroscopy that would predict the expected symmetric absorption lineshape is needed. Only after this first step one can search for the missing physical process that generates the asymmetry. Therefore the implementation of a numerical simulation in this master thesis constitutes a preliminary work for the study of the asymmetry of the HD absorption lineshape.

In this master thesis I have implemented a numerical simulation of saturated cavity absorption spectroscopy. This numercial simulation uses an existing python library for quantum calculations named QuTiP to compute the time evolution of the density matrix of the particles interacting with the laser inside the cavity. The first attempt used the time evolution of the coherences of the density matrix to extract the polarisation of the particle. This method follows directly from the definition of the absorption coefficient and its relation with the dielectric susceptibility of the particle. Unfortunately this method was difficult to apply in the case of cavity spectroscopy due to the presence of a standing wave made of two counterpropagating electromagnetic waves with equal intensity inside the cavity. The standing wave induces spatial variation that are responsible for the difficulty to extract the polarization for moving particles. Moreover, the equal intensity of the two counterpropagating waves prevents the usual approach of a pump laser and a probe laser. An indirect approach was therefore used. This approach is based on the measurement of the total amount of energy lost by the particle through spontaneous emission. In other words, the energy balance of energy coming in and out of the particle gives access to its absorption. Therefore this method uses the time evolution of the populations rather than the time evolution of the coherences. This method proved to be much easier and more computationally efficient. The method was tested on a toy model and assuming a steady state regime of the particle interacting with the laser beam. This gave a lineshape that was in perfect agreement with the analytic formula (2.84). However the absolute value of the absorption coefficient was not correct and a correction factor (= 158) needed to be used.

Eventually the numerical simulation was applied to the HD absorption spectroscopy. The simulation were performed without the steady state assumption this time. This is what actually happens in the experiments. Also the interaction time and the laser beam amplitude were approximated. The result of the simulation are satisfying as it correctly produces a symmetric Lamb-dip even when the steady state is not reached and the full width at half maximum of the Lamb-dip is in agreement with the chosen interaction time. Once again the value of the absorption coefficient is not correct and a correction factor must be used. In addition the FWHM of the Lamb-dip is not yet the one observed in the experiment as well as the depth of the dip. The reason is probably the choice for the approximated interaction time in the simulation that induces a transit time broadening larger than the pressure broadening observed in the experiment. A better choice based on the trajectories and velocity distribution of the HD molecules should give better results.

In conclusion, the present numerical implementation of saturated cavity absorption spectroscopy is able to correctly reproduce expected symmetric lineshape of Lamb-dip even in the case of cavity enhanced spectroscopy. It works both for steady state and transitory regime of the time evolution of the density matrix. However it needs to be improved as the value of the absorption coefficient generated by the simulation must be adjusted with a correction factor. In addition the issue with the approximations used for the HD saturated cavity absorption spectroscopy must be adressed.

6.2 Perspectives

The numerical simulation develloped in this thesis can be used to go further in the analysis of the HD satutared cavity absorption spectroscopy. Here are few perspectives of further devellopment.

- **Calibration of the numerical simulation parameters:** The numerical simulation of the Lamb-dip does not evaluate the correct value of the absorption coefficient, only the lineshape (and its dependance on intensity) is correct. One can search for the solution to obtain directly the exact value of the absorption coefficient and implement it in the code which would be the best option. However, one could also calibrate the absorption curve by a determination of the correction coefficient through comparisons with experimental measurements. In addition, we have seen that the fixed transit time should be better determined. For this purpose one must investigate how to sample the trajectories of the HD molecule in the cavity and average over them to obtain a relevant and valid fixed interaction time parameter in the numerical simulation. As this fixed interaction time is an approximation, some arbitrariness would remain and the method to obtain the fixed interaction time could also be callibrated by a comparison with experimental results to check the validity. If the fixed interaction time hypothesis would proved to be inaccurate, even when it is long enough to properly resolve the absorption frequency below the pressure broadening (such that the simulation is not limited by the transit time), then one should implement a statistical sampling of the trajectories crossing the Gaussian beam.

- **Addition of physical processes:** Obviously at some point an implementation of some mechanism that would account for the asymmetry must be done. As the hyperfine structure has been ruled out the mechanism suggested by the Heifei reasearch group is very promising as it relies on the motion of the particle and not on the internal structure of its energy states. An implementation of the oscillation of the upper energy level to take into account the AC Stark shift should thus be tested.

- **Optimisation of the code:** A slight improvement of the numerical simulation would be to automatize the time sampling for the solver of the QuTiP library. The time sampling implemented has been obtain through trial and errors such that it works for the case under study. In addition, the velocity sampling has been increased until numerical oscillations disappeared. The resulting velocity sampling is very dense and thus very demanding in computation time. It might be worth optimising this sampling to reduce the simulation time of the Lamb-dip.

Bibliography

[1] Jacek Komasa et al. "Rovibrational energy levels of the hydrogen molecule through nonadiabatic perturbation theory". In: *Phys. Rev. A* 100 (2019), p. 032519. DOI: 10.1103/PhysRevA.100.032519. URL: https://link.aps.org/doi/10.1103/PhysRevA.100.032519.

[2] Daniel V. Schroeder Michael E. Peskin. *An Introduction to Quantum Field Theory.* CRC Press, 1995, pp. 196–198. ISBN: 0201503972.

[3] Samir Kassi et al. "The (2–0) R(0) and R(1) transition frequencies of HD determined to a 10-10 relative accuracy by Doppler spectroscopy at 80 K". In: *Phys. Chem. Chem. Phys.* 24 (2022), pp. 23164–23172. DOI: 10.1039/D2CP02151J. URL: http://dx.doi.org/10.1039/D2CP02151J.

[4] M. L. Diouf et al. "Lamb-dips and Lamb-peaks in the saturation spectrum of HD". In: *Opt. Lett.* 44.19 (2019), pp. 4733–4736. DOI: 10.1364/OL.44.004733. URL: https://opg.optica.org/ol/abstract.cfm?URI=ol-44-19-4733.

[5] T.-P. Hua, Y. R. Sun, and S.-M. Hu. "Dispersion-like lineshape observed in cavity-enhanced saturation spectroscopy of HD at 1.4 μm". In: *Opt. Lett.* 45.17 (2020), pp. 4863–4866. DOI: 10.1364/OL.401879. URL: https://opg.optica.org/ol/abstract.cfm?URI=ol-45-17-4863.

[6] Antonio Castrillo, Eugenio Fasci, and Livio Gianfrani. "Doppler-limited precision spectroscopy of HD at 1.4 μm: An improved determination of the $R(1)$ center frequency". In: *Phys. Rev. A* 103 (2021), p. 022828. DOI: 10.1103/PhysRevA.103.022828. URL: https://link.aps.org/doi/10.1103/PhysRevA.103.022828.

[7] C.-F. Cheng et al. "Dissociation Energy of the Hydrogen Molecule at 10^{-9} Accuracy". In: *Phys. Rev. Lett.* 121 (2018), p. 013001. DOI: 10.1103/PhysRevLett.121.013001. URL: https://link.aps.org/doi/10.1103/PhysRevLett.121.013001.

[8] E. J. Salumbides et al. "Bounds on fifth forces from precision measurements on molecules". In: *Phys. Rev. D* 87 (2013), p. 112008. DOI: 10.1103/PhysRevD.87.112008. URL: https://link.aps.org/doi/10.1103/PhysRevD.87.112008.

[9] E J Salumbides et al. "Constraints on extra dimensions from precision molecular spectroscopy". In: *New Journal of Physics* 17 (2015), p. 033015. DOI: 10.1088/1367-2630/17/3/033015. URL: https://dx.doi.org/10.1088/1367-2630/17/3/033015.

[10] Eugenio Fasci et al. "Precision spectroscopy of HD at 1.38 μm". In: *Phys. Rev. A* 98 (2018), p. 022516. DOI: 10.1103/PhysRevA.98.022516. URL: https://link.aps.org/doi/10.1103/PhysRevA.98.022516.

[11] L.-G. Tao et al. "Toward a Determination of the Proton-Electron Mass Ratio from the Lamb-Dip Measurement of HD". In: *Phys. Rev. Lett.* 120 (2018), p. 153001. DOI: 10.1103/PhysRevLett.120.153001. URL: https://link.aps.org/doi/10.1103/PhysRevLett.120.153001.

[12] F. M. J. Cozijn et al. "Sub-Doppler Frequency Metrology in HD for Tests of Fundamental Physics". In: *Phys. Rev. Lett.* 120 (2018), p. 153002. DOI: 10.1103/PhysRevLett.120.153002. URL: https://link.aps.org/doi/10.1103/PhysRevLett.120.153002.

[13] Claude Fabre Gilbert Grynberg Alain Aspect. *Introduction to quantum optics*. Cambridge University Press, 2010, p. 364. ISBN: 9780521551120.

[14] Claude Fabre Gilbert Grynberg Alain Aspect. *Introduction to quantum optics*. Cambridge University Press, 2010, pp. 53–61. ISBN: 9780521551120.

[15] Daniel Manzano. "A short introduction to the Lindblad master equation". In: *AIP Advances* 10 (2020). ISSN: 2158-3226. DOI: 10.1063/1.5115323. URL: http://dx.doi.org/10.1063/1.5115323.

[16] Alan Carrington John M. Brown. *Rotational Spectroscopy of Diatomic Molecules*. Cambridge Molecular Science. Cambridge University Press, 2003, pp. 233–244. ISBN: 9780511814808.

[17] Joya Cooley. *Rovibrational Spectroscopy*. URL: https://chem.libretexts.org/Bookshelves/Physical_and_Theoretical_Chemistry_Textbook_Maps/Supplemental_Modules_(Physical_and_Theoretical_Chemistry)/Spectroscopy/Rotational_Spectroscopy/Rovibrational_Spectroscopy (visited on 10/17/2024).

[18] Christopher J. Foot. *Atomic physics*. Oxford master series in physics. Oxford University Press, 2004, pp. 123–137. ISBN: 9780198506966.

[19] Claude Fabre Gilbert Grynberg Alain Aspect. *Introduction to quantum optics*. Cambridge University Press, 2010, pp. 85–90. ISBN: 9780521551120.

[20] Claude Fabre Gilbert Grynberg Alain Aspect. *Introduction to quantum optics*. Cambridge University Press, 2010, pp. 90–92. ISBN: 9780521551120.

[21] Christopher J. Foot. *Atomic physics*. Oxford master series in physics. Oxford University Press, 2004, pp. 138–147. ISBN: 9780198506966.

[22] Christopher J. Foot. *Atomic physics*. Oxford master series in physics. Oxford University Press, 2004, pp. 151–159. ISBN: 9780198506966.

[23] Daniele Romanini et al. *Cavity-Enhanced Spectroscopy and Sensing*. Ed. by Gianluca Gagliardi and Hans-Peter Loock. Berlin, Heidelberg: Springer Berlin Heidelberg, 2014, p. 3. ISBN: 978-3-642-40003-2. DOI: 10.1007/978-3-642-40003-2_1. URL: https://doi.org/10.1007/978-3-642-40003-2_1.

[24] Jimmy Roussel. *Interférence à N ondes*. URL: https://femto-physique.fr/optique/interference-a-N-ondes.php (visited on 10/29/2024).

[25] Eric Toombs. *Gaussian beam w40mm lambda30mm.png*. URL: https://commons.wikimedia.org/wiki/File:Gaussian_beam_w40mm_lambda30mm.png (visited on 10/29/2024).

[26] Bob Mellish. *GaussianBeamWaist.svg*. URL: https://commons.wikimedia.org/wiki/File:GaussianBeamWaist.svg (visited on 10/29/2024).

[27] Daniele Romanini et al. *Cavity-Enhanced Spectroscopy and Sensing*. Ed. by Gianluca Gagliardi and Hans-Peter Loock. Berlin, Heidelberg: Springer Berlin Heidelberg, 2014, pp. 23–26. ISBN: 978-3-642-40003-2. DOI: 10.1007/978-3-642-40003-2_1. URL: https://doi.org/10.1007/978-3-642-40003-2_1.

[28] Daniele Romanini et al. *Cavity-Enhanced Spectroscopy and Sensing*. Ed. by Gianluca Gagliardi and Hans-Peter Loock. Berlin, Heidelberg: Springer Berlin Heidelberg, 2014, pp. 211–251. ISBN: 978-3-642-40003-2. DOI: 10.1007/978-3-642-40003-2_1. URL: https://doi.org/10.1007/978-3-642-40003-2_1.

[29] Daniele Romanini et al. *Cavity-Enhanced Spectroscopy and Sensing.* Ed. by Gianluca Gagliardi and Hans-Peter Loock. Berlin, Heidelberg: Springer Berlin Heidelberg, 2014, pp. 143–162. ISBN: 978-3-642-40003-2. DOI: 10.1007/978-3-642-40003-2_1. URL: https://doi.org/10.1007/978-3-642-40003-2_1.

[30] G Herzberg. "Rotation-vibration spectrum of the HD molecule". In: *Nature* 166.4222 (1950), pp. 563–563.

[31] FMJ Cozijn, ML Diouf, and W Ubachs. "Saturation spectroscopy of R (0), R (2) and P (2) lines in the (2-0) band of HD". In: *The European Physical Journal D* 76.11 (2022), p. 220.

[32] Y.-N. Lv et al. "Fano-like Resonance due to Interference with Distant Transitions". In: *Physical Review Letters* 129 (2022). DOI: 10.1103/physrevlett.129.163201. URL: https://doi.org/10.1103%2Fphysrevlett.129.163201.

[33] Krzysztof Pachucki and Jacek Komasa. "Electric dipole rovibrational transitions in the HD molecule". In: *Physical Review A—Atomic, Molecular, and Optical Physics* 78.5 (2008), p. 052503.

[34] Paul Nation et al. *QuTiP: Quantum Toolbox in Python (version 5.0.4).* 2024. URL: https://qutip.org/index.html.

[35] Andrew Nelson et al. *SciPy (version 1.14.1).* 2024. URL: https://scipy.org/.

[36] LP Maguire et al. "Theoretical calculation of saturated absorption spectra for multi-level atoms". In: *Journal of Physics B: Atomic, Molecular and Optical Physics* 39.12 (2006), p. 2709.

[37] Peter Joseph Rayer. *Pressure Broadening of Spectral Lines: The Theory of Line Shape in Atmospheric Physics.* Cambridge University Press, 2020, pp. 95–128.

[38] Franciscus Martinus Jacobus Cozijn. "High-Precision Rovibrational Saturation Spectroscopy of H2, HD and HT". English. PhD-Thesis - Research and graduation internal. Vrije Universiteit Amsterdam, Oct. 2024. DOI: 10.5463/thesis.744.

[39] Harvard-Smithsonian Center for Astrophysics (CFA). *HITRAN on the web.* URL: https://hitran.iao.ru/home (visited on 01/01/2025).

UNIVERSITÉ CATHOLIQUE DE LOUVAIN
École polytechnique de Louvain
Rue Archimède, 1 bte L6.11.01, 1348 Louvain-la-Neuve, Belgique | **www.uclouvain.be/epl**